Doctoral Thesis

Two- and Three-Dimensional Network Structures from Design to Application

Sun-Min Jung

Department of Energy Engineering

Graduate School of UNIST

2017

Two- and Three-Dimensional Network Structures from Design to Application

Sun-Min Jung

Department of Energy Engineering

Graduate School of UNIST

Two- and Three-Dimensional Network Structures from Design to Application

A thesis/dissertation
submitted to the Graduate School of UNIST
in partial fulfillment of the
requirements for the degree of
Doctor of Philosophy

Sun-Min Jung

08/18/2017 of submission

Approved by

Advisor
Jong-Beom Baek

Two- and Three-Dimensional Network Structures from Design to Application

Sun-Min Jung

This certifies that the thesis/dissertation of Sun-Min Jung is approved.

08/18/2017 of submission

signature

Advisor: Jong-Beom Baek

signature

Myoung Soo Lah: Thesis Committee Member #1

signature

Noejung Park: Thesis Committee Member #2

signature

Jung-Woo Yoo: Thesis Committee Member #3

signature

Hu Young Jeong: Thesis Committee Member #4;

three signatures total in case of masters

Abstract

From designing a molecular structure to the realization of the structure, the greatest challenge in chemistry is assembling molecules in a specific orientation and with a precise spatial arrangement. Depending on architectures, it is flexible what geometry, size and functional groups of building blocks are composed of and result from controllable chemical/physical properties. For example, the electronic device performance relied on material's properties. Therefore, the material properties are indispensable to maximize status of devices. Graphene has spotlighted since discovery in 2004 due to outstanding physical properties over metal, even though composed of carbon. Inspired by graphene and graphene studies, graphitic 2-dimensional and 3-dimensional materials were prepared. Approached bottom-up process, graphene with heteroatom doping was prepared and succeeded tuning the bandgap and electrocatalytic effect increased. Moreover, graphitic carbon sheets with well-aligned carbon atoms with random-hole showed microporosity with relatively high surface area. The formation of organic-molecule-based superstructures was realized by solid-state conversion of an organic single-crystal. The resultant porous organic framework with 1-dimensional channels showed unusually high thermal stability tolerance to electron-beams. These prepared materials were analyzed the structure thoroughly and applied in energy conversion and storage system, etc.

Key words: graphene, heteroatom-doping, co-doping, band-gap, field effect transistor, dye-sensitive solar cell, graphitic carbon sheet, defect, paramagnetism, microporosity, solid-state reaction, 5,5',5"-(1,3,5-triazine-2,4,6-triyl)triisophthalonitrile, porous crystal, robust crystal, single-crystal-to-single-crystal.

Table of Contents

List of Figures

Figure 2.3. (a) SEM image of C-graphene. Scale bar is 1 μm. TEM images of BC-graphene: (b) bright field (BF) image. Inset is the fast-Fourier transformed (FFT) pattern; (c, d) high-angle annular dark field (HAADF) and bright field (BF) images of scanning TEM (STEM).

Figure 2.4. (a) SEM image of BCN-graphene. Scale bar is 1 μm. TEM images of BCN-graphene: (b) Atomic-resolution TEM image. Scale bar is 2 nm. Inset is the fast-Fourier transformed (FFT) pattern; (c, d) high-angle annular dark field (HAADF) of images of scanning TEM (STEM) and bright field (BF) image. Scale bars are 50 nm.

Figure 2.5. (a) XPS survey spectra of samples. Inset is high-resolution B 1s spectrum of BCN-graphene marked sky blue square in (a). (b) TOF-SIMS spectra. The nitrogen and oxygen peaks were observed in all samples due to chemically/physically attached nitrogen and oxygen. The spectrum from pristine graphite is provided as reference. (c) K-shell excitation of boron, carbon and nitrogen from EELS spectra of samples. The element mappings of BCN-graphene: (d) dark field TEM image and dotted region is mapping area with 20 nm of scale bars; (e) carbon; (f) boron; (g) nitrogen.

Figure 2.6. Schematic representations of energy gains (formation energy plus lattice energy) of chemical reactions: (a) the formation of B-B bond; (b) the formation of C-C bond; (c) the formation of B-C bond; (d) the formation of B-C *via* Br_3B-N=N-BBr_3 complex. The formation of Br_3B-N=N-BBr_3 complex *via* Lewis acid-base interaction between Lewis acid BBr_3 and Lewis base nitrogen.

Figure 2.7. Summary of DFT calculations for formation energies of various chemical reactions: (a) the formation of B-B bond; (b) the formation of C-C bond; (c) the formation of B-C bond; (d) the formation of B-C *via* Br_3B-N=N-BBr_3 complex. The formation of Br_3B-N=N-BBr_3 complex *via* Lewis acid-base interaction between Lewis acid BBr_3 and Lewis base nitrogen. The number in parenthesis is the formation energy per unit chemical reaction.

Figure 2.8. (a) Raman spectra of samples taken with a He-Ne laser (532 nm) as the excitation source; (b) TGA thermograms obtained with ramping rate of 10 °C min^{-1} in air; (c) XRD powder patterns of samples; (d) XRD patterns marked pink rectangle in (c). The asterisks indicate the trapped residue of KCl crystal.

Figure 2.9. Nitrogen adsorption/desorption isotherms obtained and the calculation of pore size: (a) C-graphene; (b) BC-graphene; (c) BCN-graphene.

Figure 2.10. Dispersion stability of sample solutions in NMP standing at normal laboratory condition for two months. (concentration: 5 mg mL^{-1})

Figure 2.11. (a) The transfer curve of BCN-graphene FET at a drain voltage of 0.1 V. Inset image is schematic illustration of BCN-graphene FET; (b) a tapping-mode AFM image of BCN-graphene film on a SiO_2/Si wafer. The embedded graph is the thickness profile. The scale bar is 200 nm. Output curves of BCN-graphene FET at different gate voltages: (c) p-type output curves; (d) n-type output curves.

Figure 2.12. (a) UV-vis absorption spectrum of BCN-graphene (NMP used as the solvent), (b) Absorbance squared vs. the photon energy ($h\upsilon$) plotted as a function of energy of BCN-graphene shows a linear tendency for an indirect transition.

Figure 3.1. (a) TOF-SIMS spectra of PG, BG, and graphite. Graphite is a reference for comparison. (b) EELS spectra of boron and carbon K edge collected at PG and BG. (c) Raman spectra of PG and BG. (d and e) Nitrogen adsorption/desorption isotherms: (d) PG and (e) BG.

Figure 3.2. SEM images: (a) PG and (b) BG. Scale bars are 1 μm. TEM bright field (BF) images: (c) PG; (d) BG. Insets are fast-Fourier transformed (FFT) patterns.

Figure 3.3. (a, b) TEM bright field (BF) images of PG. (c, d) High-angle annular dark field (HAADF) of images of scanning TEM (STEM) and BF image.

Figure 3.4. (a, b) TEM bright field (BF) images of BG. (c, d) High-angle annular dark field (HAADF) of images of scanning TEM (STEM) and BF image.

Figure 3.5. SEM images of PG and BG coated on FTO/glass substrates by e-spray: (a-c) PG with at different magnifications: (a) scale bar is 100 μm; (b) scale bar is 20 μm; and (c) scale bar is 4 μm. (d-f) BG with at different magnifications: (d) scale bar is 100 μm; (e) scale bar is 20 μm and (f) scale bar is 4 μm. Both samples are well covered on FTO surface with some aggregates (white ovals in (b) and (e)).

Figure 3.6. (a) Current-voltage characteristics of the DSSCs with Pt, PG, and BG CEs under one sun illumination (AM 1.5 G). The TiO_2 film thickness and active area are 9 (6 + 3) μm and 0.16 cm^2 with a black metal mask, respectively. (b) Cyclic voltammograms obtained at a scan rate of 10 mV s^{-1} for oxidation and reduction of the $Co(bpy)_3^{2+/3+}$ redox couple using Pt, PG, and BG electrodes as the working electrodes, a Pt wire as the CE, Ag/Ag^+ as the reference electrode, and 0.1 M $LiClO_4$ as the supporting electrolyte. (c) Nyquist plots measured at 0 V from 10^6 Hz to 0.1 Hz on symmetrical dummy

cells with Pt, PG and BG electrodes. (d) Electrochemical stability of identical dummy cells after 100 cycling potentials (e.g. 100 × CV scans (from 0 V → 1 V → −1 V → 0 V at a scan rate of 50 mV s^{-1})).

Figure 3.7. Chemical formulas: (a) JK-303 dye; (b) HC-A (SGT-301); (c) $Co(bpy)_3^{2+/3+}$ redox couple.

Figure 3.8. Potential-step chronoamperometry curves on symmetrical dummy cells with the Pt and BG electrodes. Potential was from 0 to 0.8 V for 10 s.

Figure 3.9. Tafel-polarization curves of the symmetrical cells fabricated with two identical BG and Pt electrodes at room temperature.

Figure 3.10. Nyquist plots in the full-frequency range (a) and high-frequency region (b) of DSSCs with different CEs at a forward bias of −0.85 V under dark conditions. The inset shows the equivalent circuit for fitting at the high-frequency region.

Figure 4.1. (a) Digital photographs of reaction process. Mixed monomer **1**, **2** or **3** with P_2O_5, respectively. The final product was black powder of GCSs. (b) The brief reaction scheme of GCS-1.

Figure 4.2. DSC thermograms from the first heating scans with ramping rate of 10 °C min^{-1} using high-pressure pan. (a) Mixed powder of acetyl monomers (**1**-**3**) with P_2O_5 with same ratio of GCSs and (b) monomers (**1**-**3**) without P_2O_5. The exothermal peaks of the existence of P_2O_5 are much lower than only monomer state. Monomers are decomposed and carbonized after phase transition to gas-state.

Figure 4.3. (a) Solid-state ^{13}C NMR of GCSs. (b) Fourier transform infrared (FT-IR) spectra of GCSs.

Figure 4.4. (a) SEM images of GCS-1. Inset is SEM image at low magnification and the scale bar is 10 μm. (b) TEM image of exfoliated GCS-1 at low magnification. (c and e) AR-TEM image of GCS-1; (d and f) schematic diagrams of different hole-defects in a graphitic carbon sheet. (c) monolayer of GCS and graphitic carbon aligned like graphene (white dotted line) and hole-defects marked by yellow dotted line and (d) brief structure scheme of (c) described intact hole-defect; (e) Hole-defect blocked by stacked another layer marked by yellow dotted line, and (f) brief structure of scheme of (e) described hole-defect blocked by another graphitic carbon sheet.

Figure 4.5. SEM images of (a) GCS-2 and (c) GCS-3. Each inset is SEM image at low magnification with 10 μm of scale bar. TEM image of exfoliated (b) GCS-2 and (d) GCS-3 at low magnification.

Figure 5.6. Brief mechanism of the formation of *s*-triazine of three benzoniriles under the acid catalyst.

Figure 5.7. Fourier transform infrared spectroscopy (FT-IR) spectra of TCB, TCB-250 and TCB-250HCl. The *s*-triazine of TCB-250HCl vibrated at both 1531 and 1360 cm^{-1}. The sp^2 C-H stretching peak from TIPN was shifted at 3074 cm^{-1} compared with that of TCB at 3084 cm^{-1} due to resonance effects between benzene and the *s*-triazine ring.

Figure 5.8. The solubility of TCB, TCB-250 and TCB-250HCl in NMP (concentration: 2 mg mL^{-1}): (a) under the light, (b) in the dark inside with a laser penetration for Brownian motion. Dispersed particles indicated TIPN in each solution.

Figure 5.9. (a) CPK diagram of TIPN viewed along the crystallographic b-axis. The yellow ball and stick represent traces of water at partial occupancy sites in the solvent channels (color codes: grey = carbon; blue = nitrogen; white = hydrogen). (b) Ball-and-stick packing diagram of TIPN crystal and red lines indicate interdigitation between two TIPNs by dipole-dipole interactions with each distance; a: 2.75 Å; b: 2.76 Å and c: 2.71 Å.

Figure 5.10. (a) ORTEP drawing of TIPN. (b) Ball-and-stick packing diagram of TIPN viewed along the crystallographic *b*-axis. The red balls represent traces of water at partial occupancy sites in the solvent channels. (c) CPK diagram of the interdigitated 1D zig-zag ribbon structure viewed from *b*-axis perpendicular to *ac*-plane, and (d) along the *ac*-plane of the molecules. (e) CPK diagram of the π-π stacked 1D column viewed (a) in parallel.

Figure 5.11. PXRD and single crystal XRD patterns of TIPN.

Figure 5.12. The formation energy diagram for formation of single *s*-triazine compared with TIPN and CTF-0 as the 2-dimensional polymeric crystal (color code: grey = carbon; blue = nitrogen; white = hydrogen).

Figure 5.13. (a) The formation energy difference between TIPN and TIPN crystal composed of 8 units ($C_{216}N_{72}H_{72}$). The formation energy is computed to be −3.6322 eV per unit ($C_{27}N_9H_9$). The interaction energy of two TIPNs; van der Waals interaction (π-π) and dipole-dipole interaction (D-D) of a side of unit $C_{27}N_9H_9$ described molecules into figures. (b) The interaction energy between two TCBs in the crystal lattice, which composed of van der Waals interaction (π-π) and dipole-dipole interaction (D-D) of a side unit $C_9N_3H_3$ (color code: grey = carbon; blue = nitrogen; white = hydrogen).

Figure 5.14. (a) Schematic diagram of TIPN crystal facets revealed by TEM; (b) SEM images of TIPN crystal: Inset is the magnified image from red square. (c) TEM images of TIPN. (d) SAED pattern from (c) region. The crystal (001) facet is parallel to the grid. (e) Cross-sectional TEM image of TIPN crystal prepared by FIB; (f) Selected area electron diffraction (SAED) pattern from (e) region depicting zone axis of [010]. The main crystal growth direction is perpendicular to the image plane, the crystallographic *b*-axis. (g) Atomic-resolution TEM image of the magnified region in (e) which shows a well-ordered crystal lattice; (h) Inverse fast-Fourier transform (IFFT) image. The image is matched with a TIPN crystallographic model determined by XRD (color codes: grey = carbon; blue = nitrogen). The scale bars indicate: (b) 5 μm; (c) 500 nm; (e) 200 nm; (g) 5 nm; (h) 2 nm.

Figure 5.15. (a) Optical microscopy images of TIPN crystalline. The scale bars indicate 20 μm. (b) SEM images of TIPN with scale bar is 50 μm and the inset is a magnified image of the region marked with a red box with the scale bar of 1 μm. (c) SEM image shows TIPN powder (scale bar: 50 μm).

Figure 5.16. (a) EDX spectrum of TIPN. EDX spectrum was collected in marked region. Inset table recorded the EDX quantitate analysis and EDX mapping of TIPN: (b) SEM image, (c) carbon, (d) nitrogen and (e) oxygen.

Figure 5.17. FIB milling process of TIPN. (a) Deposited carbon layers onto TIPN crystal rod for FIB milling. (b) Cross section of TIPN crystal, showing the hexagon shape. Scale bars: (a) 2 μm and (b) 1 μm.

Figure 5.18. (a) The image of hexagonal cross-section of TIPN crystalline rod prepared by FIB. The main axes are indicated single crystal axis. The scale bar indicates 200 nm. (b) The selected area electron diffraction (SAED) pattern from (a) region depicting zone axis of [010]. (c) the octagonal cross-section of TIPN crystalline fabricated by FIB milling process of TIPN. The scale bar indicates 300 nm. (d) SAED pattern from (c) region having zone axis of [010]. SAED patterns ((b) and (d)) follow same trends having hexagonal spots.

Figure 5.19. (a) The polygons of TIPN crystal distribution. The ratio of 87.5% occupied hexagonal shape and 12.5% took octagonal shape in cross-section. (b) The hexagonal cross-section has three faces and (c) the octagonal cross-section has the four faces. The scale bars indicate 1 μm.

Figure 5.20. (a) The simulated SAED pattern of TIPN having zone axis of [001]. (b) Simulated SAED pattern having zone axis [010] and (c) simulated TEM image of cross-section of TIPN crystal image

having zone axis [010]. The scale bar indicates 2 nm. The inset is a magnified image of the region marked with a white box, which is decorated by TIPN molecules and scale bar indicates 1 nm.

Figure 5.21. (a) The high-resolution TEM image and corresponding a fast-Fourier transform (FFT) pattern. (b) The inverse fast-Fourier transform (IFFT) image from (a). The lattice image indicates a regularly ordered crystalline. (c) The simulated IFFT images the calculated TIPN molecular model. The white contrast indicates a vacant pore (color codes: grey = carbon; blue = nitrogen). The scale bars: (a) 5 nm, (b) 1 nm and (c) 1 nm.

Figure 5.22. The K-shell excitation of carbon and nitrogen from electron energy loss spectroscopy (EELS) spectrum of TIPN.

Figure 5.23. Electron ionized mass spectroscopy of TIPN, which is 459.0 *m/z* (M^+, calcd. 459.10). TIPN defragmented into an initial starting reactant TCB, originated in *s*-triazine, which was destroyed by strong electron source at *m/z* 153.0 (M^+, calcd. 153.03).

Figure 5.24. FT-IR spectra of TIPN and TCB.

Figure 5.25. TGA thermograms of TCB and TIPN obtained with ramping rate of 10 °C min^{-1}. TIPN shows unusually high thermal stability under nitrogen gas. Inset is a photograph of residue at 1000 °C.

Figure 5.26. Gas adsorption/desorption isotherms of TIPN with N_2 at 77 K and CO_2 at 196 K (filled circle for absorption and open circle for desorption).

List of Tables

Nomenclature

0D	Zero-dimensional
1D	One-dimensional
2D	Two-dimensional
3D	Three-dimensional
COF	Covalent organic framework
CNT	Carbon nanotube
TMD	Transition metal dichalcogenide
MOF	Metal-organic framework
BCN-graphene	Boron and nitrogen co-doped graphene
FET	Field effect transistor
CVD	Chemical vapor deposition
TGA	Thermogravimetric analysis
BET	Brunauer-Emmett-Teller
FE-SEM	Field emission scanning electron microscopy
HR-TEM	High-resolution transmission electron microscopy
SAED	Selected area electron diffraction
FFT	Fast-Fourier transformed
EELS	Electron energy loss spectroscopy
BF	Bright field
HAADF	High-angle annular dark field
XPS	X-ray photoelectron spectroscopy
XRD	X-ray diffraction
TOF-SIMS	Time-flight secondary ion mass spectrometry
AFM	Atomic force microscopy
PMMA	Poly(methyl methacrylate)
DFT	Density functional theory
PG	Pristine graphene
BG	Boron-doped graphene
DSSC	Dye-sensitized solar cell
CE	Counter electrode
FTO	Fluorine-doped SnO_2
PCE	Power conversion efficiency
FF	Fill factor
CV	Cyclic voltammetry
EIS	Electrochemical impedance spectroscopy
EC	Equivalent circuit
CPE	Constant phase element
GCS	Graphitic carbon sheet
DSC	Differential scanning calorimetry
TCB	1,3,5-tricyanobenzene
TIPN	5,5',5"-(1,3,5-triazine-2,4,6-triyl)triisophthalonitrile
FIB	Focused ion beam
EDX	Electron-dispersive X-ray

I. Introduction

1.1 Molecular Assembly

The chemistry challenge is to achieve assembling molecules in a specific orientation and with a precise spatial arrangement. For chemistry challenge, it was motivated by nature to synthesize complex systems from the atomic-level assembly with modification. Chemical architectures have great progress in constructing numerous with discrete (zero-dimensional, 0D) to extended structures (one-dimensional (1D), two-dimensional (2D), and three-dimensional (3D)) by assembling the diverse building units in different methods. The molecular architectures built from molecular fragment has been realized as shown in Figure 1.1. The driving force to assemble the molecules is based on the energy gain in thermodynamics. The molecular assembly has been carried out through different strategies such as non-covalent bond (intermolecular/intramolecular interactions) and covalent bond formation. Non-covalent bond has somewhat weak interactions from electromagnetic interactions between molecules or within molecules, for examples, electrostatic, π-π effects, van der Waals forces, hydrophobic effect etc.[1] The broad examples representative non-covalent bond including proteins, organic crystals, organic compounds, drugs, etc.

Covalent bond defines that a region of relatively high electron density between nuclei which arises at least partly from sharing of electrons and give rise to an attractive force and characteristic internuclear distance.[2] It is a chemical bond, showing strong interaction by sharing electron pairs between atoms, which to attain the equivalent of a full outer shell, corresponding to a stable electronic configuration.[3] It contains σ-bonding, π-bonding, metal-to-metal bonding, three-center two-electron bond, bent bond, agnostic interaction, etc. The individual molecules, macromolecular compounds, and polymeric compounds are linked by the covalent bond as a unimolecular structure.

1.2 Polymer Considered as a Macromolecule

Hermann Staudinger first proposed the high molecular concept indicating long chains of lots of small monomers held by covalent bond formation to synthesize macromolecules in 1920s, which termed polymers, introduced in the literature in 1833.[4] In other words, polymer structure is consisted of repeated the monomer linkage in a single chain, and high molecular weight results from the entanglement. His work expanded to the chemical understanding of polymers and the field of polymer chemistry.

Polymers are also classified by dimensional state such as 1D, 2D and 3D polymers relying on the building block topologies. The architecture is important to affect polymer's physical properties: viscosity, solubility, glass transition temperature and size of individual polymer coils in the solution.[5] The simple 1D polymer so called linear polymer in solution behaves as the random-walk model, which are sequence of random steps on a lattice.[6] The topology of linear polymer developed chain shape from bifunctional monomers between functional groups located at the 180° orientation (Figure 1.2a).

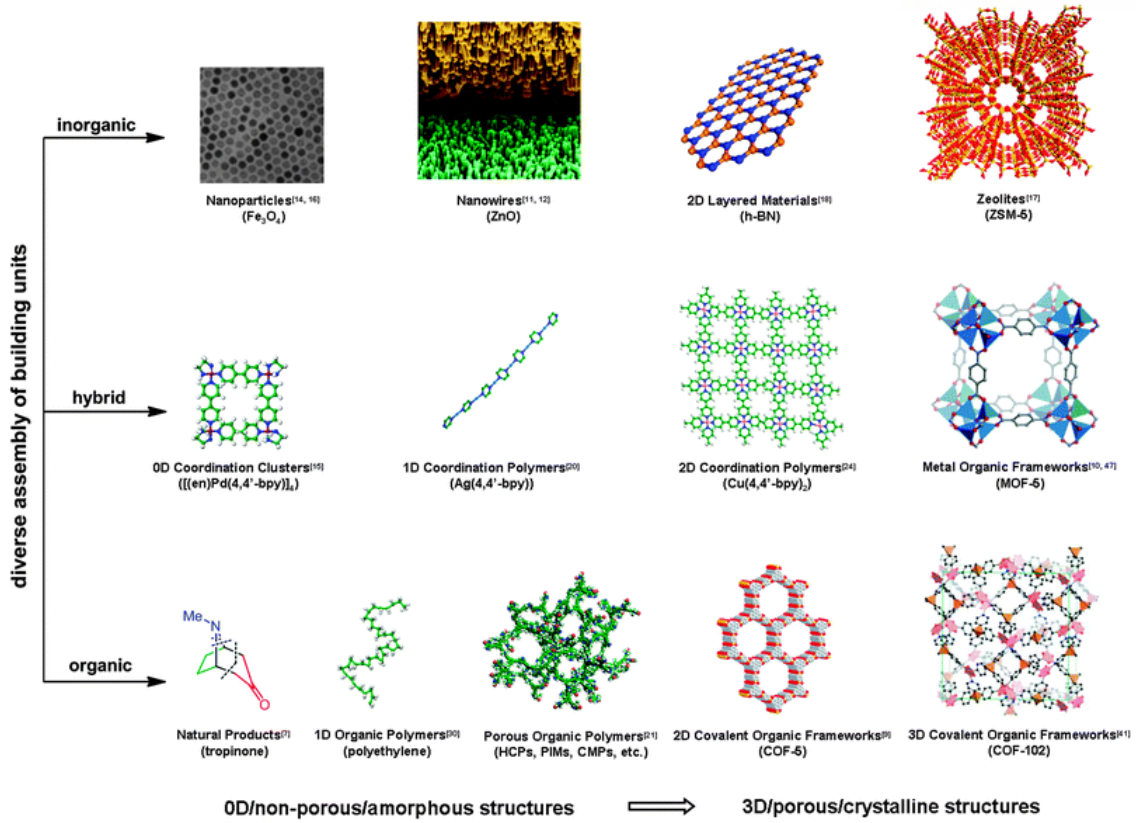

Figure 1.1. Selected examples for diverse assembly of building units to construct inorganic/hybrid/organic chemical architectures, ranging from the discrete 0D/non-porous/amorphous structures to the extended 3D/porous/crystalline structures. For clarity, many related systems, such as active carbons, mesoporous silicas, periodic mesoporous organosilicas, mesoporous carbons, and supermolecules are not included herein.[7]

Two-dimensional polymer has been spotlighted having sheet-like morphology, as defining that a covalently linked network of monomers with periodic bonding in two orthogonal directions (Figure 1.2b).[8] Strictly speaking, 2D polymer should be isolated as a single layer. Dissimilarities between linear polymer (1D polymer) and 2D polymer has a different topology, robustness, assembling chemical functionality with atomic-level precision and what subtle changes make 2D polymer dramatically and unpredictably affect the solid-state structure of molecular compounds.[8] To interpret the 2D polymer structure, the XRD analysis is the best option. However, the amorphous polymer has randomly arranged in solid-state, preparation of crystalline 2D polymer is the big challenge. In 2014, Kissel *et al.*, successfully synthesized single-crystal 2D polymer by photopolymerization and well-organized polymer structure was observed.[9] Similarly, covalent organic frameworks (COFs) epitomize reticular chemistry, which has high crystallinity and open organic framework.[10] For forming crystallinity, the reversible reaction has been introduced in 2005, which provides for error-correction, was used to reticulate molecular building blocks into extend, crystalline COF.[11] However, COF is classified into framework as a kind of macromolecule, not a polymer, because the molecular weight didn't satisfy

commercial polymer's molecular weight.

Three-dimensional polymer has studied for high surface area porous polymers built from 3D rigid monomer.[12] Moreover, hyperbranched polymer and dendrimer are 3-dimensional globular structures. (Figure 1.3).[13]

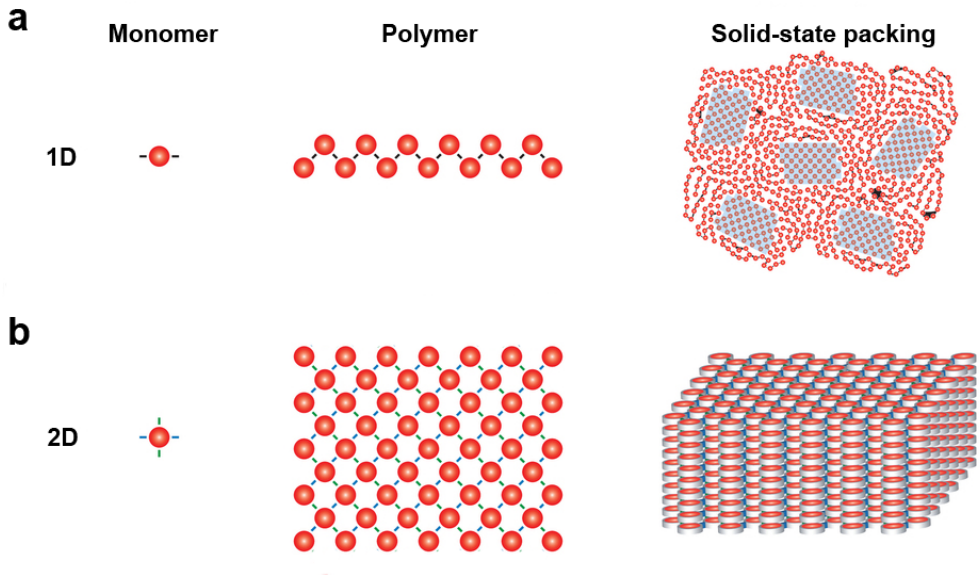

Figure 1.2. Schematic illustration of the structures of one- and two-dimensional polymers. (a) Some 1D polymers pack into crystalline domains (shown as blue-shaded regions) within a disordered matrix, whereas others are amorphous in the solid state. (b) 2D polymers can be isolated as multilayer crystals or as individual sheets.[8]

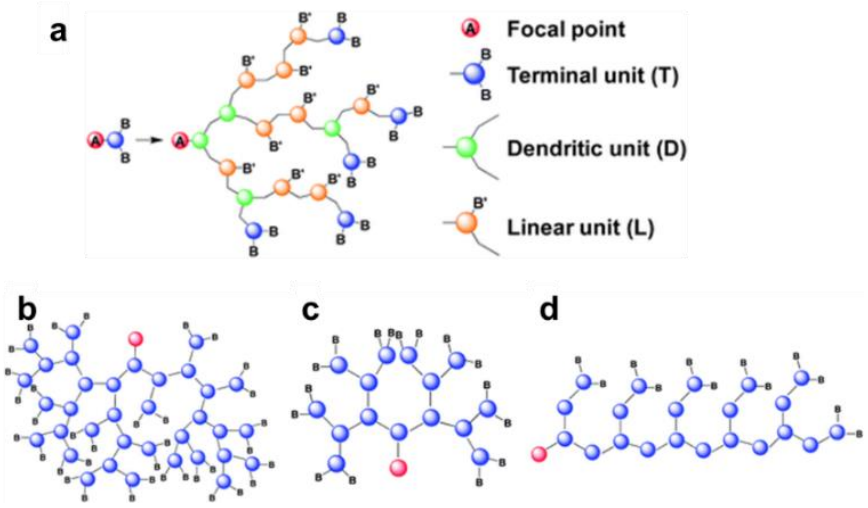

Figure 1.3. (a) Different segment types present in hyperbranched polymer. (b-d) Possible structures of hyperbranched polymers with 100% degree of branching delivered from an AB_2 monomer. (b) Dendrimers wedge, (c) perfect hyperbranched polymer, and (d) quasi-linear polymer.[13]

1.3 Carbon Materials

Note: This chapter is partially adapted with permission from "Carbon Materials and Nanotechnology" Copyright © 2010, WILEY-VCH Verlag.

Carbon is the 15th most abundant terrestrial elements' frequency and the 4th most abundant universe element by the mass.[14] Carbon materials are familiar with our life, termed carbon allotropes from graphite to diamond with the different covalent bond and it shows different topologies and physical/chemical properties even composed of primary carbon atoms (Table 1.1 and Figure 1.4).

Carbon atom bears six electrons: two electrons tightly bound, which close to the nucleus, and the remaining four regarded valence electrons. The electronic configuration is 1 s^2, 2 s^2, 2 p^2, accordingly. This implies a bivalence, which in fact does only exist in a few structures, though. In the most majority of its compounds, carbon is tetravalent. The preferred tetravalence maybe explained with the hybridization model: the energetic difference between 2 *s*- and 2 *p*-orbital is rather low compared to the energy released in chemical binding. Therefore, it is possible for the wavefunctions of these orbitals to mix and form four equivalent hybridized orbitals. These sp^3-hybrid orbitals are directed toward the four corners of a tetrahedron circumscribed to the carbon atom. Likewise, the 2 *s*-orbital may mix with a lower number of 2 *p*-orbitals to form sp^2- or *sp*-hybrid orbitals, respectively. As depending on the degree of hybridization, the resulting compounds show different structural feature: *sp*-hybridized carbon atoms form linear chain, whereas sp^2- and sp^3-hybridization bring about planar structures and 3D tetrahedral networks, respectively. In *sp*- or sp^2- hybridized C-atoms there are two or one *p*-orbitals not taking part in hybridization. These can form π-bonds that, in contrast to σ-bonds, do not exhibit rational symmetry. Their existence shows in bond length and enthalpies.[15]

Table 1.1. Properties of carbon materials[16]

Properties	Fullerene	Carbon nanotubes	Activated carbon	Graphite	Graphene
Specific surface area ($m^2\ g^{-1}$)	5	1,315	1,200	~10	2,630
Thermal conductivity ($Wm^{-1}K^{-1}$)	0.4	>3,000 (multi-walled CNT)	0.15-0.5	~3,000 (in-plane values)	~5,000
Intrinsic mobility ($cm^2V^{-1}s^{-1}$)	0.56	~100,000	-	13,000 (in plane values)	~200,000 (free-standing)
Young's modulus (TPa)	0.01	0.64	0.138	1.06	~1.0
Optical transparency (%)	-	-	-	-	~97.7

Carbon allotropes structures give rise to degree of hybridized carbon atoms and their topologies totally are different from fullerene (0D), carbon nanotube (1D), graphene (2D), diamond (3D) and graphite (3D) with diverse dimension. (Figure 1.4) Among various carbon materials, one of the fastest growing material is graphene since experimentally discovered in 2004. Graphene defines a single layer of graphite, composed of sp^2-hybridized carbon atoms over *xy*-plane, whose π-electron is delocalized over the graphene layer.

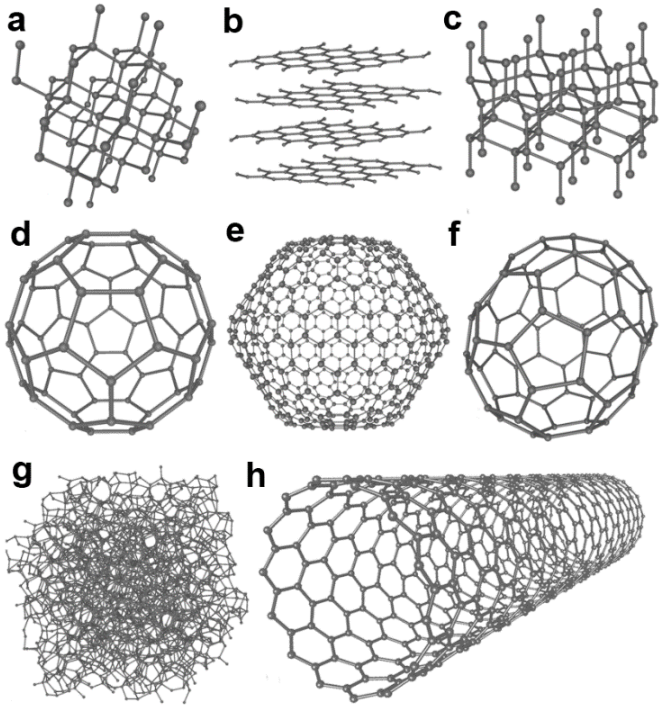

Figure 1.4. The structures of eight allotropes of carbon: (a) Diamond (3D, network covalent structure), (b) Graphite (2D, covalent plates) (graphene is a single of graphite), (c) Lonsdaleite, (d) C_{60} (0D, molecules) (Buckminsterfullerene or buckyball), (e) C_{540} Fullerene, (f) C_{70} Fullerene, (g) Amorphous carbon, (h) Single-walled carbon nanotube. (1D, tubes) by Michael Ströck, February 7, 2006.

1.4 Two-dimensional Materials

Landau and Peierls concluded that 2D crystals were theoretically unstable and couldn't exist because thermal fluctuation could be destroyed 2D crystals.[17] Furthermore, some experiments proved this theory and explained 2D crystals melt when the thermal vibration of atoms in solid become unstable film,[17] and monolayer is regarded a part of larger 3D structures grown by epitaxial onto crystal substrate. This theory has been considered as widely-accepted theory until discovery of graphene.

Graphene was discovered in 2004, the outstanding properties based on high crystallinity and the most of graphene charge carriers can wander thousands of interatomic distances without scattering.[18] Indeed, it can be argued that the obtained 2D crystallites are quenched in a metastable state because they are isolated from 3D materials, whereas their small size less than 1 mm and strong interatomic bonds ensure

that thermal fluctuations cannot lead to the generation of dislocations or other crystal defects even at elevated temperature.[17] Crumpled 2D crystals in 3D warping are stable by minimizing the total free energy above certain temperature.

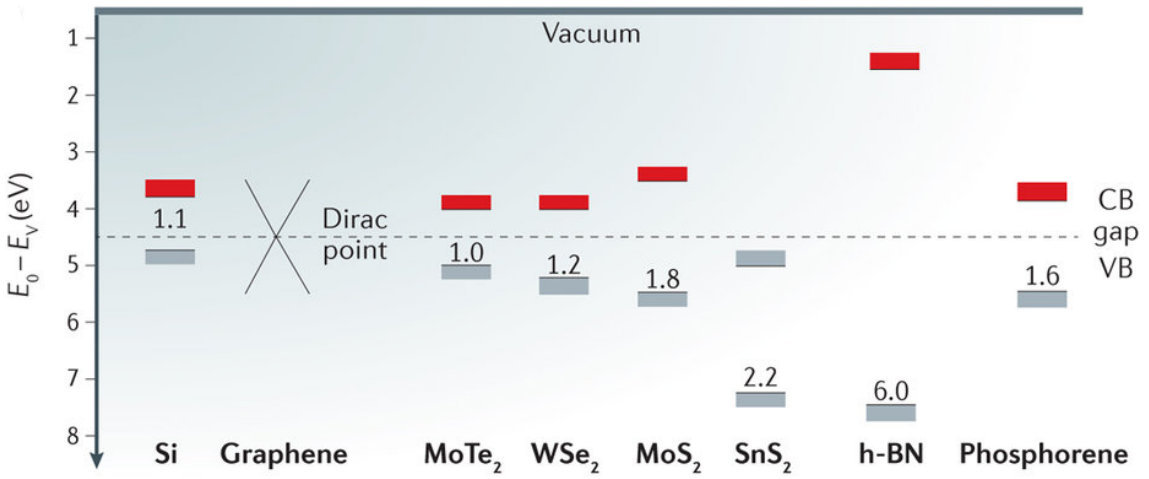

Figure 1.5. Energy levels of various 2D materials compared with that of silicon. The numbers between the valence band (VB) and conduction band (CB) energies indicate the bandgaps of the materials. The energies with respect to the vacuum level (the work function or the electron affinity) are approximate and subject to experimental refinement.[19]

Inspired by graphene, scientists have gotten tremendous attention and synthesized 2D crystals or 2D materials, due to their unique physical/chemical properties from the structure. Besides, newly discovered and synthesized 2D materials have expanded their field to apply electronic devices to have a chance to replaced silicon transistor (Figure 1.5). To overcome graphene's zero-bandgap, there are salient strategies; physically/chemically doped graphene, sandwiched 2D materials, and exploring new 2D materials,[20] for example, as an insulator; boron nitride (*h*-BN),[21] as semiconductors; transition metal dichalcogenides (TMDs), which composed of MX_2 having bandgap range of 1-2 eV, transition metal atom (M = Mo, W, We and so on) being in two chalcogen atoms (X = S, Se, Te and so on),[22] germanene,[23] silicene[24] and exfoliated single-layer from metal-organic frameworks (MOFs),[25] COFs,[26] and 3D layered materials, etc. Applications are infinite about electronic devices as well as electrochemical electrodes, energy generation and storage systems, catalysts, and so on.[27]

1.5 References

1. Anslyn, E. V.; Dougherty, D. A. *Modern Physical Organic Chemistry*; University Science Books, 2006.
2. McNaught, A. D.; Wilkinson, A. *IUPAC. Compendium of Chemical Terminology*; Blackwell Scientific Publications: Oxfor, 1997.

3. Brown, W. H. *Introduction to organic chemistry*; Saunders College Pub., 2000.
4. Mülhaupt, R. *Angew. Chem. Int. Ed.* **2004**, *43*, 1054.
5. Fried, J. R. *Polymer Science and Technology*; Prentice Hall PTR, 1995.
6. Schlüter, A. D.; Payamyar, P.; Öttinger, H. C. *Macromol. Rapid Commun.* **2016**, *37*, 1638.
7. Ding, S. Y.; Wang, W. *Chem. Soc. Rev.* **2013**, *42*, 548.
8. Colson, J. W.; Dichtel, W. R. *Nat. Chem.* **2013**, *5*, 453.
9. Kissel, P.; Murray, D. J.; Wulftange, W. J.; Catalano, V. J.; King, B. T. *Nat. Chem.* **2014**, *6*, 774.
10. Yaghi, O. M. *J. Am. Chem. Soc.* **2016**, *138*, 15507.
11. Côte, A. P.; Benin, A. I.; Ockwig, N. W.; O'Keeffe, M.; Matzger, A. J.; Yaghi, O. M. *Science* **2005**, *310*, 1166.
12. Zhang, C.; Zhu, P. C.; Tan, L.; Liu, J. M.; Tan, B.; Yang, X. L.; Xu, H. B. *Macromolecules* **2015**, *48*, 8509.
13. Segawa, Y.; Higashihara, T.; Ueda, M. *Polym. Chem.* **2013**, *4*, 1746.
14. Jorgensen, S. E.; Fath, B. *Encyclopedia of Ecology*; Elsevier Science, 2014.
15. Krüger, A. *Carbon Materials and Nanotechnology*; Wiley, 2010.
16. Choi, H. J.; Jung, S. M.; Seo, J. M.; Chang, D. W.; Dai, L. M.; Baek, J. B. *Nano Energy* **2012**, *1*, 534.
17. Geim, A. K.; Novoselov, K. S. *Nat. Mater.* **2007**, *6*, 183.
18. Novoselov, K. S.; Geim, A. K.; Morozov, S. V.; Jiang, D.; Zhang, Y.; Dubonos, S. V.; Grigorieva, I. V.; Firsov, A. A. *Science* **2004**, *306*, 666.
19. Chhowalla, M.; Jena, D.; Zhang, H. *Nat. Rev. Mater.* **2016**, *1*, 16052.
20. Wang, X.; Sun, G.; Routh, P.; Kim, D. H.; Huang, W.; Chen, P. *Chem. Soc. Rev.* **2014**, *43*, 7067.
21. Song, X. J.; Sun, J. Y.; Qi, Y.; Gao, T.; Zhang, Y. F.; Liu, Z. F. *Adv. Energy Mater.* **2016**, *6*, 1600541.
22. Duan, X.; Wang, C.; Pan, A.; Yu, R.; Duan, X. *Chem. Soc. Rev.* **2015**, *44*, 8859.
23. Dávila, M. E.; Xian, L.; Cahangirov, S.; Rubio, A.; Lay, G. L. *New J. Phys.* **2014**, *16*, 095002.
24. Vogt, P.; De Padova, P.; Quaresima, C.; Avila, J.; Frantzeskakis, E.; Asensio, M. C.; Resta, A.; Ealet, B.; Le Lay, G. *Phys. Rev. Lett.* **2012**, *108*, 155501.
25. Makiura, R.; Konovalov, O. *Sci. Rep.* **2013**, *3*, 2506.
26. Xu, L.; Zhou, X.; Tian, W. Q.; Gao, T.; Zhang, Y. F.; Lei, S.; Liu, Z. F. *Angew. Chem. Int. Ed.* **2014**, *53*, 9564.
27. Liu, X.; Dai, L. *Nat. Rev. Mater.* **2016**, *1*, 16064.

Chapter II. Direct Solvothermal Synthesis of B/N Doped Graphene

Note: This chapter is partially and totally adapted with permission from "Direct solvothermal synthesis of B/N doped graphene", Angewandte Chemie International Edition 2014, 53(9), 2398. Copyright © 2014, WILEY-VCH Verlag.

2.1 Abstract

Boron/nitrogen co-doped graphene (BCN graphene) is directly synthesized from a reaction between CCl_4/BBr_3/N_2 in the presence of potassium. The reaction of CCl_4 with either BBr_3 or N_2 alone leads to a marginally doped graphene. On the other hand, there is a synergistic effect when CCl_4 is reacted with BBr_3 and N_2 together to yield BCN graphene. The resultant BCN graphene displays good dispersion stability in *N*-methyl-2-pyrrolidone (NMP), allowing for the fabrication of a field-effect transistor by solution casting, which displays an on/off ratio of 10.7 with an optical band-gap of 3.3 eV. Considering the scalability and solution processability, BCN graphene has a high potential for many practical applications.

2.2 Introduction

Since graphene was experimentally discovered in 2004,[1] it has been the focus of vigorous application research due to its outstanding properties such as high specific surface area,[2] good thermal and electrical conductivities,[3-4] superior optical properties,[5] and many more peculiar properties.[6-7] However, in order to take advantage of the outstanding properties of graphene in practice, development of feasible synthetic protocols and chemical modifications to provide multifunctionality and processability for specific applications becomes an important challenge. For example, chemical and/or physical doping, such as covalent doping of heteroatoms into the graphitic structure,[8] and physisorption of gases,[9] metals,[10-11] or organic molecules[12] on the surface of graphene, is useful for enhanced electrocatalytic activity in solar cells[13] and fuel cells[14] as well as controlling the band-gap state.[15] However, covalent introduction of heteroatoms into the graphitic framework is not feasible enough to tune the properties of graphene.[16]

Graphene is a semimetal with no band-gap.[17] As a result, it is not suitable for logic applications, because devices cannot be switched off. Therefore, graphene must be modified to produce a band-gap, if it is to be used in electronic devices. Various methods of making graphene-based field effect transistors (FETs) have been researched, including doping graphene,[18] tailoring a graphene like nanoribbon,[19] and by using boron nitride as a support.[20] Among the methods of controlling the band-gap of graphene, doping methods show the most promise of industrial feasibility. By co-doping boron and nitrogen into carbon nanotubes and graphene using a CVD process, semiconducting behavior was achieved.[21-22] It is believed that doping of graphene using a solvothermal method will produce similar semiconducting behavior.

Herein, we report an efficient method for the mass production of boron/nitrogen co-doped graphene nanoplatelets (BCN-graphene) via solvothermal reaction of carbon tetrachloride (CCl_4) and potassium (K) in the presence of BBr_3/nitrogen. Notably, this method is extremely limited for B-doping into the graphitic framework using BBr_3 by itself,[23] while it is feasible for boron/nitrogen co-doping in the presence of BBr_3 together with nitrogen. The resultant BCN-graphene nanoplatelets displayed on/off current ratio ~10.7 in a FET.

2.3 Materials and Instrumentation

Instrumentations. Themogravimetric analysis (TGA) was conducted on a TA Q600 (TA Instrument) under nitrogen at a heating rate of 10 °C min^{-1}. The surface area was measured by nitrogen adsorption-desorption isotherms using the Brunauer-Emmett-Teller (BET) method on Micromeritics ASAP 2504N. The field emission scanning electron microscopy (FE-SEM) was performed on FEI Nanonova 230 while the high-resolution transmission electron microscopy (HR-TEM) was carried out on a JEOL JEM-2100F (Cs) microscope operating at 200 kV. Low voltage Cs aberration-corrected transmission electron microscopy (Titan Cube G2 60-300, FEI), which was operated at 80 kV with monochromated electron beam, was used for ultra-high-resolution imaging of the BCN-graphene along with selected area electron diffraction (SAED) pattern and electron energy loss spectroscopy (EELS). The TEM specimen were prepared by dipping carbon micro-grids (Ted Pella Inc., 200 Mesh Copper Grid) into well-dispersed samples in NMP. X-ray photoelectron spectroscopy (XPS) spectra were recorded on a Thermo Fisher K-alpha XPS spectrometer. Elemental analysis (EA) was conducted with Thermo Scientific Flash 2000. Zeta-potential values were determined using a Malvern Zetasizer (Nano ZS, Malvern Instruments). X-Ray diffraction (XRD) powder patterns were recorded with a Rigaku D/MAZX 2500V/PC with Cu–Kα radiation (40 kV, 100 mA, λ = 1.5418 Å). Time-of-flight secondary ion mass spectrometry (TOF-SIMS; ION TOF SIMS 5) were performed at positive secondary ion mode with a pulsed Bi_1^+ cluster ion source (25 kV, 1.02 pA) as a primary beam. Raman spectra were taken with a He-Ne laser (532 nm) as the excitation source by using confocal Raman microscopy (Alpha 300S, WITec, Germany) with power of 0.5 mW, in conjunction with atomic force microscopy (AFM). UV-vis spectrum was recorded on a Perkin-Elmer Lambda 35.

2.4 Experimental Section

Caution: This reaction is too reactive and dangerous for explosion, so careful attention is needed.
For synthesized boron materials via Wurtz reaction, after putting the sliced potassium in the reactor, I dropped BBr_3 using syringe with few drops in the glove box. After few seconds, the reaction exploded with huge heat and sound. So, do not repeat this experiment in large quantity. And the reaction is extremely exothermic reaction and high reactive.

2.4.1 C-graphene

Freshly distilled carbon tetrachloride (CCl_4, 4.0 mL) as a carbon source and potassium (K, 7.10 g), 1.1 eq. based on the halogens, were put into a stainless-steel autoclave (volume of 250 mL) under a nitrogen atmosphere in the glove box. The reaction was run at 270 °C for 30 min.

2.4.2 BC-graphene

Freshly distilled carbon tetrachloride (CCl_4, 4.0 mL), potassium (K, 7.63 g), 1.1 eq. based on the halogens, and boron tribromide (BBr_3, 0.39 mL) were put into a stainless-steel autoclave under an argon atmosphere. The reaction was run at 270 °C for 30 min. (Caution: BBr_3 is toxic and corrosive.)

2.4.3 BCN-graphene

Freshly distilled carbon tetrachloride (CCl_4, 4.0 mL), potassium (K, 7.60 g), 1.1 eq. based on the halogens, and boron tribromide (BBr_3, 0.39 mL) were put into a stainless-steel autoclave under a nitrogen atmosphere. The reaction was run at 270 °C for 30 min. The product was dispersed in an HCl solution for one day with stirring to remove residual metals and potassium from the reactor. The solution was then filtered. All products were purified by Soxhlet extraction with acetone and distilled water for three days each. After purification, the filtered product was freeze-dried at −120 °C under reduced pressure (0.05 mmHg) for 2 days.

2.4.4 Preparation of BCN-graphene FET Devices

The BCN-graphene was dispersed in NMP at a concentration of 0.3 mg mL^{-1}. The solution was then centrifuged at 10,000 rpm for 2 h. The centrifugation was carried out 10 times to ensure a homogenous dispersion. The solution was then drop-cast on a SiO_2/silicon substrate. The substrate and deposited BCN-graphene were annealed at 900 °C for 2 h under an argon atmosphere with a 30 sccm Ar gas flow rate. The substrates were then coated with PMMA by spin coating, and floated on hydrofluoric acid (HF) solution (2%) to take off the PMMA-coated sample. The PMMA coated film was transferred to new SiO_2/silicon substrate. The PMMA support layer was removed by dipping into acetone for 2 min, followed by rinsing the substrate with freshly distilled acetone and drying at room temperature for 1 day. Next 40 nm of gold electrodes were prepared by e-beam lithography with channel dimensions of W/L = 10 (L = 500 nm). Finally, the fabricated devices were measured in N_2 atmosphere.

2.4.5 DFT Calculations

For computations, we used the Vienna *Ab initio* Simulation Package (VASP) to calculate the ground state of many electrons system in the frame work of density functional theory. The plane-wave basis set with an energy cut-off of 400 eV and the PBE-type gradient-corrected exchange-correlation potential were employed.

2.5 Results and Discussion

In order to optimize the reaction conditions and provide a baseline for later comparison, carbon-based graphene (C-graphene) was prepared by solvothermal reaction, using the so-called Wurtz reaction.[23-25] In brief, the reaction between alkyl halides (carbon tetrachloride in this work) and alkaline metals (potassium in this work) generates carbon radicals and precipitated alkaline metal halides (potassium chloride in this work) (Figure 2.1a). The carbon radicals then form carbon-carbon (C-C) bonds on the surface of the alkaline metal particles. The fast radical reaction is spontaneously driven by high thermodynamic energy gain (formation energy plus crystal lattice energy) from K-K and 2C-Cl to 2KCl and C-C bonds (inset, Figure 2.1a). The product (C-graphene) has a dark black color, indicating the formation of a graphitic structure, while the white KCl crystal deposited on the reactor wall (photograph, Figure 2.1a). The optimized reaction conditions for C-graphene were used for the synthesis of boron-doped graphene (BC-graphene) by adding BBr_3 under an argon atmosphere or for boron/nitrogen-doped graphene (BCN-graphene) by adding BBr_3 under a nitrogen atmosphere. It is important to note that the key difference of reaction condition between BC-graphene and BCN-graphene is the absence or presence of nitrogen.

The morphologies of C-, BC- and BCN-graphene appear to be similar to each other in both scanning electron microscope (SEM) and transmission electron microscope (TEM) images (Figures 2.2-2.4), and

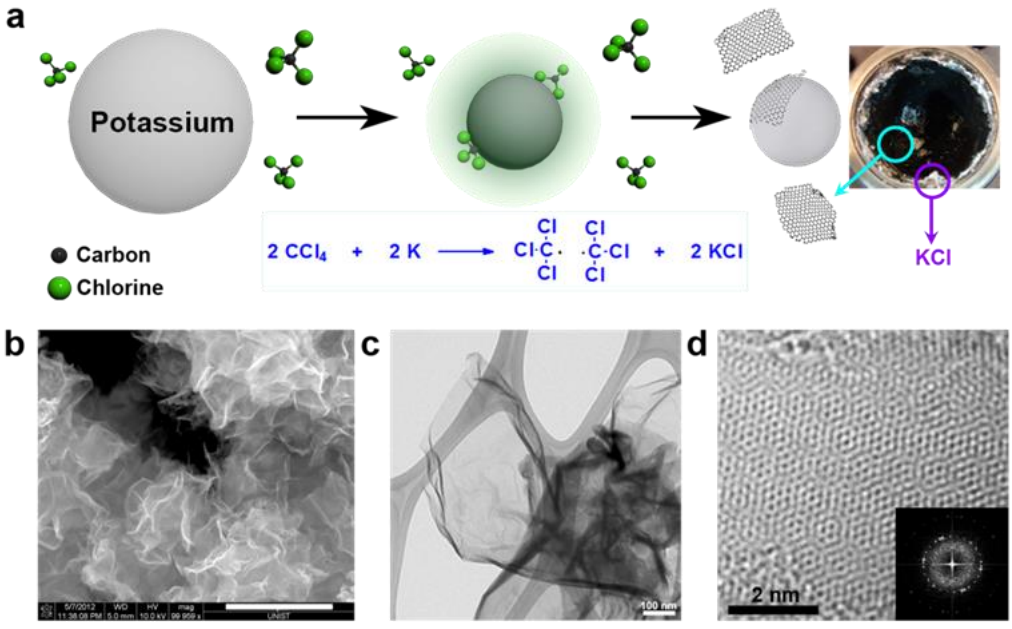

Figure 2.1. (a) A schematic representation for the formation of C-graphene *via* solvothermal reaction between carbon tetrachloride (CCl_4) and potassium (K). Photograph is of the autoclave after the reaction, showing the formation of C-graphene (black) and potassium chloride (KCl, white). (b) SEM image of BCN-graphene. Scale bar is 1 μm; (c) Bright field (BF) TEM image of BCN-graphene; (d) Atomic-resolution TEM image of BCN-graphene. Inset is a fast-Fourier transformed (FFT) pattern.

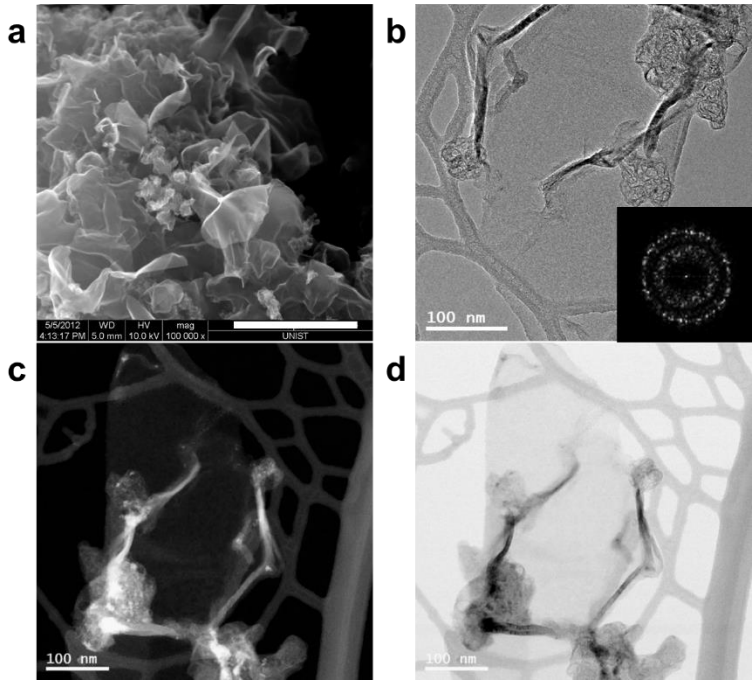

Figure 2.2. (a) SEM image of C-graphene. Scale bar is 1 μm. TEM images of C-graphene: (b) bright field (BF) image. Inset is the fast-Fourier transformed (FFT) pattern; (c, d) high-angle annular dark field (HAADF) and bright field (BF) images of scanning TEM (STEM)

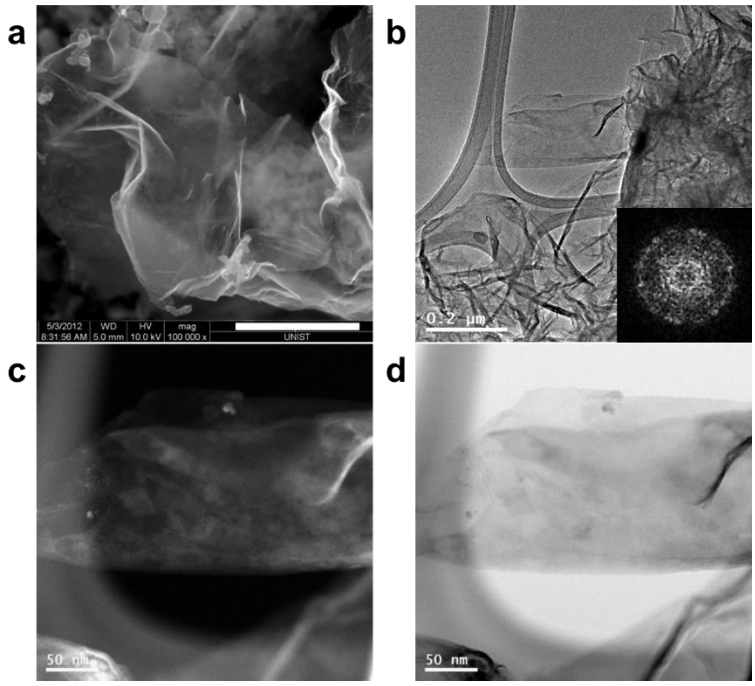

Figure 2.3. (a) SEM image of C-graphene. Scale bar is 1 μm. TEM images of BC-graphene: (b) bright field (BF) image. Inset is the fast-Fourier transformed (FFT) pattern; (c and d) high-angle annular dark field (HAADF) and bright field (BF) images of scanning TEM (STEM).

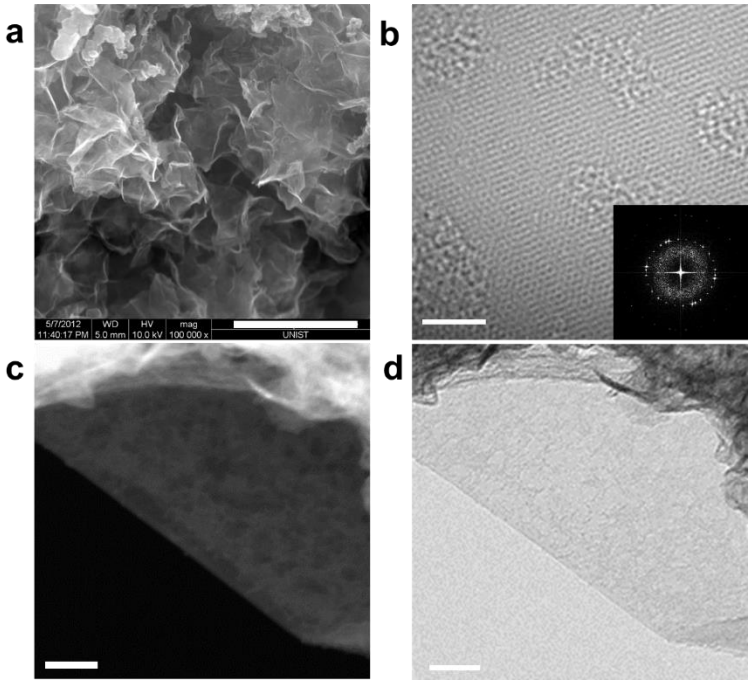

Figure 2.4. (a) SEM image of BCN-graphene. Scale bar is 1 μm. TEM images of BCN-graphene: (b) Atomic-resolution TEM image. Scale bar is 2 nm. Inset is the fast-Fourier transformed (FFT) pattern; (c and d) high-angle annular dark field (HAADF) of images of scanning TEM (STEM) and bright field (BF) image. Scale bars are 50 nm.

Table 2.1. XPS data of the samples

Sample	C (at.%)	B (at.%)	Br (at.%)	Cl (at.%)	N (at.%)	O (at.%)	C/B	C/N
C-graphene	92.46	BDL[a]	BDL[a]	1.05	0.59	5.90	NA[b]	182.2
BC-graphene	87.47	BDL[a]	0.28	1.28	0.73	10.07	NA[b]	139.7
BCN-graphene	84.41	2.38	BDL[a]	1.07	2.66	9.47	31.9	37.0

a. BDL = Below detection limit or not available.

b. NA = Not applicable.

those of BCN-graphene at low magnification show a crumpled and wrinkled sheet structure (Figures 2.1b and c and 2.4). At higher magnification (Figures 2.1d and 2.4b), BCN-graphene displayed a strong selected area electron diffraction (SAED) pattern, which suggests a highly crystalline structure (insets, Figures 2.1d and 2.4b).

The X-ray photoelectron spectroscopy (XPS) spectrum of C-graphene shows C 1s and O 1s peaks at

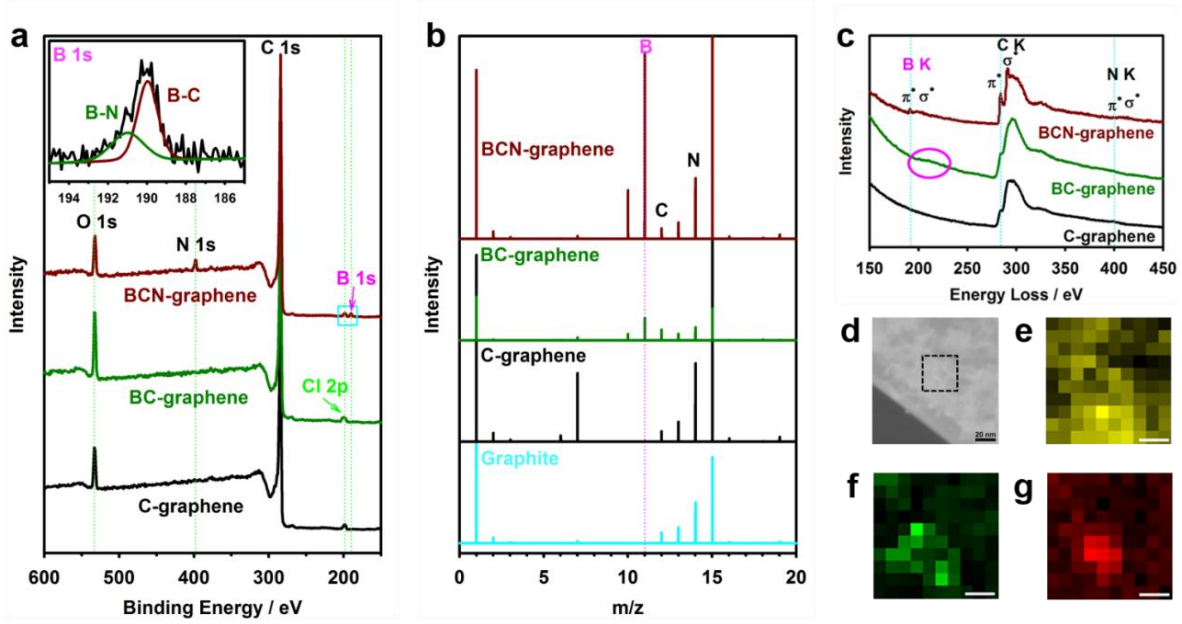

Figure 2.5. (a) XPS survey spectra of samples. Inset is high-resolution B 1s spectrum of BCN-graphene marked sky blue square in (a). (b) TOF-SIMS spectra. The nitrogen and oxygen peaks were observed in all samples due to chemically/physically attached nitrogen and oxygen. The spectrum from pristine graphite is provided as reference. (c) K-shell excitation of boron, carbon and nitrogen from EELS spectra of samples. The element mappings of BCN-graphene: (d) dark field TEM image and dotted region is mapping area with 20 nm of scale bars; (e) carbon; (f) boron; (g) nitrogen.

284 and 533 eV, along with a weak Cl 2p peak at 198 eV (Figure 2.5a and Table 2.1). It is of note that there is no detectable N 1s peak in C-graphene, implying that nitrogen was inert against carbon radicals during the reaction. The XPS survey spectrum of BC-graphene is almost identical to that of C-graphene with no detectable B 1s peak (0.0 at.%). While incorporation of boron in BC-graphene was detected by TOF-SIMS (Figure 2.5b), the results indicate that the introduction of boron or nitrogen into the graphitic structure is extremely difficult in the presence of only BBr_3 or nitrogen. However, BCN-graphene, which was prepared in the presence of both BBr_3 and nitrogen, exhibits B 1s (2.38 at.%) and N 1s (2.66 at.%) peaks centered at 190 and 398 eV in the XPS spectrum, as well as strong B and N peaks in the TOF-SIMS spectra (Figures 2.5a and b). By using the high-resolution B 1s peak, the ratio of B-C/B-N was determined to be approximately 2 (Inset, Figure 2.5a), which matches with the structural unit proposed in Figure 2.6d. Furthermore, electron energy-loss spectroscopy (EELS) roughly provided bonding state information as heteroatoms (B K- and N K-edges) and carbon (C K-edge) are connected with sp^2 hybridized structure (Figure 2.5c). EELS shows that each atom's bonding consists of 1s-π* and 1s-σ* bonding as observed in XPS spectrum (Inset, Figure 2.5a). Specifically, the EELS spectrum of BCN-graphene exhibits clear boron, carbon and nitrogen peaks at 190, 284 and 399 eV, while BC-graphene shows a marginally detectable B K-edge (pink circle, Figure 2.5c). All elements are sp^2

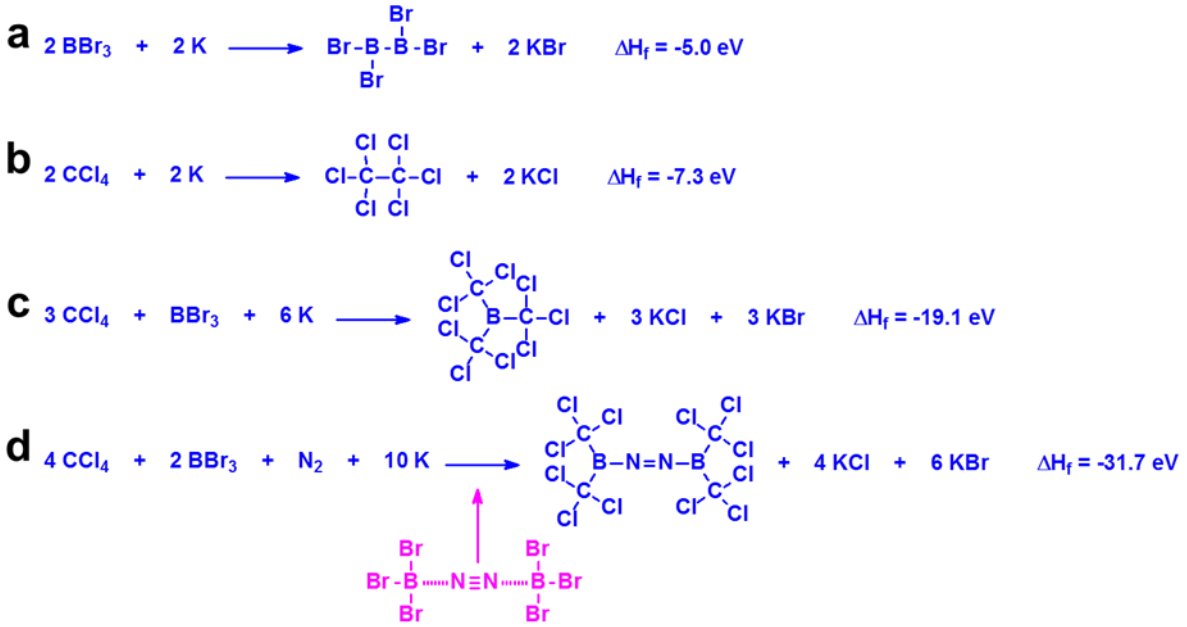

Figure 2.6. Schematic representations of energy gains (formation energy plus lattice energy) of chemical reactions: (a) the formation of B-B bond; (b) the formation of C-C bond; (c) the formation of B-C bond; (d) the formation of B-C *via* Br_3B-N=N-BBr_3 complex. The formation of Br_3B-N=N-BBr_3 complex *via* Lewis acid-base interaction between Lewis acid BBr_3 and Lewis base nitrogen.

hybridized due to having both π* and σ* bonding.[6] The distribution of boron, carbon, and nitrogen in the BCN-graphene sheet was mapped using elemental mapping (Figures 2.5d-g). It shows that the boron and nitrogen are co-doped in BCN-graphene sheet. The proposed acid-base interaction between B and N should be plausible mechanism for B/N co-doping into graphitic structure.[28] The proposed mechanism is that BBr_3 interacts with the nitrogen gas first and is then activated by the potassium to generate boron radicals, which subsequently react with carbon radicals to self-assemble into graphitic structure (Figure 2.6d). To support the experimental observation of efficient B/N co-doping in BCN-graphene, density functional theory (DFT) calculations were conducted and revealed that the formation energy and crystal lattice energy of the BCN-unit is the lowest among the possible unit reactions (Figure 2.7). Hence, for the co-doping of boron and nitrogen into graphitic framework, it is believed that there must be a synergistic contribution to the reaction. Similar to the stable borane-ammonia complex (H_3B-NH_3),[27] a possible scenario would be the acid-base interaction between BBr_3 (Lewis acid) and nitrogen (Lewis base) to yield Br_3B-N=N-BBr_3 intermediate complex (Figure 2.6), because BBr_3 has the highest Lewis acidity among boron trihalides (BX_3, X = F, Cl, Br). The in-situ formation of this complex could promote efficient B-N bond formation in the reaction system, which efficiently forms BCN-graphene.

To further investigate the structure of the BCN-graphene, Raman spectra were obtained from all powder samples (Figure 2.8a).[29] The normalized spectra of all samples display D and G bands at 1343 and 1580 cm^{-1}, which are associated with the degree of disorder and graphitic symmetry. In all cases,

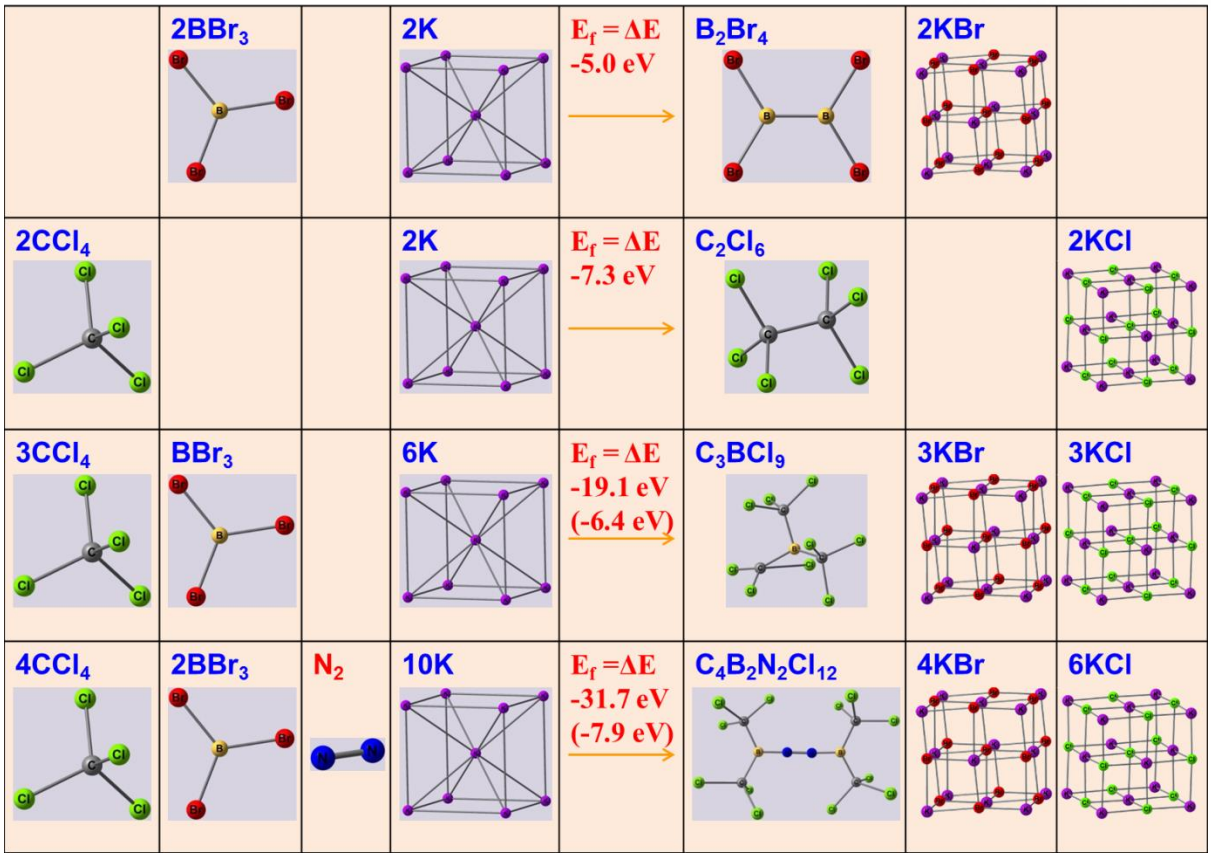

Figure 2.7. Summary of DFT calculations for formation energies of various chemical reactions: (a) the formation of B-B bond; (b) the formation of C-C bond; (c) the formation of B-C bond; (d) the formation of B-C *via* Br_3B-N=N-BBr_3 complex. The formation of Br_3B-N=N-BBr_3 complex *via* Lewis acid-base interaction between Lewis acid BBr_3 and Lewis base nitrogen. The number in parenthesis is the formation energy per unit chemical reaction.

2D peaks, which are related to the number of graphene sheets, are located at 2680 cm^{-1}. In the cases of C-, BC- and BCN-graphene, the I_D/I_G ratios are 0.95, 0.92 and 0.70 in that order, indicating that the defect ratios are generally higher than graphene produced from chemical vapor deposition (CVD).[30] The I_{2D}/I_G ratio is 1.35, which implies that C-graphene consists of few layers even in a solid powder. On the other hand, BC- and BCN-graphene have I_{2D}/I_G ratios of 0.67 and 0.62, indicating that they are composed of multilayers.

Thermogravimetric analysis (TGA) suggests that all samples are thermooxidatively stable up to 500 °C in air, indicating that graphitic networks have well-ordered structures (Figure 2.8b). X-ray diffraction (XRD) patterns show that the peaks (interlayer d-spacing) are located at 26.01° (3.42 Å) for C-graphene, 25.88° (3.44 Å) for BC-graphene and 25.94° (3.43 Å) for BCN-graphene, respectively (Figures 2.8c and d), which are lower (larger d-spacing) than the 26.54° (3.34 Å) for pristine graphite.[31] Furthermore, the relative peak intensities of (002) of C-, BC- and BCN-graphene were 0.72, 0.30, and

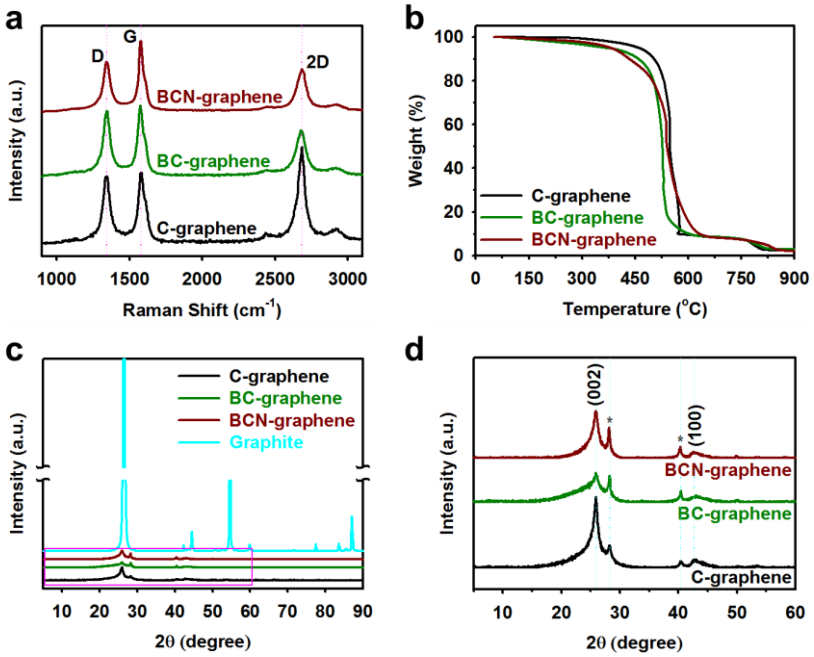

Figure 2.8. (a) Raman spectra of samples taken with a He-Ne laser (532 nm) as the excitation source; (b) TGA thermograms obtained with ramping rate of 10 °C min^{-1} in air; (c) XRD powder patterns of samples; (d) XRD patterns marked pink rectangle in (c). The asterisks indicate the trapped residue of KCl crystal.

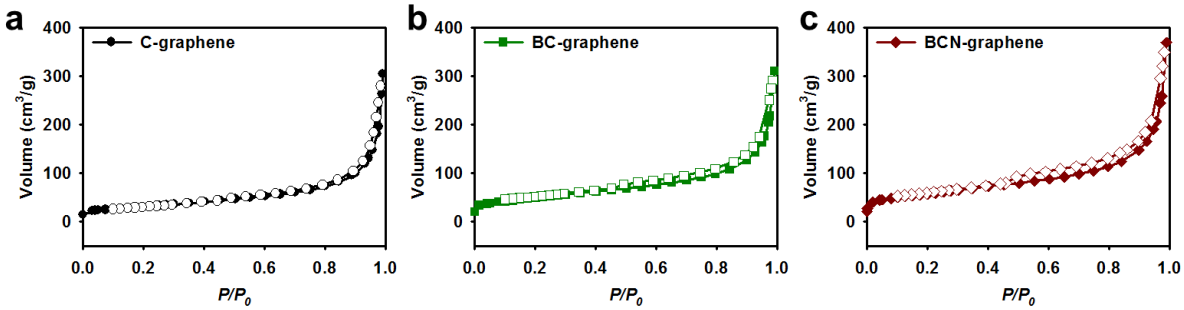

Figure 2.9. Nitrogen adsorption/desorption isotherms obtained and the calculation of pore size: (a) C-graphene; (b) BC-graphene; (c) BCN-graphene.

Table 2.2. BET surface areas of samples

Sample	Specific Surface Area (m^2 g^{-1})	Pore Volume (mL g^{-1})	Pore Size (nm)
C-graphene	109.16	0.47	17.27
BC-graphene	171.87	0.48	11.17
BCN-graphene	201.47	0.57	11.34

0.48% of that of pristine graphite, indicating that solvothermally synthesized graphene stays in crumpled and wrinkled forms (Figures 2.1b and c and Figures 2.3-4). As a result, efficient stacking is limited to form large number of graphitic layers.

The specific surface area, as determined by nitrogen adsorption/desorption isotherms, also increases in the order of C-graphene (109.2 $m^2 g^{-1}$), BC-graphene (171.9 $m^2 g^{-1}$) and BCN-graphene (201.5 $m^2 g^{-1}$; Figure 2.9 and Table 2.2). The values are well-correlated with the degree of crumples/wrinkles in the samples, which depends upon the doping states. It is supposed that doped heteroatoms in the graphitic carbon framework create not only a crumpled/wrinkled morphology but also provide active sites for efficient gas absorption by charge polarization. More interestingly, the dispersion stability of BCN-graphene in *N*-methyl-2-pyrrolidone (NMP) (Figure 2.10 and Table 2.3), which is the most crumpled/wrinkled and with highest surface area, is the best among the samples. BCN-graphene remains stable for two months, allowing easy fabrication of thin films and thus broad applications.

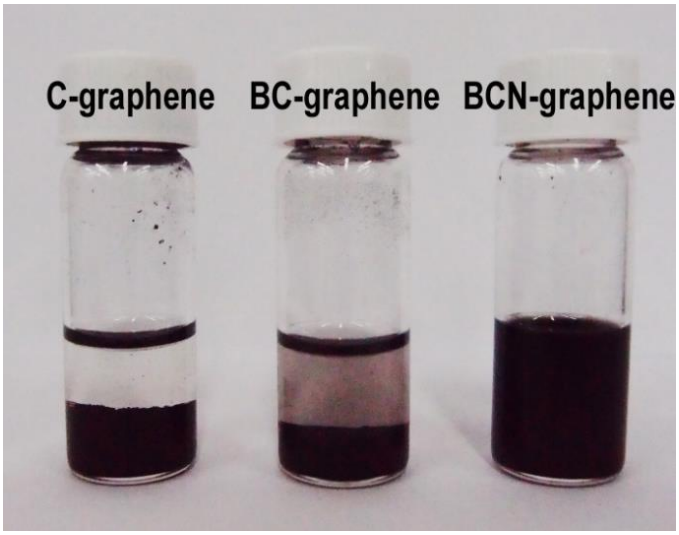

Figure 2.10. Dispersion stability of sample solutions in NMP standing at normal laboratory condition for two months. (concentration: 5 mg mL^{-1})

Table 2.3. Zeta-potentials of samples at different concentrations

Sample	Concentration (mg mL^{-1})			Particle Size (nm)
	0.10	0.05	0.02	
C-graphene	−18.7	−34.6	−40.3	300.1
BC-graphene	−29.8	−38.0	−38.9	311.6
BCN-graphene	−30.0	−37.1	−38.6	278.0

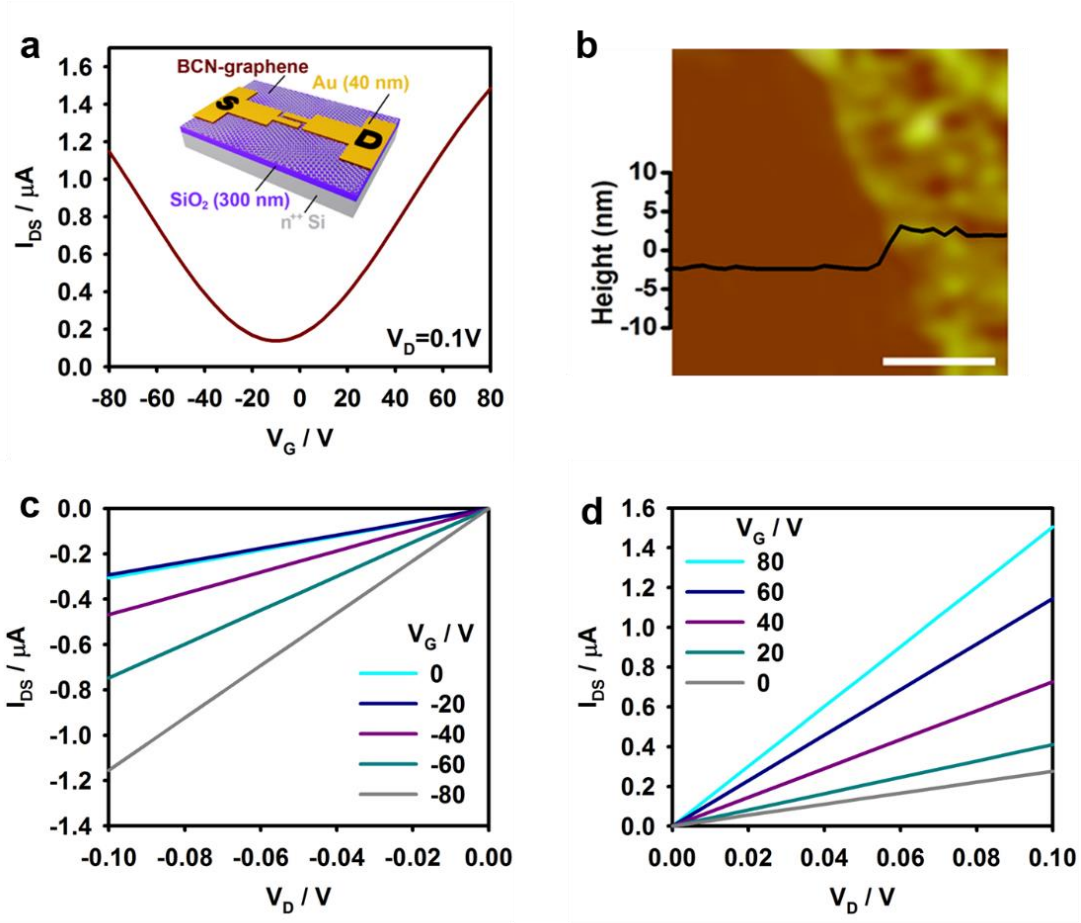

Figure 2.11. (a) The transfer curve of BCN-graphene FET at a drain voltage of 0.1 V. Inset image is schematic illustration of BCN-graphene FET; (b) a tapping-mode AFM image of BCN-graphene film on a SiO_2/Si wafer. The embedded graph is the thickness profile. The scale bar is 200 nm. Output curves of BCN-graphene FET at different gate voltages: (c) p-type output curves; (d) n-type output curves.

Table 2.4. Average electrical property of top-contact bottom-gate FET devices fabricated from BCN-graphene

Sample[a]	μ_e[b] ($cm^2\ V^{-1}\ s^{-1}$)	μ_h[c] ($cm^2\ V^{-1}\ s^{-1}$)	On/Off current ratio	Dirac point (V)
BCN-graphene	1.98 (±0.10)[d]	1.89 (±0.11)	10.4 (±0.4)	−9.6 (±0.05)

a. 20 devices were measured in N_2 atmosphere.

b. μ_e is a mobility of electron.

c. μ_h is a mobility of hole.

d. The standard deviation.

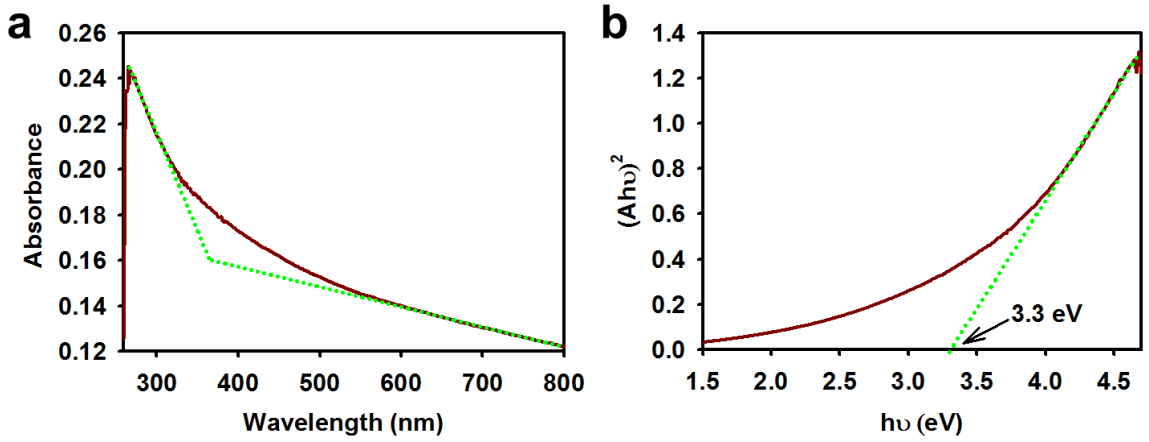

Figure 2.12. (a) UV-vis absorption spectrum of BCN-graphene (NMP used as the solvent), (b) Absorbance squared *vs*. the photon energy ($h\upsilon$) plotted as a function of energy of BCN-graphene shows a linear tendency for an indirect transition.

As an example, the fabrication of field-effect transistors (FETs) was performed with BCN-graphene (Inset, Figure 2.11a), which was dispersed in NMP and cast as a thin film on SiO_2 (300 nm)/silicon substrates with a thickness of approximately 4 nm (Figure 2.11b). The channel width-to-length ratio (W/L) of the FETs is 10 with L equal to 500 nm. The electronic properties of the BCN-graphene film as the active layers were measured. A typical transfer curve of BCN-graphene is displayed in Figure 2.11a. The hole and electron mobilities were calculated from the linear regime of the transfer properties resulting from the equation:

$$I_D = \mu \frac{W}{L} C_i V_D (V_G - V_{th})$$

where I_D is the drain current, μ is the field-effect mobility, C_i is the specific capacitance of the dielectric, V_D is the drain voltage, V_G is the gate voltage, V_{th} is the threshold voltage. Hole and electron mobilities were calculated at room temperature and a drain bias of 0.1 V from the transfer curve in Figure 2.11a and Table 2.4 resulting in values of 2.0 and 2.1 $cm^2V^{-1}s^{-1}$ respectively. The transfer curve shows ambipolar characteristics (Figures 2.11c and 2.11d). The low hole and electron mobilities resulted from the scattering at the junction by the stacking of individual BCN-graphene flake sheets. It was expected that by co-doping boron and nitrogen into the basal plane of graphene, the band-gap would increase, but the Dirac point would stay near 0 V due to charge neutralization between boron and nitrogen. However, in the case of BCN-graphene, the Dirac point was located at −10 V, showing an n-type behavior due to the slightly higher amount of nitrogen (2.66 at.%) as well as a much stronger electronegativity (χ = 3.04) than those of boron (2.38 at.% and χ = 2.04, respectively) (Table 2.1). The on/off current ratio was 10.7, which shows that the BCN-graphene behaves as a semiconductor. In addition, the optical band-gap is about 3.3 eV (Figure 2.12), further confirming the semiconducting behavior. Although graphene oxide and doped-graphene oxide films are easy to fabricate, it is difficult

to use as an n-type semiconductor with a band-gap opened.[32-35] BCN-graphene overcomes this difficulty while maintaining easy processability, which could offer many more practical applications.

2.6 Conclusions

In summary, boron/nitrogen co-doped graphene (BCN-graphene) was successfully prepared. During doping, it was discovered that boron and nitrogen have a synergistic effect when applied together, and that reaction with either boron or nitrogen alone did not lead to a high doping level. The dispersion stability of the graphene was improved via doping with boron and nitrogen leading to greater processability. In addition, the BCN-graphene demonstrated a 10.7 on/off ratio in a FET device, showing that it possesses semiconducting properties. Combined with the high dispersion stability, the BCN-graphene possesses a high potential for many practical applications.

2.7 References

1. Novoselov, K.; Geim, A. K.; Morozov, S.; Jiang, D.; Grigorieva, M. K. I.; Dubonos, S.; Firsov, A. *Nature* **2005**, *438*, 197.
2. Peigney, A.; Laurent, C.; Flahaut, E.; Bacsa, R.; Rousset, A. *Carbon* **2001**, *39*, 507.
3. Balandin, A. A.; Ghosh, S.; Bao, W.; Calizo, I.; Teweldebrhan, D.; Miao, F.; Lau, C. N. *Nano Lett.* **2008**, *8*, 902.
4. Bolotin, K. I.; Sikes, K.; Jiang, Z.; Klima, M.; Fudenberg, G.; Hone, J.; Kim, P.; Stormer, H. *Solid State Commun.* **2008**, *146*, 351.
5. Nair, R.; Blake, P.; Grigorenko, A.; Novoselov, K.; Booth, T.; Stauber, T.; Peres, N.; Geim, A. *Science* **2008**, *320*, 1308.
6. Bonaccorso, F.; Sun, Z.; Hasan, T.; Ferrari, A. *Nat. Photon.* **2010**, *4*, 611.
7. Lee, C.; Wei, X.; Kysar, J. W.; Hone, J. *Science* **2008**, *321*, 385.
8. Wang, H.; Maiyalagan, T.; Wang, X. *ACS Catalysis* **2012**, *2*, 781.
9. Schedin, F.; Geim, A.; Morozov, S.; Hill, E.; Blake, P.; Katsnelson, M.; Novoselov, K. *Nat. Mater.* **2007**, *6*, 652.
10. Varykhalov, A.; Scholz, M. R.; Kim, T. K.; Rader, O. *Phys. Rev. B* **2010**, *82*, 121101.
11. Liang, Y.; Li, Y.; Wang, H.; Zhou, J.; Wang, J.; Regier, T.; Dai, H. *Nat. Mater.* **2011**, *10*, 780.
12. Englert, J. M.; Dotzer, C.; Yang, G.; Schmid, M.; Papp, C.; Gottfried, J. M.; Steinrück, H.-P.; Spiecker, E.; Hauke, F.; Hirsch, A. *Nat. Chem.* **2011**, *3*, 279.
13. Sun, Y.; Wu, Q.; Shi, G. *Energy Environ. Sci.* **2011**, *4*, 1113.
14. Choi, H.-J.; Jung, S.-M.; Seo, J.-M.; Chang, D. W.; Dai, L.; Baek, J.-B. *Nano Energy* **2012**.
15. Wang, X.; Li, X.; Zhang, L.; Yoon, Y.; Weber, P. K.; Wang, H.; Guo, J.; Dai, H. *Science* **2009**, *324*, 768.
16. Sun, Z.; James, D. K.; Tour, J. M. *J. Phys. Chem. Lett.* **2011**, *2*, 2425.

17. Geim, A. K.; Novoselov, K. S. *Nat. Mater.* **2007**, *6*, 183.
18. Wei, D.; Liu, Y.; Wang, Y.; Zhang, H.; Huang, L.; Yu, G. *Nano Lett.* **2009**, *9*, 1752.
19. Li, X.; Wang, X.; Zhang, L.; Lee, S.; Dai, H. *Science* **2008**, *319*, 1229.
20. Britnell, L.; Gorbachev, R. V.; Jalil, R.; Belle, B. D.; Schedin, F.; Mishchenko, A.; Georgiou, T.; Katsnelson, M. I.; Eaves, L.; Morozov, S. V.; Peres, N. M. R.; Leist, J.; Geim, A. K.; Novoselov, K. S.; Ponomarenko, L. A. *Science* **2012**, *335*, 947.
21. Lu, J.; Zhang, K.; Feng Liu, X.; Zhang, H.; Chien Sum, T.; Castro Neto, A. H.; Loh, K. P. *Nat. Commun.* **2013**, *4*.
22. Xu, Z.; Lu, W.; Wang, W.; Gu, C.; Liu, K.; Bai, X.; Wang, E.; Dai, H. *Adv. Mater.* **2008**, *20*, 3615.
23. Chang, C.-K.; Kataria, S.; Kuo, C.-C.; Ganguly, A.; Wang, B.-Y.; Hwang, J.-Y.; Huang, K.-J.; Yang, W.-H.; Wang, S.-B.; Chuang, C.-H.; Chen, M.; Huang, C.-I.; Pong, W.-F.; Song, K.-J.; Chang, S.-J.; Guo, J.-H.; Tai, Y.; Tsujimoto, M.; Isoda, S.; Chen, C.-W.; Chen, L.-C.; Chen, K.-H. *ACS Nano* **2012**, *7*, 1333.
24. Lin, T.; Huang, F.; Liang, J.; Wang, Y. *Energy Environ. Sci.* **2011**, *4*, 862.
25. Choucair, M.; Thordarson, P.; Stride, J. A. *Nat. Nanotechnol.* **2008**, *4*, 30.
26. Lü, X.; Wu, J.; Lin, T.; Wan, D.; Huang, F.; Xie, X.; Jiang, M. *J. Mater. Chem.* **2011**, *21*, 10685.
27. Ci, L.; Song, L.; Jin, C.; Jariwala, D.; Wu, D.; Li, Y.; Srivastava, A.; Wang, Z.; Storr, K.; Balicas, L. *Nat. Mater.* **2010**, *9*, 430.
28. Niedenzu, K.; Dawson, J. W. *J. Am. Chem. Soc.* **1960**, *82*, 4223.
29. Shore, S. G.; Boddeker, K. W. *Inorg. Chem.* **1964**, *3*, 914.
30. Frrari, A.; Meyer, J.; Scardaci, V.; Casiraghi, C.; Lazzeri, M.; Mauri, F.; Piscanec, S.; Jiang, D.; Novoselov, K.; Roth, S. *Phys. Rev. Lett.* **2006**, *97*, 187401.
31. Bae, S.; Kim, H.; Lee, Y.; Xu, X.; Park, J.-S.; Zheng, Y.; Balakrishnan, J.; Lei, T.; Ri Kim, H.; Song, Y. I.; Kim, Y.-J.; Kim, K. S.; Ozyilmaz, B.; Ahn, J.-H.; Hong, B. H.; Iijima, S. *Nat. Nanotechnol.* **2010**, *5*, 574.
32. Jeon, I.-Y.; Choi, H.-J.; Ju, M. J.; Choi, I. T.; Lim, K.; Ko, J.; Kim, H. K.; Kim, J. C.; Lee, J.-J.; Shin, D.; Jung, S.-M.; Seo, J.-M.; Kim, M.-J.; Park, N.; Dai, L.; Baek, J.-B. *Sci. Rep.* **2013**, *3*.
33. Eda, G.; Fanchini, G.; Chhowalla, M. *Nat. Nanotechnol.* **2008**, *3*, 270.
34. Chang, D. W.; Lee, E. K.; Park, E. Y.; Yu, H.; Choi, H.-J.; Jeon, I.-Y.; Sohn, G.-J.; Shin, D.; Park, N.; Oh, J. H.; Dai, L.; Baek, J.-B. *J. Am. Chem. Soc.* **2013**, *135*, 8981.
35. He, Q.; Wu, S.; Gao, S.; Cao, X.; Yin, Z.; Li, H.; Chen, P.; Zhang, H. *ACS Nano* **2011**, *5*, 5038.
36. Lee, S.-K.; Jang, H. Y.; Jang, S.; Choi, E.; Hong, B. H.; Lee, J.; Park, S.; Ahn, J.-H. *Nano Lett.* **2012**, *12*, 3472.

Chapter III. B-doped Graphene as an Electrochemically Superior Metal-free Cathode Material as Compared to Pt over a Co(II)/Co(III) Electrolyte for Dye-sensitized Solar Cell

Note: This chapter is partially and totally adapted with permission from "B-doped graphene as an electrochemically superior metal-free cathode material as compared to Pt over a Co(II)/Co(III) electrolyte for dye-sensitized solar cell", Chemistry of materials 2014, 26(11), 3586. Copyright © 2014, American Chemical Society.

3.1 Abstract

We report that B-doped graphene (BG) is prepared and tested as counter electrode (CE) in dye-sensitized solar cells (DSSCs) in conjunction with $Co(bpy)_3^{2+/3+}$ redox couple. The BG CE has lower charge-transfer resistance and surpassing electrochemical stability than Pt CE. As the result, the DSSC with BG CE exhibits higher power conversion efficiency than the DSSC with Pt CE, suggesting possibility to replace Pt CE.

3.2 Introduction

As one of the most abundant and yet least collected sources of renewable energy, solar energy has attracted considerable interest in the areas of scientific research and industrial applications. Dye-sensitized solar cells (DSSCs), first developed two decades ago,[1] are considered to be one of the most promising photovoltaic devices among various photovoltaic systems. DSSCs have many advantages over other photovoltaic devices such as dye availability, easy and low-cost fabrication, high power conversion efficiency (PCE), and an environmental friendly nature.[2] A typical DSSC is constructed with three major components: a dye-coated TiO_2 film, a counter electrode (CE), and a redox-couple based electrolyte sandwiched between the two electrodes. The CE serves as an electrocatalyst for the reduction of a redox couple. Platinum (Pt) is thus far the most commonly used CE, due to its excellent electrocatalytic activity. However, because of high cost, low abundance in nature, and electrochemical instability, using Pt as a CE presents major drawbacks for large-scale production of DSSCs. Finding alternative CE materials to Pt with low manufacturing cost and high electrocatalytic activity with high stability is therefore an important challenge. There have been many attempts to replace the Pt electrocatalyst, and suggested substitutes include inorganic metal compounds,[3,4] conducting polymers,[5,6] and carbon-based materials.[7-15] Among them, carbon-based materials such as carbon black,[7] nanocarbons,[8] carbon nanotubes,[9,10] and graphene[11-16] have shown strong potential for use in practice in terms of availability at low cost and stability in corrosive electrolytes.

Doping heteroatoms (e.g., boron (B), nitrogen (N), and phosphorus (P)) into a graphitic carbon framework is an efficient way to activate graphene as an electrocatalyst in energy-related devices.[17] Doping N (its atomic radius of 70 pm) into a graphitic structure has been realized without difficulty[18] and N-doped graphene (NG) has demonstrated excellent electrocatalytic activity as CEs for DSSCs.[19-

[21] On the other hand, doping B into a graphitic carbon (C) network is very limited, due to atomic size mismatch between B (85 pm) and C (77 pm). There has only been one report on the synthesis and application of boron-doped graphene (BG) as a CE in a DSSC based on an I^-/I_3^- redox couple.[22] Meanwhile, the utilization of BG as a CE for DSSCs in conjunction with a $Co(bpy)_3^{2+/3+}$ redox couple (bpy = 2',2'-bipyridine) exhibited a higher open circuit voltage (V_{oc}) than the I^-/I_3^- redox couple has not been investigated.

3.3 Materials and Instrumentation

Time-of-flight secondary ion mass spectrometry (TOF-SIMS; ION TOF SIMS 5) were performed at positive secondary ion mode with a pulsed Bi_1^+ cluster ion source (25 kV, 1.02 pA) as a primary beam. Raman spectra were taken with a He-Ne laser (532 nm) as the excitation source by using confocal Raman microscopy (Alpha 300S, WITec, Germany) with power of 0.5 mW. The field emission scanning electron microscopy (FE-SEM) was performed on FEI Nanonova 230 while the high-resolution transmission electron microscopy (HR-TEM) was carried out on a JEOL JEM-2100F (Cs) microscope operating at 200 kV and electron energy loss spectroscopy (EELS). The TEM specimen were prepared by dropping the solution, well-dispersed samples in NMP, onto the carbon micro-grids (Ted Pella Inc., 200 Mesh Copper Grid). The surface area, pore volume and pore size were calculated by nitrogen adsorption-desorption isotherms using the Brunauer-Emmett-Teller (BET) method on BELSORP-max.

3.4 Experimental Section

3.4.1 Preparation of PG and BG

PG was prepared by freshly distilled carbon tetrachloride (CCl_4, 4.0 mL) as a carbon source and potassium (K, 7.10 g), 1.1 eq. based on the halogen. They were put into a stainless-steel autoclave (volume of 250 mL) under a nitrogen atmosphere in the glove box. The reaction was run at 270 °C for 30 min. BG was prepared by distilled 4.0 mL of carbon tetrachloride (CCl_4), potassium (K) 7.63 g, 1.1 eq. based on the halogens, and boron tribromide (BBr_3) 0.39 mL. They were put into a stainless-steel autoclave under an argon atmosphere. The reaction was run at 270 °C for 30 min. (Caution: BBr_3 is toxic and corrosive.) After the reactions, PG and BG were purified by Soxhlet extraction with acetone and distilled water for three days, respectively. After purification, the filtered product was freeze-dried at −120 °C for 2 days.

3.4.2 Preparation of BG and PG Electrodes

Homogeneously dispersed 0.1 wt% sample powders in 2-propanol solution were obtained by ultrasonication for 30 min. The resultant solution was deposited directly onto FTO/glass (TEC-8, Pilkington) using an e-spray technique. First, the sample dispersion solutions were loaded into a plastic syringe equipped with a 27-gauge stainless steel hypodermic needle. The needle was connected to a

high voltage power supply (ESN-HV30). A voltage of ~8.0 kV was applied between a metal orifice and the conducting substrate at a distance of 5.5 cm. The feed rate was controlled by the syringe pump (KD Scientific Model 220) at a constant flow rate of 150 μL min^{-1}. The electric field overcomes the surface tension of the droplets, resulting in the minimization of numerous charged mists. The sample electrodes were sintered at 300 °C for 30 min at atmosphere prior to device fabrication. The morphology of the sample electrodes was investigated using field emission scanning electron microscopy (FE-SEM, FEI Nanonova 230). For the reference, the Pt-FTO electrode was also prepared by deposition of *ca*. 30 μL cm^{-2} of H_2PtCl_6 solution (2 mg of H_2PtCl_6 in 1 mL of ethanol) and sintered at 400 °C for 15 min.

3.5 Results and Discussion

In this study, BG was prepared by the modified Wurtz reaction.[23-26] The reaction between carbon tetrachloride (CCl_4) and boron tribromide (BBr_3) was carried out in the presence of potassium (K) in a high-pressure reactor at 270 °C for 30 min under an argon atmosphere. For comparison, pristine graphene (PG) was also synthesized in the same reaction conditions without adding BBr_3. The experimental details for the synthesis and work-up procedure of BG and PG are described in Experimental section. Doping B in BG was first verified by using time-of-flight secondary ion mass spectrometry (TOF-SIMS) (Figure 3.1a). While BG shows the B peak at 11.0 m/z, natural graphite as a reference and PG do not show a boron peak, indicating that only BG contains boron. Electron energy-loss spectroscopy (EELS) meanwhile provides information on the bonding nature in BG. BG shows a sp^2 hybridized structure between B (B K edge) and carbon (C K edge) (sky blue circle, Figure 3.1b), implying the formation of C-B bonds in the graphitic structure. The structure of BG was further investigated in comparison with PG by using Raman spectroscopy. Raman spectra were obtained for powder samples of PG and BG (Figure 3.1c). Both samples show D and G bands at 1343 and 1576 cm^{-1}, which are related to the degree of disorder and graphitic symmetry. PG and BG exhibit similar peak intensity (I_D/I_G) ratios of 0.86 and 0.92, suggesting that the defect ratios of wet-chemically produced graphene are generally higher than those of graphene produced from chemical vapor deposition (CVD).[27] Interestingly, however, both PG and BG display strong 2D peaks at 2676 cm^{-1}, which are associated with the number of graphitic layers. The I_{2D}/I_G ratios of PG and BG are 1.07 and 0.62, indicating that they consist of a few graphitic layers.

The specific surface areas of PG and BG were calculated to nitrogen adsorption/desorption isotherms. Compared with natural graphite (2-4 m^2 g^{-1}), PG and BG displayed high specific surface areas of 180.8 m^2 g^{-1} and 318.0 m^2 g^{-1}, respectively (Figure 3.1d and e and Table 3.1). As observed from the high I_{2D}/I_G ratios, the results indicated that the PG and BG produced from solvothermal reactions remain at a high degree of exfoliation. Moreover, BG shows higher specific surface area than PG, BG shows higher specific surface area than PG, because the bond length mismatch between C-C and C-B bonds

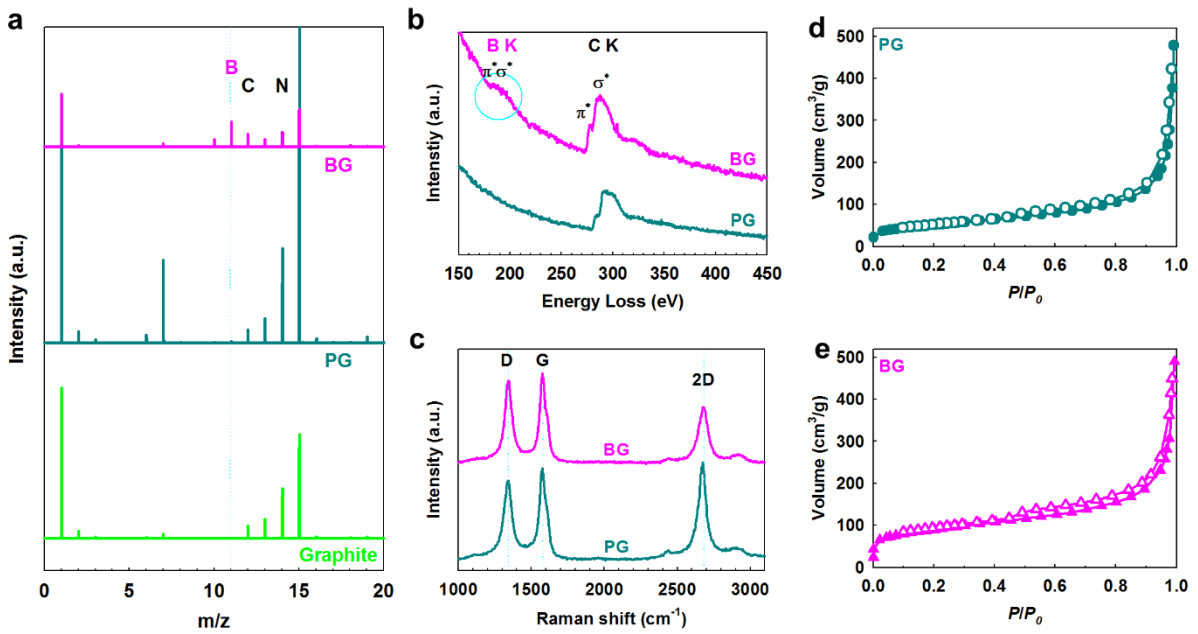

Figure 3.1. (a) TOF-SIMS spectra of PG, BG, and graphite. Graphite is a reference for comparison. (b) EELS spectra of boron and carbon K edge collected at PG and BG. (c) Raman spectra of PG and BG. (d and e) Nitrogen adsorption/desorption isotherms: (d) PG and (e) BG.

Table 3.1. BET surface areas of samples

Sample	Specific Surface Area ($m^2\ g^{-1}$)	Pore Volume ($mL\ g^{-1}$)	Pore Size (nm)
PG	180.77	0.70	15.49
BG	318.01	0.71	8.99

in the graphitic network generates a more wrinkled morphology and the polar nature of C-B bonds facilitates absorption of nitrogen gas. The electron-deficient B atom (χ = 2.04) has lower electronegativity than C (χ = 2.55). The relatively larger surface area and the more polar nature of BG are expected to provide active sites for efficient electrochemical activity.

The morphologies of PG and BG were further studied with a scanning electron microscope (SEM) and trans-mission electron microscope (TEM). SEM images of PG (Figure 3.2a) and BG (Figure 3.2b) are similar, showing wrinkled and crumpled sheet structures. TEM images of the bright field (BF) and high-angle annular dark field (HAADF) of samples from scanning TEM (STEM) for PG (Figure 3.3) and BG (Figure 3.4) are also similar. As expected, however, fast-Fourier transformed (FFT) patterns indicate that the crystallinity of PG (inset, Figure 3.2c) is higher than that of BG (inset, Figure 3.2d), due to the presence of B in the BG graphitic lattice. Edge-on view images demonstrate that PG and BG ~ 2-4 layers arrows), which is correlated by Raman spectroscopy and BET results (Figure 3. 1c).

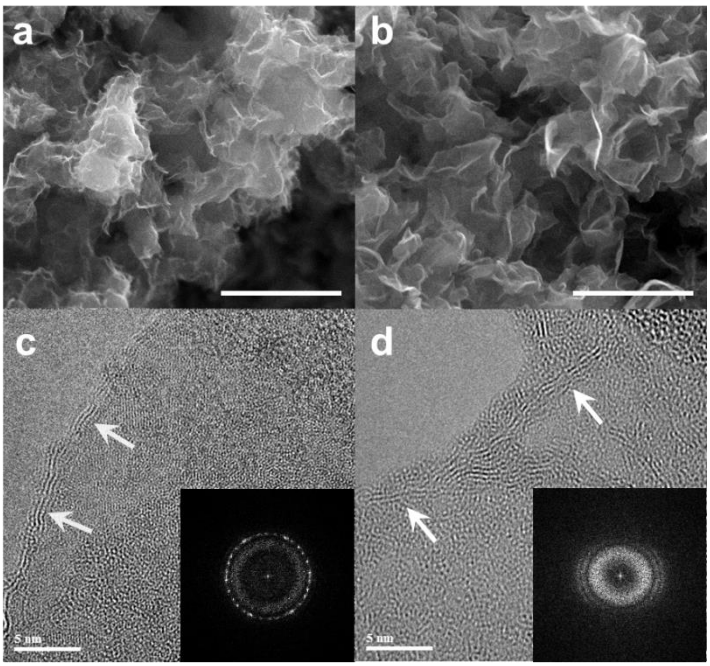

Figure 3.2. SEM images: (a) PG and (b) BG. Scale bars are 1 μm. TEM bright field (BF) images: (c) PG; (d) BG. Insets are fast-Fourier transformed (FFT) patterns.

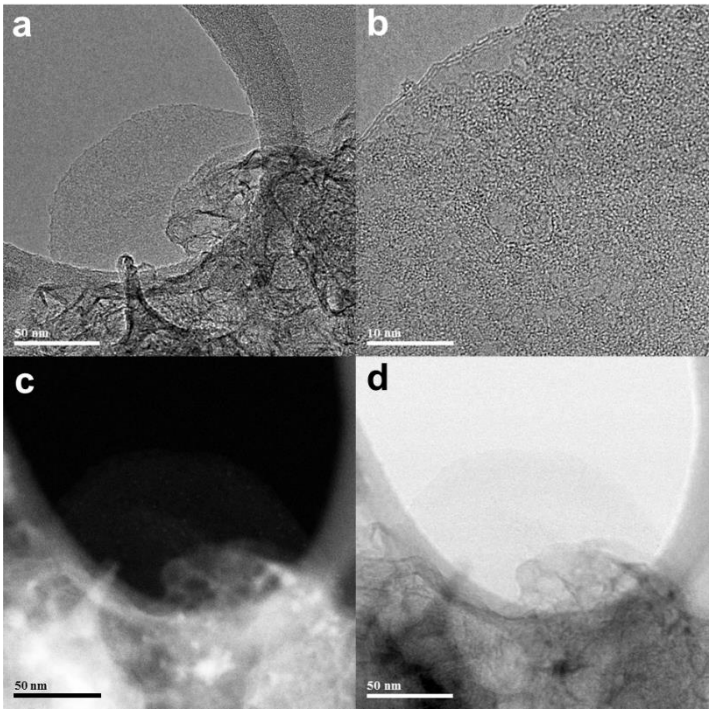

Figure 3.3. (a, b) TEM bright field (BF) images of PG. (c, d) High-angle annular dark field (HAADF) of images of scanning TEM (STEM) and BF image.

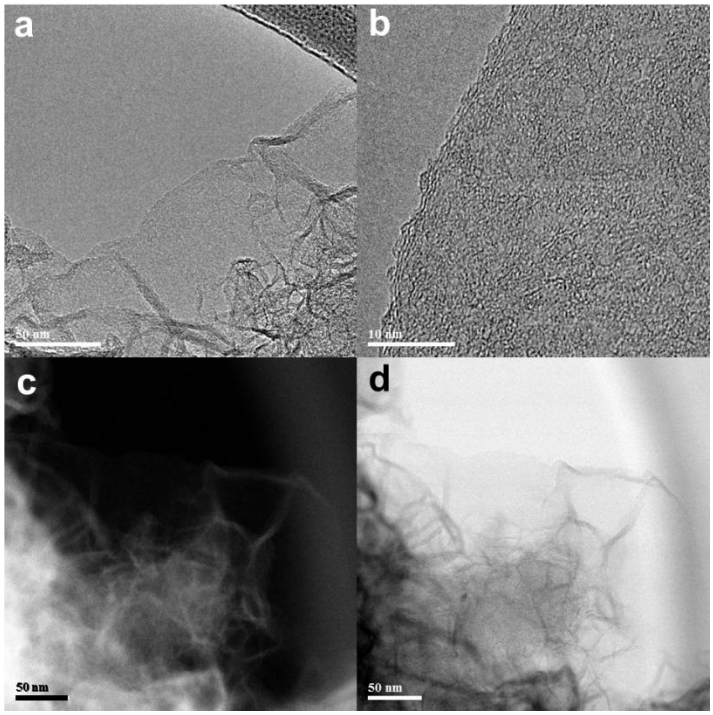

Figure 3.4. (a, b) TEM bright field (BF) images of BG. (c, d) High-angle annular dark field (HAADF) of images of scanning TEM (STEM) and BF image.

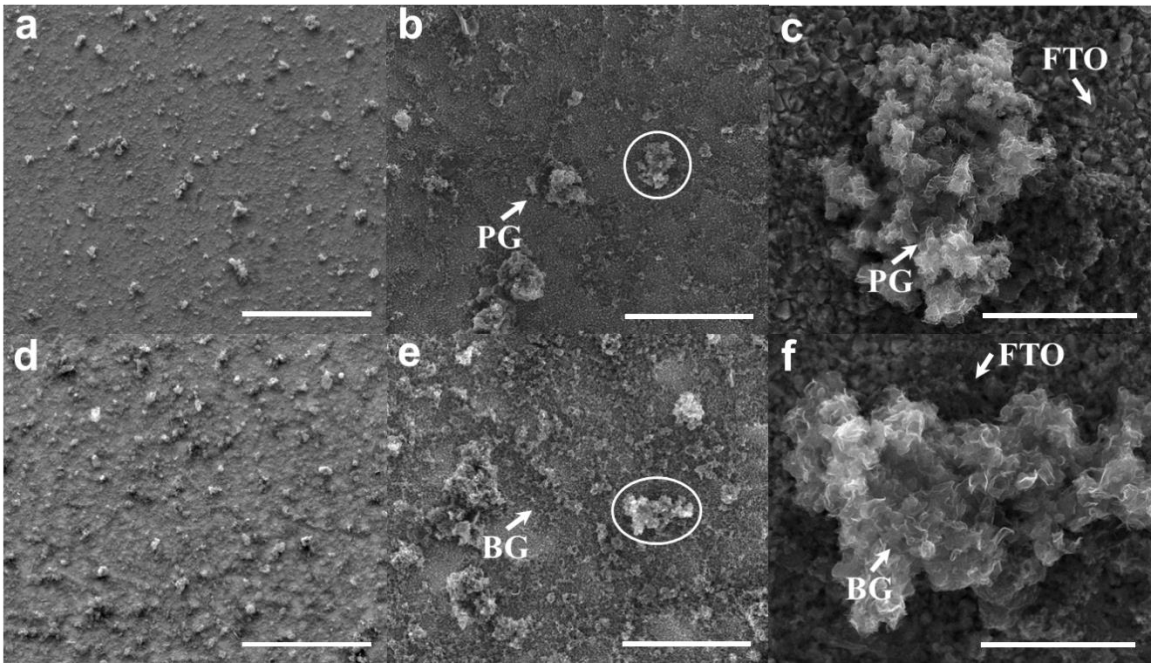

Figure 3.5. SEM images of PG and BG coated on FTO/glass substrates by e-spray: (a-c) PG with at different magnifications: (a) scale bar is 100 μm; (b) scale bar is 20 μm; and (c) scale bar is 4 μm. (d-f) BG with at different magnifications: (d) scale bar is 100 μm; (e) scale bar is 20 μm and (f) scale bar is 4 μm. Both samples are well covered on FTO surface with some aggregates (white ovals in (b) and (e)).

To evaluate the electrocatalytic activity of the PG and BG as CEs in DSSCs, thin films of these materials on fluorine-doped SnO_2 (FTO)/glass were prepared by using an electrostatic spray (e-spray) technique. The fabrication details are described in the ESI. The resultant electrodes were sintered at 300 °C for 30 min under a nitro-gen atmosphere prior to device fabrication. SEM images (Figure 3.5) of PG and BG on FTO show that the samples are well covered on the surfaces with some aggregates (white ovals in Figures 3.5b and e). For comparison, Pt ona FTO electrode was also fabricated, as described in the Experimental Section.

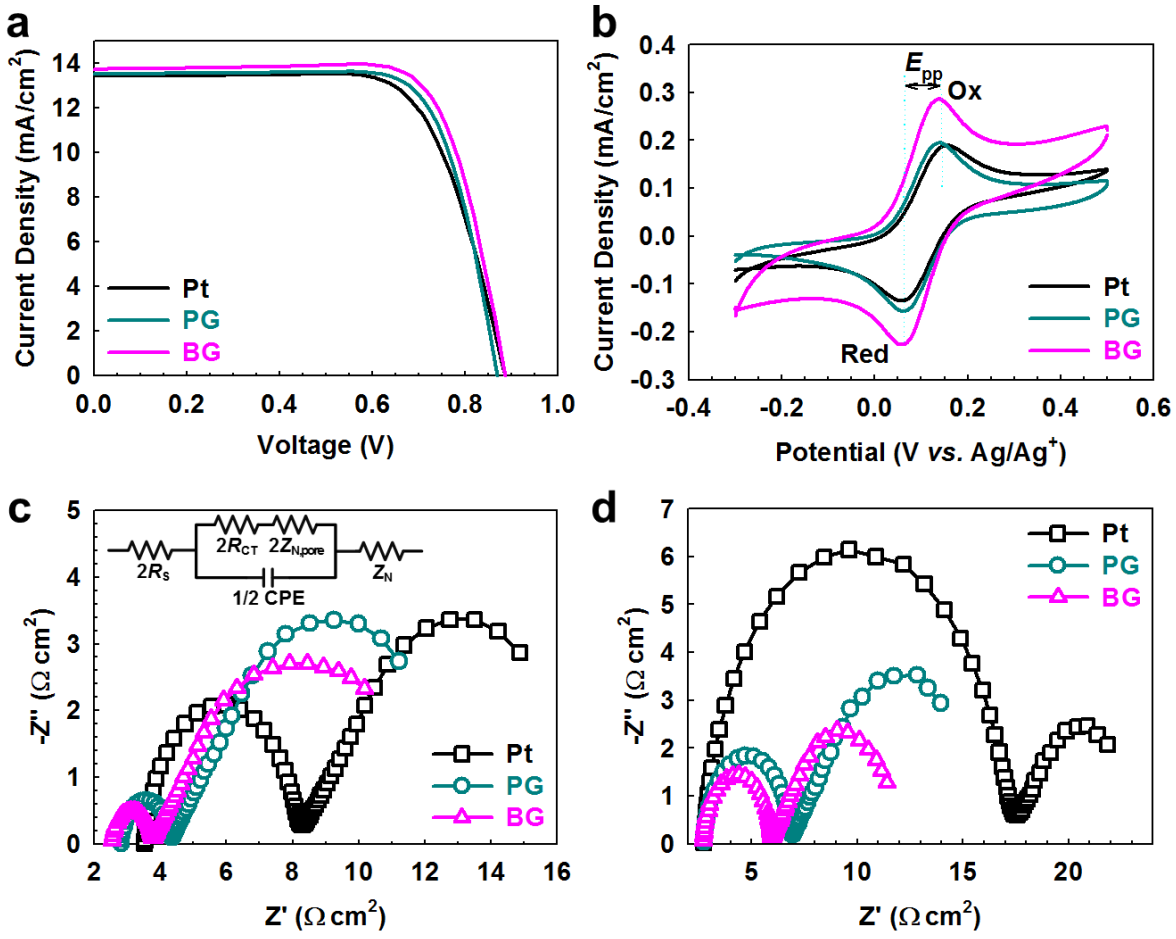

Figure 3.6. (a) Current-voltage characteristics of the DSSCs with Pt, PG, and BG CEs under one sun illumination (AM 1.5 G). The TiO_2 film thickness and active area are 9 (6 + 3) μm and 0.16 cm^2 with a black metal mask, respectively. (b) Cyclic voltammograms obtained at a scan rate of 10 mV s^{-1} for oxidation and reduction of the $Co(bpy)_3^{2+/3+}$ redox couple using Pt, PG, and BG electrodes as the working electrodes, a Pt wire as the CE, Ag/Ag^+ as the reference electrode, and 0.1 M $LiClO_4$ as the supporting electrolyte. (c) Nyquist plots measured at 0 V from 10^6 Hz to 0.1 Hz on symmetrical dummy cells with Pt, PG and BG electrodes. (d) Electrochemical stability of identical dummy cells after 100 cycling potentials (e.g. 100 × CV scans (from 0 V → 1 V → −1 V → 0 V at a scan rate of 50 mV s^{-1})).

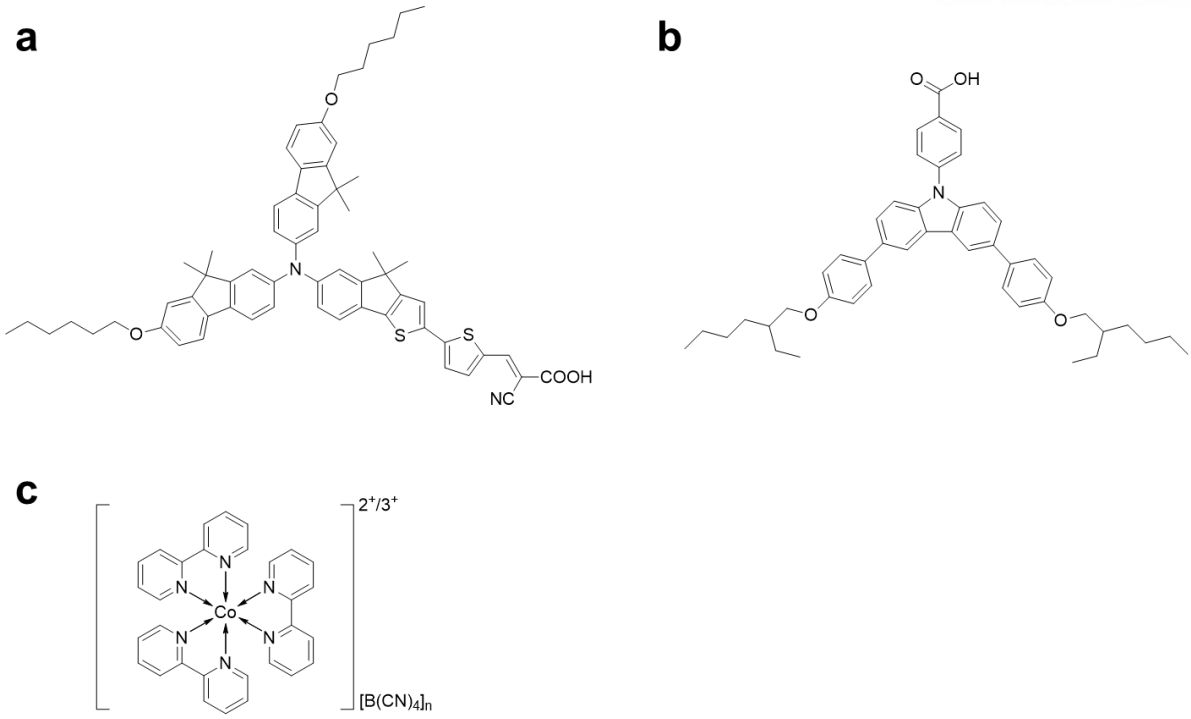

Figure 3.7. Chemical formulas: (a) JK-303 dye; (b) HC-A (SGT-301); (c) $Co(bpy)_3^{2+/3+}$ redox couple.

Given structural identification of PG and BG, the catalytic activities of the sample electrodes as CEs in actual devices were also evaluated in a $Co(bpy)_3^{2+/3+}$ redox couple exhibiting higher redox potential in a DSSC with an organic sensitizer (JK-303)[28] and a multi-functional coadsorbent of HC-A (SGT-301, see Figure 3.7).[29-32] Figure 3.6a presents the photocurrent-voltage (*J-V*) characteristics of the DSSCs with different CEs. As can be seen in the figure, the Pt-based DSSC exhibited a short-circuit current density (J_{sc}) of 13.44 mA cm^{-2}, an open-circuit voltage (V_{oc}) of 885 mV, a fill factor (FF) of 71.0%, and a power conversion efficiency (PCE) of 8.45%. The PG-based DSSC showed an even higher J_{sc} of 13.51 mA cm^{-2}, a V_{oc} of 869 mV, a FF of 74.9% and a PCE of 8.80%. On the other hand, photovoltaic performance values of the BG-based DSSC were 13.73 mA cm^{-2}, 887 mV, 75.6% and 9.21%, respectively. The J_{sc} and FF values of the BG-based DSSC are also higher than those of the Pt- and PG-based DSSCs. Replacement of the Pt CE with the BG CE evidently enhances efficiency, which is attributed to the improvement of J_{sc} and FF. Given that the same photoanode and electrolyte were used and only the CEs (Pt, PG and BG) were varied to fabricate DSSCs for this comparison, the variation in the device performance can be ascribed to the electrocatalytic performance of the CE materials.

To understand the differences in performance among the DSSCs, electrocatalytic activity of the CEs used in this study was evaluated by cyclic voltammetry (CV) and electrochemical impedance spectroscopy (EIS) analyses. Figure 3.6b compares the CV curves of the $Co(bpy)_3^{2+/3+}$ redox couple on Pt, PG, and BG electrodes, respectively. A typical pair of oxidation and reduction peaks (O_x and R_{ed}, as denoted in Figure 3.6b) are well resolved in the range of −0.4 to 0.6 V (*vs*. Ag/Ag$^+$). The peak-to-peak

separation (E_{pp}) for a pair peak and the peak currents are two important parameters for comparing catalytic activities of different CEs. A smaller E_{pp} and larger peak currents indicate higher catalytic performance. The E_{pp} is 0.095, 0.083 and 0.081 V for the Pt, PG and BG electrodes, respectively. The cathodic peak currents for the reduction of $Co(bpy)_3^{3+}$ are 0.14, 0.16 and 0.23 mA cm^{-2} for Pt, PG and BG, respectively. Compared to the Pt electrode, the BG electrode exhibits narrower E_{pp} and larger peak current density. This indicates that the reduction rate of $Co(bpy)_3^{3+}$ to $Co(bpy)_3^{2+}$ on the BG electrode surface is faster than that on the Pt counterpart.

To avoid electron losses in the TiO_2 photoanode in the DSSC, a redox shuttle reduction rate should be comparable to the rate of dye regeneration at the TiO_2 photoanode. This is given by the flux of electrons from the photoexcited dye to the conduction band of TiO_2, and is expressed by the photocurrent density (J_{sc}). Therefore, the exchange current density (J_0) should be comparable to J_{sc} to avoid electron losses at the CE. J_0 is expressed as follows:[33]

$$J_0 = \frac{RT}{nFR_{CT}} = Fk_0(c_{ox}^{1-\alpha} \times c_{red}^{\alpha}) \quad (1)$$

where R is the gas constant, T is the temperature, n is number of electrons contributing to charge transfer at the interface, and F is Faraday's constant. k_0 is the formal rate constant of the electrode reaction, c_{ox} and c_{red} are concentrations of oxidized and reduced shuttle, respectively, and α is the charge-transfer coefficient (α ≈ 0.5). The rate constant k_0 is assumed at equilibrium conditions; i.e. the rates of the anodic reaction and cathodic reactions are identical. Charge-transfer resistance (R_{CT}) at the CE/electrolyte interface is most conveniently carried out using electrochemical impedance spectroscopy (EIS) on a model system, so call ed symmetrical dummy cell, which mimics the structure of the DSSC.[34] Figure 3.6c illustrates the Nyquist plots of the EIS spectra of dummy cells fabricated with the aforementioned CEs. The corresponding equivalent circuit (EC) model fitting the EIS spectra (inset, Figure 3.6c). In this model, R_S is the ohmic series resistance, R_{CT} is the charge-transfer resistance, and Z_N is the Nernst diffusion impedance in the bulk electrolyte solution. The model also includes a constant phase element (CPE) describing deviation from the ideal capacitance due to the surface roughness of the electrodes. In addition, for highly porous electrodes, such as carbons and/or nanomaterials, the variable $Z_{N,pore}$ is introduced in this case to represent the effect of the second Nernst diffusion process. To account for this effect, the so called effective charge-transfer resistance (R_{CT}) is introduced:[35]

$$\mathcal{R}_{CT} = R_{CT} + Z_{N,pore} \quad (2)$$

It is considered that two main factors affecting the efficiency of a DSSC are the mass transport of the redox couple in the bulk electrolyte solution and that within the structural porosity of the electrode. These factors are particularly critical for large redox messengers such as Co-complex-based redox couples, which generally suffer from slow diffusion through nanomaterials with high porosity.[36] In Figure 3.6c, EIS spectra show two distinct semicircles corresponding to charge-transfer resistance (R_{CT})

at high frequency and the Nernst diffusion impedance (Z_N) of the $Co(bpy)_3^{2+/3+}$ redox couple in the electrolyte solution at low frequency regions, respectively. In the present study, $Z_{N,pore}$ at the porous PG and BG electrodes can be neglected because similar semicircles were observed with the Pt CE surface, where the catalytic reaction occurs on the vertically nonporous Pt surface.[37] Moreover, as demonstrated by potential-step chronoamperometry measurements, the BG electrode reached the steady-state current by a diffusion-limited interfacial charge-transfer process more quickly after the potential stepping, compared with the Pt counterpart (Figure 3.8.). Therefore, the R_{CT} itself is the effective charge-transfer resistance. The R_{CT} values according to the EC (inset of Figure 3.6c) were calculated as 2.39, 0.75 and 0.57 W cm^2 for Pt, PG and BG electrodes, respectively.

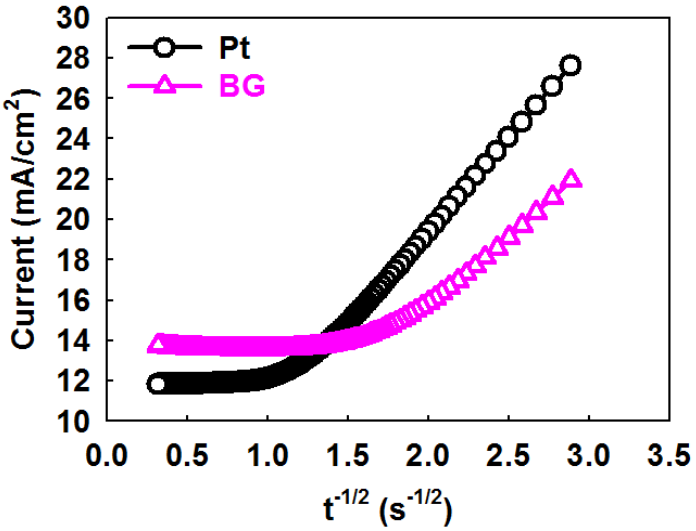

Figure 3.8. Potential-step chronoamperometry curves on symmetrical dummy cells with the Pt and BG electrodes. Potential was from 0 to 0.8 V for 10 s.

As R_{CT} correlates inversely with the electrocatalytic performance (equation. 1), BG electrode exhibited the highest electrocatalytic activity, and was favorable for fast electron diffusion, which is helpful to improve the electrocatalytic activity. Considering that the photoanode and electrolyte were fabricated under the same conditions, the charge transfer from the electrocatalyst to $Co(bpy)_3^{3+}$ must be the limiting step for photocurrent generation in DSSCs. As the R_{CT} for BG is smaller than that for Pt and PG, the J_0 value of the BG electrode is much higher than those of the Pt and PG electrodes. The electrocatalytic activity, quantified as J_0 or $1/R_{CT}$, (equation. 1), was found to be larger by a factor of about 4.19 for the BG electrode compared to that for the Pt electrode. The values of $c_{ox}^{1-\alpha}$ and c_{red}^{α} (equation. 1) are the same for all electrodes. Hence, the enhancement of J_0 in BG electrode is due to its higher electrocatalytic performance rather than a concentration effect.

The Tafel-polarization curves of symmetrical dummy cells with Pt and BG electrodes are presented

in Figure 3.9. They display the current density (J) as a function of voltage (V) at room temperature for the oxidation/reduction of $Co(bpy)_3^{3+}$ to $Co(bpy)_3^{2+}$. The slope of a tangent to the BG curve is higher than that of Pt, indicating that the BG shows a larger J_0. This is also in good agreement with the aforementioned EIS measurements in terms of equation (1). Therefore, a DSSC based on a BG CE with smaller R_{CT} or larger J_0 can yield higher J_{sc} than cells with Pt and PG Ces slightly increased to 1.44 and 1.66 W cm^2, respectively, whereas the Pt was remarkably increased up to 7.21 Ω cm^2. The much slower and milder deterioration of BG and PG than Pt clearly demonstrated much higher stability of BG and PG in the $Co(bpy)_3^{2+/3+}$ medium. A similar electrochemical stability was reported for the $Co(bpy)_3^{2+/3+}$/NGnP interface, and was ascribed to poisoning of Pt.[38] Thus, the BG CE exhibited better electrochemical stability compared to the PG and Pt electrodes in the $Co(bpy)_3^{3+/2+}$ medium.

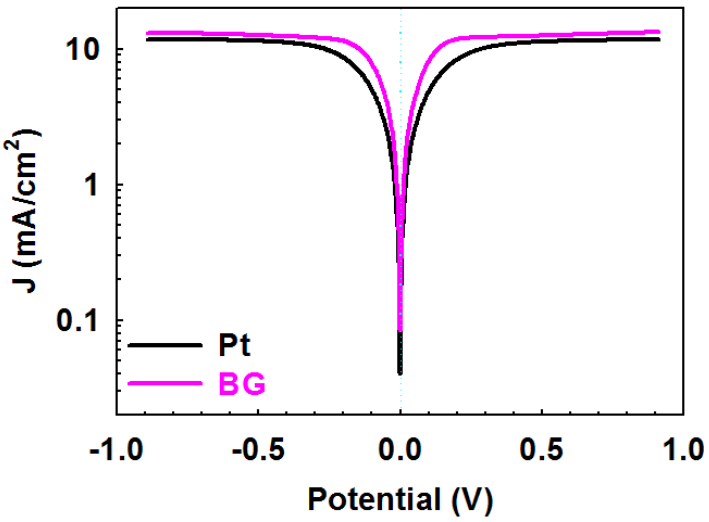

Figure 3.9. Tafel-polarization curves of the symmetrical cells fabricated with two identical BG and Pt electrodes at room temperature.

Table 3.2. Photovoltaic performance of DSSCs with different CEs

CE	J_{SC} (mA cm^{-2})	V_{OC} (mV)	FF (%)	PCE (%)
Pt	13.44	885	71.1	8.45
PG	13.51	869	74.9	8.80
BG	13.73	887	75.6	9.21

Finally, to further understand the improved performance of the DSSCs with different CEs, EIS measurements were carried out on the DSSC devices. The full- and high-frequency regions of the Nyquist plots of the DSSCs with different CEs are shown in Figure 3.10. The first semi-circle of the DSSC with PG is somewhat smaller than that of the Pt CE, while that of BG is significantly decreased. From the high-frequency region, the R_S and R_{CT} calculated with an appropriate equivalent circuit (EC, inset of Figure 3.10b) of the BG-based DSSC are 1.86 and 1.41 Ω cm^2, respectively, whereas the corresponding values of the Pt CE are 1.89 and 2.84 Ω cm^2. The lower R_{CT} value for the BG suggests high electrocatalytic activity for the reduction of $Co(bpy)_3^{3+}$ ions, which could enhance the DSSC performance, in particular, *FF* and J_{SC} (Table 3.2).

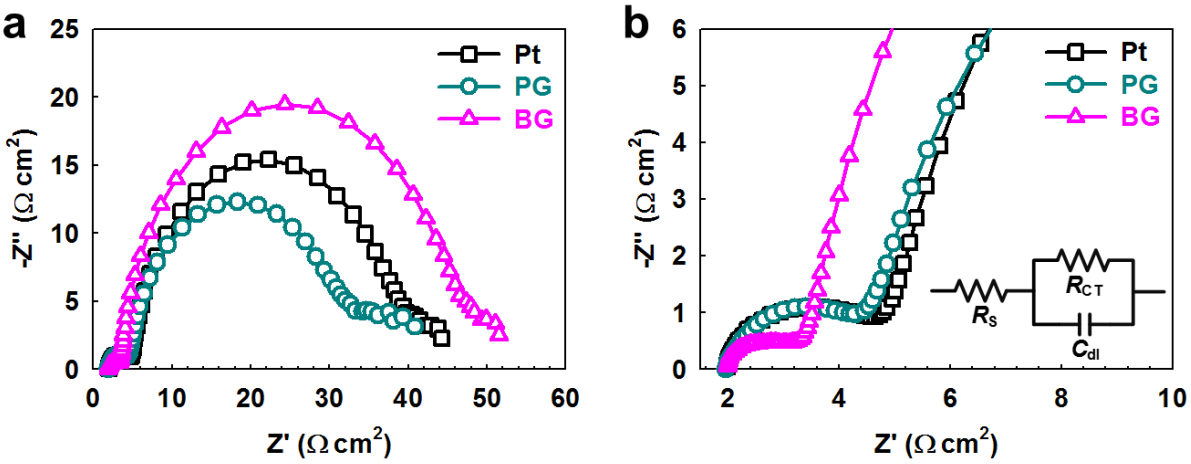

Figure 3.10. Nyquist plots in the full-frequency range (a) and high-frequency region (b) of DSSCs with different CEs at a forward bias of −0.85 V under dark conditions. The inset shows the equivalent circuit for fitting at the high-frequency region.

3.6 Conclusions

In summary, boron-doped graphene (BG) as a counter electrode (CE) was, for the first time, applied to dye-sensitized solar cells (DSSCs) in conjunction with $Co(bpy)_3^{2+/3+}$ redox couple. The BG CE exhibits superior electrocatalytic activities to the Pt CE in $Co(bpy)_3^{3+}$ redox couple. Specifically, the BG CE shows lower charge-transfer resistance and better electrochemical stability. As a result, the DSSC fabricated with the BG CE produces higher power conversion efficiency (9.21%) than the DSSCs with the PG (8.80%) and Pt CEs (8.45%). The results presented in this work suggest that BG is a promising low-cost and high-performance cathode material for application in DSSCs based on Co-complex redox couples.

3.7 References

1. O'Regan, B.; Gratzel, M. *Nature* **1991**, *353*, 737.
2. Hagfeldt, A.; Boschloo, G.; Sun, L.; Kloo, L.; Pettersson, H. *Chem. Rev.* **2010**, *110*, 6595.
3. Li, G. R.; Song, J.; Pan, G. L.; Gao, X. P. *Energy Environ. Sci.* **2011**, *4*, 1680.
4. Xin, X.; He, M.; Han, W.; Jung, J.; Lin, Z. *Angew. Chem. Int. Ed.* **2011**, *50*, 11739.
5. Tai, Q.; Chen, B.; Guo, F.; Xu, S.; Hu, H.; Sebo, B.; Zhao, X.-Z. *ACS Nano* **2011**, *5*, 3795.
6. Wang, H.; Feng, Q.; Gong, F.; Li, Y.; Zhou, G.; Wang, Z.-S. *J. Mater. Chem. A* **2013**, *1*, 97.
7. Murakami, T. N.; Ito, S.; Wang, Q.; Nazeeruddin, M. K.; Bessho, T.; Cesar, I.; Liska, P.; Humphry-Baker, R.; Comte, P.; Péchy, P. *J. Electrochem. Soc.* **2006**, *153*, A2255.
8. Jia, R.; Chen, J.; Zhao, J.; Zheng, J.; Song, C.; Li, L.; Zhu, Z. *J. Mater. Chem.* **2010**, *20*, 10829.
9. Yang, Z.; Chen, T.; He, R.; Guan, G.; Li, H.; Qiu, L.; Peng, H. *Adv. Mater.* **2011**, *23*, 5436.
10. Han, J.; Kim, H.; Kim, D. Y.; Jo, S. M.; Jang, S.-Y. *ACS Nano* **2010**, *4*, 3503.
11. Hong, W.; Xu, Y.; Lu, G.; Li, C.; Shi, G. *Electrochem. Commun.* **2008**, *10*, 1555.
12. Choi, H.; Kim, H.; Hwang, S.; Han, Y.; Jeon, M. *J. Mater. Chem.* **2011**, *21*, 7548.
13. Xu, Y.; Bai, H.; Lu, G.; Li, C.; Shi, G. *J. Am. Chem. Soc.* **2008**, *130*, 5856.
14. Kavan, L.; Yum, J. H.; Gratzel, M. *ACS Nano* **2011**, *5*, 165.
15. Jang, S. Y.; Kim, Y. G.; Kim, D. Y.; Kim, H. G.; Jo, S. M. *ACS Appl. Mater. Interfaces* **2012**, *4*, 3500.
16. Ju, M. J.; Jeon, I.-Y.; Lim, K.; Kim, J. C.; Choi, H.-J.; Choi, I. T.; Eom, Y. K.; Kwon, Y. J.; Ko, J.; Lee, J.-J.; Baek, J.-B.; Kim, H. K. *Energy Environ. Sci.* **2014**, *7*, 1044.
17. Yu, D. S.; Nagelli, E.; Du, F.; Dai, L. M. *J. Phys. Chem. Lett.* **2010**, *1*, 2165.
18. Qu, L.; Liu, Y.; Baek, J.-B.; Dai, L. *ACS Nano* **2010**, *4*, 1321.
19. Ju, M. J.; Kim, J. C.; Choi, H.-J.; Choi, I. T.; Kim, S. G.; Lim, K.; Ko, J.; Lee, J.-J.; Jeon, I.-Y.; Baek, J.-B.; Kim, H. K. *ACS Nano* **2013**, *7*, 5243.
20. Jeon, I.-Y.; Choi, H.-J.; Ju, M. J.; Choi, I. T.; Lim, K.; Ko, J.; Kim, H. K.; Kim, J. C.; Lee, J.-J.; Shin, D.; Jung, S.-M.; Seo, J.-M.; Kim, M.-J.; Park, N.; Dai, L.; Baek, J.-B. *Sci. Rep.* **2013**, *3*, 2260.
21. Xue, Y.; Liu, J.; Chen, H.; Wang, R.; Li, D.; Qu, J.; Dai, L. *Angew. Chem. Int. Ed.* **2012**, *51*, 12124.
22. Fang, H.; Yu, C.; Ma, T.; Qiu, J. *Chem. Commun.* **2014**, *50*, 3328.
23. Choucair, M.; Thordarson, P.; Stride, J. A. *Nat. Nanotechnol.* **2009**, *4*, 30.
24. Lin, T.; Huang, F.; Liang, J.; Wang, Y. *Energy Environ. Sci.* **2011**, *4*, 862.
25. Lu, X.; Wu, J.; Lin, T.; Wan, D.; Huang, F.; Xie, X.; Jiang, M. *J. Mater. Chem.* **2011**, *21*, 10685.
26. Jung, S.-M.; Lee, E. K.; Choi, M.; Shin, D.; Jeon, I.-Y.; Seo, J.-M.; Jeong, H. Y.; Park, N.; Oh, J. H.; Baek, J.-B. *Angew. Chem. Int. Ed.* **2014**, *53*, 2398.

27. Bae, S.; Kim, H.; Lee, Y.; Xu, X.; Park, J.-S.; Zheng, Y.; Balakrishnan, J.; Lei, T.; Ri Kim, H.; Song, Y. I.; Kim, Y.-J.; Kim, K. S.; Ozyilmaz, B.; Ahn, J.-H.; Hong, B. H.; Iijima, S. *Nat. Nanotechnol.* **2010**, *5*, 574.
28. Lim, K.; Ju, M. J.; Na, J.; Choi, H.; Song, M. Y.; Kim, B.; Song, K.; Yu, J.-S.; Kim, E.; Ko, J. *Chem. Eur. J.* **2013**, *19*, 9442.
29. Song, B. J.; Song, H. M.; Choi, I. T.; Kim, S. K.; Seo, K. D.; Kang, M. S.; Lee, M. J.; Cho, D. W.; Ju, M. J.; Kim, H. K. *Chem. Eur. J.* **2011**, *17*, 11115.
30. Kang, M. S.; Kang, S. H.; Kim, S. G.; Choi, I. T.; Ryu, J. H.; Ju, M. J.; Cho, D.; Lee, J. Y.; Kim, H. K. *Chem. Commun.* **2012**, *48*, 9349.
31. Kang, S. H.; Choi, I. T.; Kang, M. S.; Eom, Y. K.; Ju, M. J.; Hong, J. Y.; Kang, H. S.; Kim, H. K. *J. Mater. Chem. A* **2013**, *1*, 3977.
32. Choi, I. T.; Ju, M. J.; Kang, S. H.; Kang, M. S.; You, B. S.; Hong, J. Y.; Eom, Y. K.; Song, S. H.; Kim, H. K. *J. Mater. Chem. A* **2013**, *1*, 9114.
33. Ahmad, S.; Guillen, E.; Kavan, L.; Gratzel, M.; Nazeeruddin, M. K. *Energy Environ. Sci.* **2013**, *6*, 3439.
34. Hauch, A.; Georg, A. *Electrochim. Acta* **2001**, *46*, 3457.
35. Roy-Mayhew, J. D.; Bozym, D. J.; Punckt, C.; Aksay, I. A. *ACS Nano* **2010**, *4*, 6203.
36. Tsao, H. N.; Comte, P.; Yi, C.; Grätzel, M. *ChemPhysChem* **2012**, *13*, 2976.
37. Kavan, L.; Yum, J.-H.; Grätzel, M. *Nano Lett.* **2011**, *11*, 5501.
38. Ju, M. J.; Jeon, I.-Y.; Kim, J. C.; Lim, K.; Choi, H.-J.; Jung, S.-M.; Choi, I. T.; Eom, Y. K.; Kwon, Y. J.; Ko, J.; Lee, J.-J.; Kim, H. K.; Baek, J.-B. *Adv. Mater.* **2014**, *26*, 3055.

Chapter IV. Graphitic Carbon Sheets with Random Hole-defects from *in situ* Dehydration and Thermal Reaction

4.1 Abstract

A new synthesis method was prepared for graphitic carbon sheets having microporosity. Graphitic carbon sheets (GCSs) show sheet-like morphologies and GCS-1 has well-ordered graphitic carbon structure. The random hole-defects give rise to the microporosity. Additionally, depending on the precursor, BET surface was determined. The highest BET surface area (GCS-2) is calculated to be 917 $m^2\ g^{-1}$ at 77 K at 1 bar from nitrogen adsorption and desorption isotherm. Above all, GCS-1 shows paramagnetic behavior under 10 K caused by defects, increasing edge structures.

4.2 Introduction

Carbon materials are familiar with our life, which was composed of common carbon network structure with long history, due to broad practical use for adsorbents,[1] catalyst supports,[2] membranes,[3] electrochemical electrodes,[4] etc.[5,6] Above all, carbon is major skeleton but how they are connected determines their physical and chemical properties, as including carbon allotropes, which various dimension from 0-dimension to 3-dimension; fullerene, carbon nanotube, graphene, graphite and diamond. Among various carbon materials, porous graphitic carbon materials have spotlighted because of guaranteed their stability and having a potential to apply wide range applications.[7] Compare to inorganic porous materials, including zeolites,[8] metal-organic frameworks,[9] carbon porous material has big advantages such as lightness,[10] high thermal and chemical stability,[11] easy production and low poisoning.[12]

Conventional carbon materials, including activated carbon and carbon molecular sieves, are pyrolyzed or chemically/physically activated from organic precursors, for example, natural carbon sources; coal, wood, fruit shell or polymers at elevated temperature.[13] In high-temperature (over 1000 °C), graphitic carbon materials such as highly oriented pyrolytic graphite, are prepared by pyrolysis with well-ordered carbon atom arrangement.[5] Among synthesis methods, dehydration reaction, included condensation reaction, is the powerful and general approach.[14] For example, the reaction happens between carbohydrates (e.g. sucrose) and concentrated sulfuric acid, so called charring reaction,[15] which spontaneously reacted together with heat by hydrolysis and exothermic even at room temperature. On hydrolysis, it yields the two monosaccharides, glucose and fructose, and produces a complex carbonaceous solid residue on dehydration.[15]

Among various application fields, pure carbon materials have potentials to apply a magnet. Carbon based magnet is promising caused by some advantages: to control the magnetic intensity precisely, light and flexible, and to have a chance to design new type of devices. Especially, graphene carried a potential to have a spin generator although carbon atom has no *d*- and *f*-electron.[16] Above all, the magnetic order

of *s-p* electron magnetism is predicted to be stable at high temperature.[17] However, there is an obstacle to exploiting the non-metallic organic magnets because the organic ferromagnetism has realized at low temperature (near ~few Kelvin),[18] and it is elusive to have high Qurie temperature near room temperature.[19] Theoretically, the graphite having point defects are magnetic calculated by spin-polarized density functional theory (DFT)[16] and it alternating sp^2 and sp^3 carbon bond originated the ferromagnetism.[20]

Magnetic moments in graphitic carbon materials can be introduced trustworthy by functionalization, irradiation or making defects. As known graphene and graphite are diamagnetic, there are approaches such as absorbed hydrogenation atom onto graphene,[21] defects[22] or topological structure of graphene,[19] nitrogen-doped graphene.[23] In addition to the graphite or graphene zigzag edges[24] and the negatively curved graphitic surface[25] showed ferromagnetism.

Herein, inspired the dehydration reaction and thermal reaction, and we exploited phosphorous pentoxide (P_2O_5) for dehydration of rigid carbon monomer with which is taking advantages with powerful dehydration, easy work-up process. As the results, well-ordered graphitic structures as a 2D material with random defects were prepared with uniform microporosity.

4.3 Materials and Instrumentation

1,3,5-triacetylbenzene (**1**, 98% purity) was purchased from TCI and 1,4-diacetylbenzene (99% purity) were purchased form Sigma Aldrich. 4,4'-diaceylbiphenyl (**3**, 98% purity) was purchased form Alfa Aesar. All other solvents were supplied by Aldrich Chemical Inc., unless otherwise specified.

Differential scanning calorimetry (DSC) was carried out with DSC Q200 (TA instrument, USA) at a ramping rate of 10 °C min^{-1}. Themogravimetric analysis (TGA) was conducted on a DSC Q600 (TA Instrument, USA) at a ramping rate of 10 °C min^{-1} under nitrogen and air atmosphere. The field emission scanning electron microscopy (FE-SEM) was performed on Nanonova 230 (FEI, USA) with operating at an accelerating voltage of 10 kV. Electron diffraction (ED) and high-resolution transmission electron microscopy (HR-TEM) images of GCS-1 were taken using FEI Titan G2 60-300 equipped with an imaging-side spherical aberration (Cs) corrector operating at an accelerating voltage of 80 kV. Elemental analysis (EA) was conducted with Flash 2000 (Thermo Scientific, Netherlands). X-ray photoelectron spectroscopy (XPS) spectra were recorded on a Thermo Fisher K-alpha XPS spectrometer. Solid-state ^{13}C NMR spectra were recorded on a FT-NMR 600 MHz VNMRS 600 (Agilent, USA) spectrometer. X-Ray diffraction (XRD) powder patterns were recorded with a D/MAX 2500V/PC (Rigaku, Japan) with Cu–Kα radiation (40 kV, 100 mA, λ = 1.5418 Å). Fourier transform infrared (FT-IR) spectra were performed on Spectrum 100 (Perkin-Elmer, USA) with KBr disks pellet. The nitrogen (N_2) and hydrogen (H_2) gas adsorption-desorption isotherms obtained at 77 K, using the Brunauer-Emmett-Teller (BET) method on BELSORP-max (BEL Japan, Inc., Japan). As the pretreatment, samples were degassed at 150 °C for 12 h under vacuum. The magnetic properties of the GCSs were

characterized using a Quantum Design SQUID-VSM. Electron Spin Resonance (ESR) spectra were measured by JES-FA100 (JEOL) Spectrometer (9.5 GHz) with a field modulation frequency of 100 KHz, using microware power of 10 mW and modulation amplitude of 0.4 G. ESR is a form of magnetic resonance spectroscopy used to study the electronic structure of materials with unpaired electrons.

4.4 Experimental Section

All acetyl compounds (**1**-**3**) were recrystallized from ethanol to give white needle-type crystals (1,3,5-triacetylbenzene and 1,4-diacetylbenzene) and laminar-type crystal (4,4'-diacetylbiphenyl).

Each acetyl compound (2.0 g, 1,3,5-triacetylbenzene: GCS-1; 1,4-diacetylbenzene: GCS-2; 4,4'-diacetylbiphenyl: GCS-3) and 8.0 g of phosphorus pentoxide (P_2O_5) were placed in each glass ampoule (Φ 4 x 14 cm). The ampoules were charged and discharged with argon gas five times, and then flame sealed. The ampoules and put it a box furnace with slowly increased the temperature up to 500 °C for 12 h. The ampoules were cooled down naturally and then precipitated in water for 12 h. After filtered and washed them with enough water (after checking the neutralized state), products washed again through Soxhlet with methanol and water for 3 days, respectively. After filtration, the frozen product then freeze dry at −120 °C for 2 days and collected. (Yield: 1.63 g (GCS-1); 1.81 g (GCS-2); 2.05 g (GCS-3)).

4.5 Results and Discussion

The graphitic carbon sheets (GCS-1-3) were prepared with phosphorous pentoxide (P_2O_5) and acetyl functionalized monomers described in Figure 4.1. A powerful dehydration agent, P_2O_5, has high hygroscopicity, which absorbs moisture and induced to form polyphosphoric acid which, catalyzed dehydration and carbonized the hydrocarbon. Additionally, external thermal energy applied to heat up to 500 °C for well-graphitized and made defects in the structure.

We prepared three kinds of different acetyl functionalized monomers (**1-3**) as rigid units and mixed with P_2O_5 and heat them up. The black powders were prepared with high yield (Figure 4.1). The monomers are connected as a dimer and then increased molecular weight polymer growth during the reaction. Carbonization is a complicated sequence process combined with chemical reaction and diffusion process. In other words, thermal reaction includes simultaneously complex three reactions; dehydrogenation, rearrangement and polymerization.[26] During the dehydrogenation reaction, P_2O_5 accelerated the dehydrogenation and, polymeric carbon materials are generated intermediated carbon aromatic radicals and rearranged at the atomic scale for the stable phase. Through differential scanning calorimetry (DSC) thermograms, we confirmed that P_2O_5 helps the dehydrogenation reaction by the exothermal peak shift depending on with/without P_2O_5 condition, as indicating the exothermal peaks, forming the polymeric structure, moved to directly after the melting point (Figure 4.2).

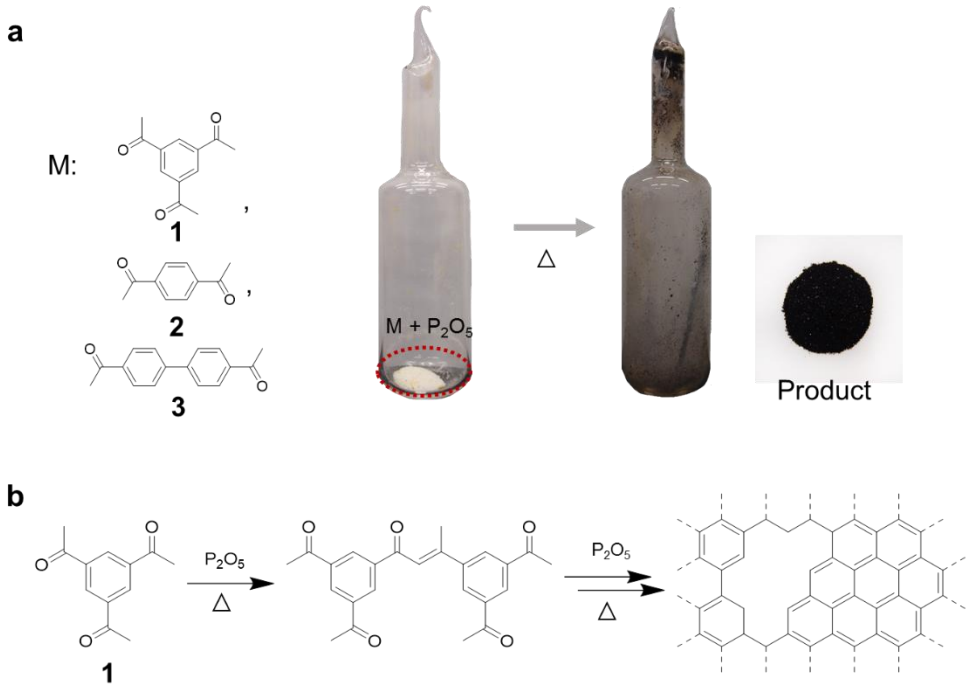

Figure 4.1. (a) Digital photographs of reaction process. Mixed monomer **1**, **2** or **3** with P_2O_5, respectively. The final product was black powder of GCSs. (b) The brief reaction scheme of GCS-1.

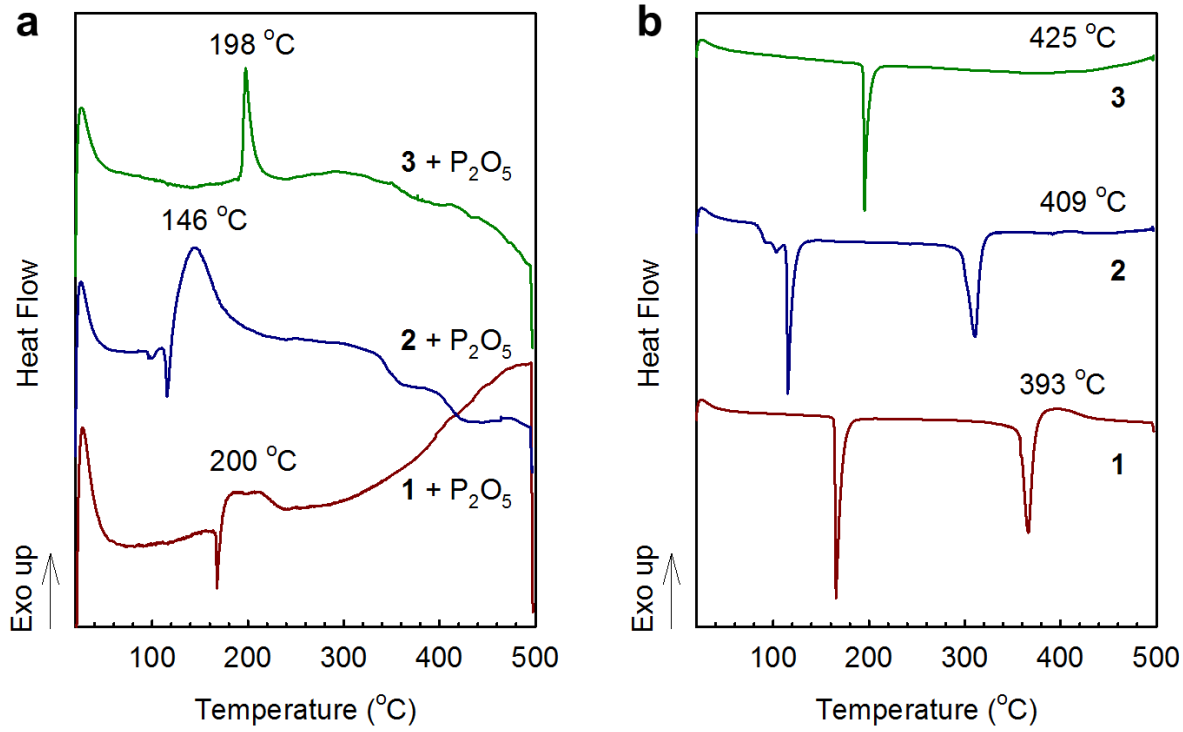

Figure 4.2. DSC thermograms from the first heating scans with ramping rate of 10 °C min^{-1} using high-pressure pan. (a) Mixed powder of acetyl monomers (**1**-**3**) with P_2O_5 with same ratio of GCSs and (b) monomers (**1**-**3**) without P_2O_5. The exothermal peaks of the existence of P_2O_5 are much lower than only monomer state. Monomers are decomposed and carbonized after phase transition to gas-state.

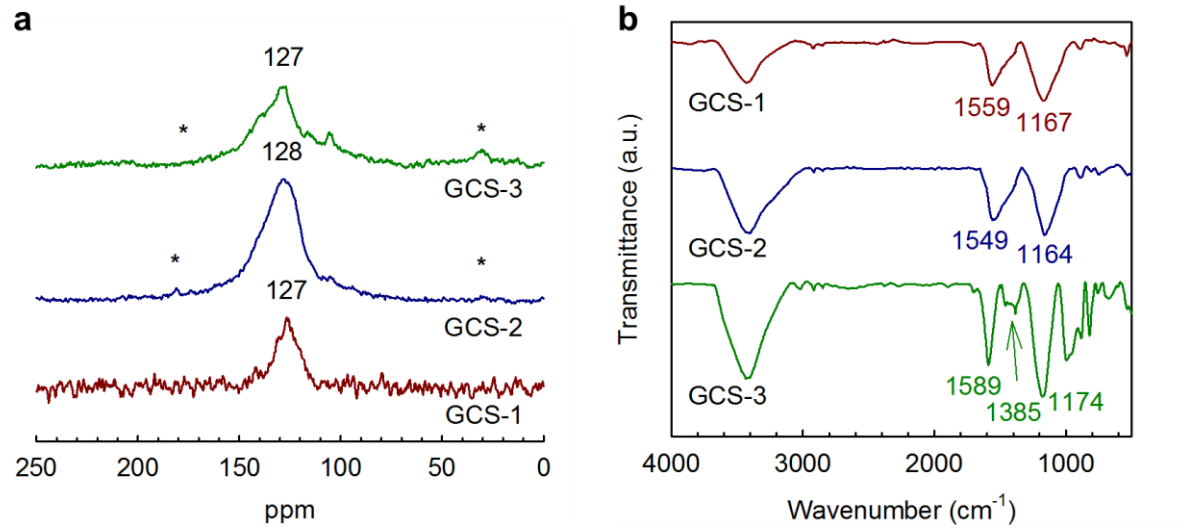

Figure 4.3. (a) Solid-state ^{13}C NMR of GCSs and (b) Fourier transform infrared (FT-IR) spectra of GCSs.

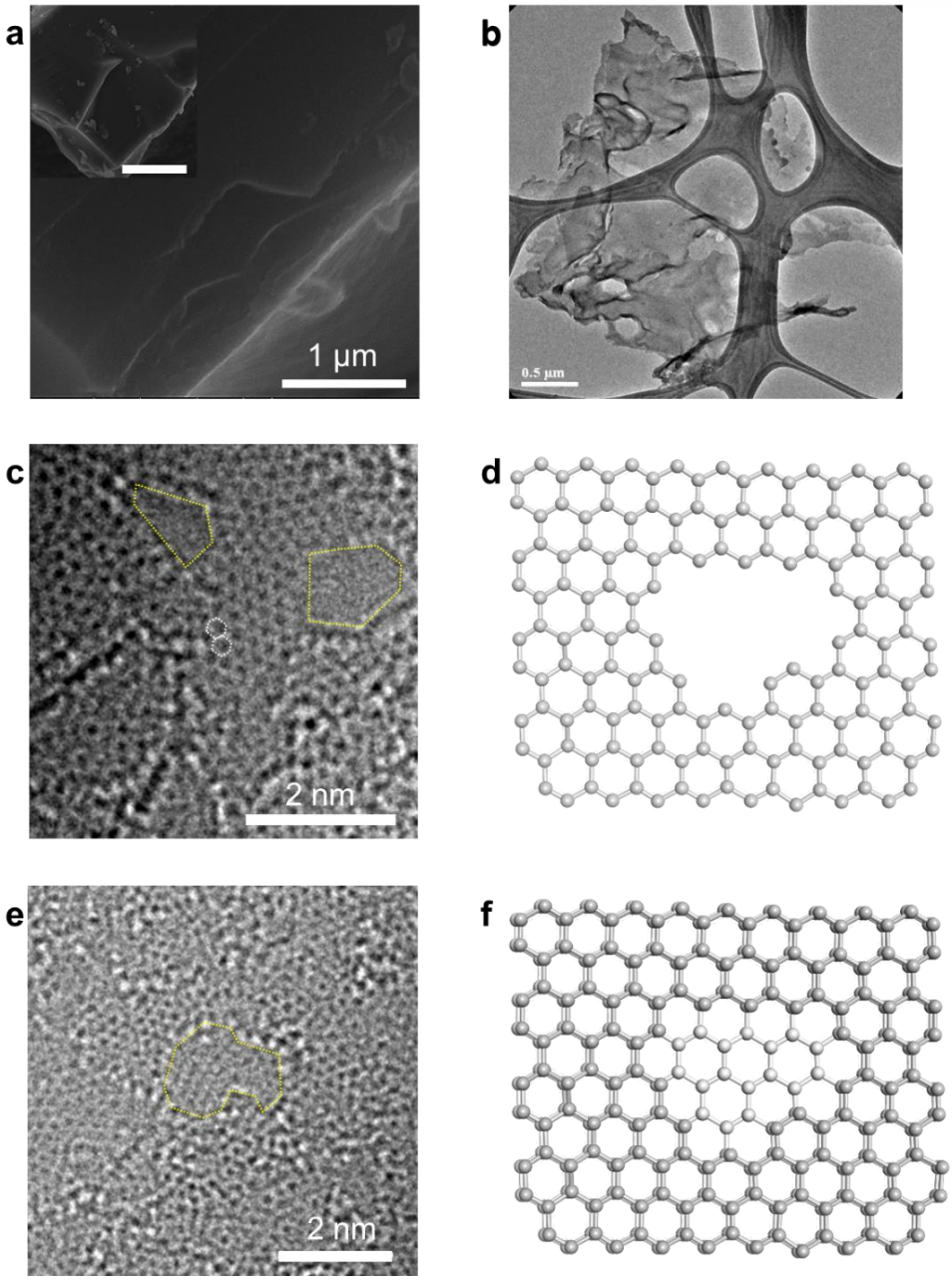

Figure 4.4. (a) SEM images of GCS-1. Inset is SEM image at low magnification and the scale bar is 10 μm. (b) TEM image of exfoliated GCS-1 at low magnification. (c and e) AR-TEM image of GCS-1; (d and f) schematic diagrams of different hole-defects in a graphitic carbon sheet. (c) monolayer of GCS and graphitic carbon aligned like graphene (white dotted line) and hole-defects marked by yellow dotted line and (d) brief structure scheme of (c) described intact hole-defect; (e) Hole-defect blocked by stacked another layer marked by yellow dotted line, and (f) brief structure of scheme of (e) described hole-defect blocked by another graphitic carbon sheet.

Generally, organic molecules start to decompose at above 400 °C, mainly through C-H bond cleavage and a subsequent loss of hydrogen.[27] Additionally, thermal rearrangement leads to more stable aromatic

building block states for graphitic structure.[26] And finally, assembled graphitic structure is formed at around 400 to 500 °C.

In order to increase the yield of GCSs, graphitic carbon material formation, it requires minimizing carbon losses in such as conversion to carbon dioxide (CO_2), converted materials to liquid or gas, etc. Therefore, we designed a closed system to minimize loss of carbon source and reacted well-mixed P_2O_5 and monomer. For the chemical environment, major carbon chemical bond is composed of aromatic carbon (127 ppm) through solid-state ^{13}C NMR (Figure 4.3a). The chemical bond environments of GCSs are measured by FT-IR, aromatic C-C vibration in 1550 cm^{-1} in common and disappeared ketone peak after the reaction (Figure 4.3b). Table 4.1 and 4.2 summarize EA and XPS results, respectively.

Table 4.1. Element analysis of GCSs

Sample	C (wt.%)	H (wt.%)	O (wt.%)	N (wt.%)	S (wt.%)	Total
GCS-1	70.97	2.65	13.93	0	0	87.55
GCS-2	69.22	2.84	16.47	0	0	88.53
GCS-3	70.89	3.26	12.12	0	0	86.27

Table 4.2. X-ray photoelectron spectra of GCSs

Sample	C (at.%)	O (at.%)	P (at.%)	Total
GCS-1	88.54	8.40	3.06	100
GCS-2	85.43	10.93	3.64	100
GCS-3	84.40	11.97	3.60	99.97

Those three samples' morphologies are similar with sheet-like shape through electron microscopy in both SEM and TEM (Figure 4.4 and Figure 4.5). Each sheet is stacked together in the powder and exfoliated sheet in the organic solvent observed through TEM (Figure 4.4a and 4.5). The monolayer of GCS-1 was observed by atomic-resolution TEM in Figure 4.4, which is well-ordered graphitic structure with randomly distributed holes of 2 nm as a kind of defects (Figure 4.4c and e). The randomly defected holes are expectably caused by pyrolysis process, nonplanar molecules from connection bond between benzene and sterically chaotic polymeric or excess amount of P_2O_5 interrupted the perfect graphitization of carbon networks.

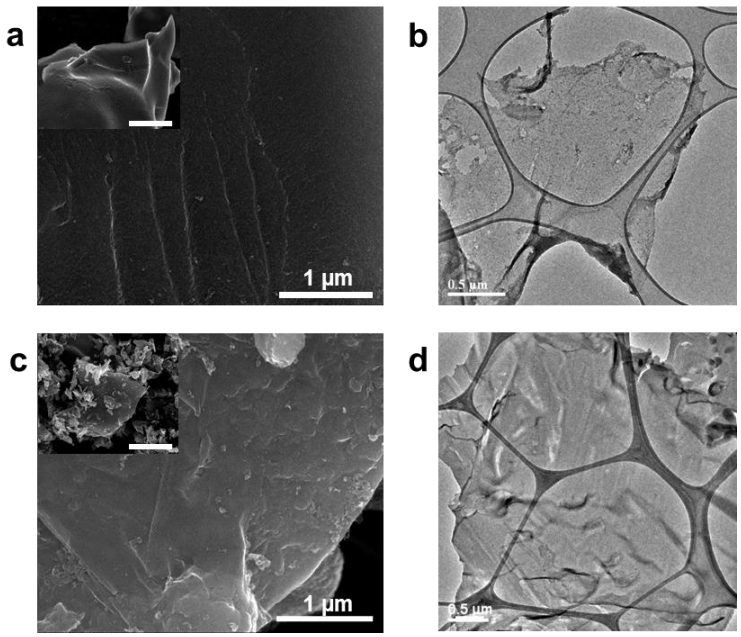

Figure 4.5. SEM images of (a) GCS-2 and (c) GCS-3. Each inset is SEM image at low magnification with 10 μm of scale bar. TEM image of exfoliated (b) GCS-2 and (d) GCS-3 at low magnification.

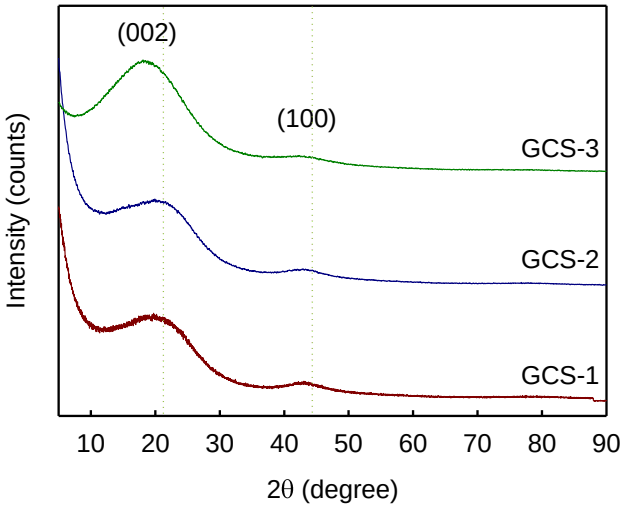

Figure 4.6. XRD patterns of GCSs.

The stacked layers of GCSs are also indirectly proved through powder X-ray diffraction (PXRD), which showed amorphous characteristic and the main peaks near 21° is (001) stacked sheets due to π-π stacking (Figure 4.6). The distance of stacked sheets is around 0.4 nm much broader than graphite, indicating that disordered carbon structure exists and indicates not regularly stacked such as graphite in hexagonal c-axis. Above all, the GCSs shows high thermal stability measured by thermogravimetry analysis (TGA) like graphite. The decomposition temperatures of GCS-1, GCS-2 and GCS-3 in 818, 810 and 777 °C with main mass loss and the residue amount was 83%, 80% and 80% at 1000 °C,

respectively and it results from well-organized graphitic structure (Figure 4.7). Although GCSs are prepared at 500 °C, the carbonized and graphitized degree of GCS is a well-oriented like other carbon materials synthesized *via* bottom-up reaction, reacted at 1000 °C.[28]

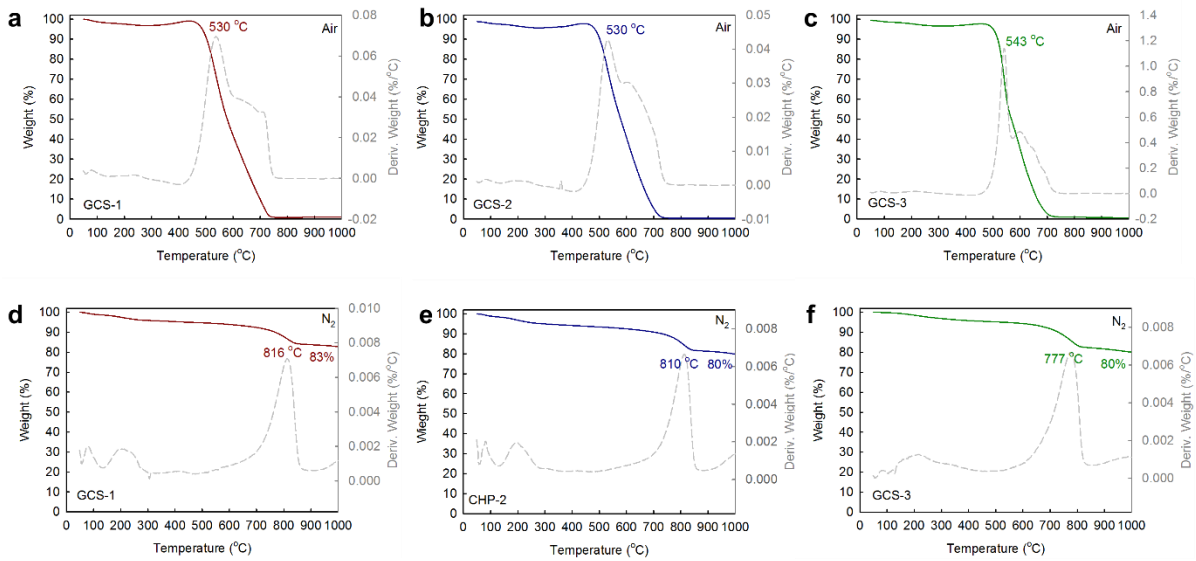

Figure 4.7. TGA thermograms estimated (a-c) under air flow and (d-f) under nitrogen flow: (a and d) GCS-1, (b and e) GCS-2 and (c and f) GCS-3.

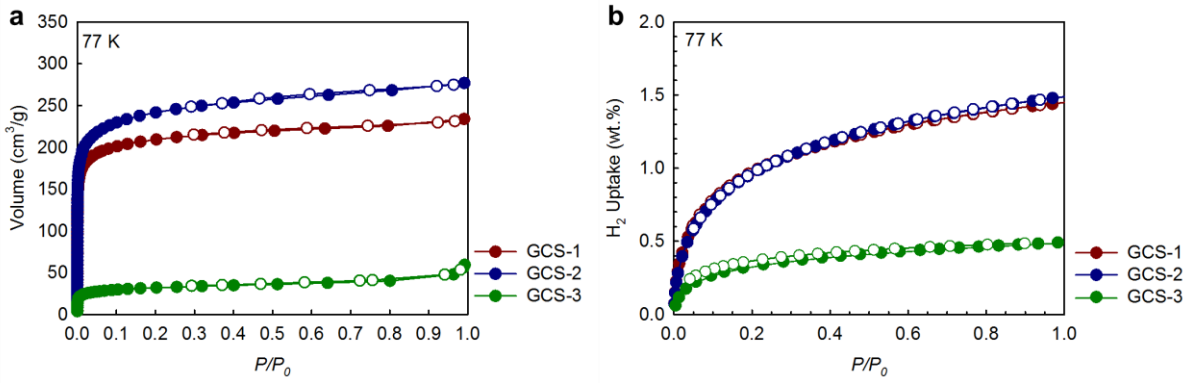

Figure 4.8. (a) N_2 adsorption and desorption isotherms and (b) H_2 adsorption and desorption isotherms at 77 K for GCSs.

Their hole defects should be affected to increase porosity in the structure. Microporous pores were determined by nitrogen adsorption/desorption isotherms with type I graph in Figure 4.8a. Microporosity in GCSs is derived from a network polymer and random arrangement suggested the micrographitic layers connected sp^3 linkage.[29] Through the AR-TEM (Figure 4.4), pores of diameter within 2 nm distributed randomly through the sheet are related to the microporosity. And some area of GCS-1 would be adopted Kanoko *et al.*, suggested model that microporosity is derived from the interstices between

micrographitic stacked may be classified into open and partially closed pores and an interstitial cage surrounded with neighboring micrograhpties.[29] BET surface areas of was calculated to 797 m^2 g^{-1} (GCS-1), 917 m^2 g^{-1} (GCS-2) and 118 m^2 g^{-1} (GCS-3). The pore volumes of GCS-1 and GCS-2 are 0.36 cm^3 g^{-1} and 0.43 cm^3 g^{-1} respectively (Figure 4.8aand Table 4.3). The calculated pore size distribution for GCSs using non-local density functional theory (NLDFT) method determined microporisity within 1.14 nm (Figure 4.9). Hydrogen uptakes of GCSs are calculated to GCS-1, GCS-2 and GCS-3 having 1.45 wt.%, 1.49 wt.% and 0.49 wt.% at 77 K (Figure 4.8b) and 1 bar.

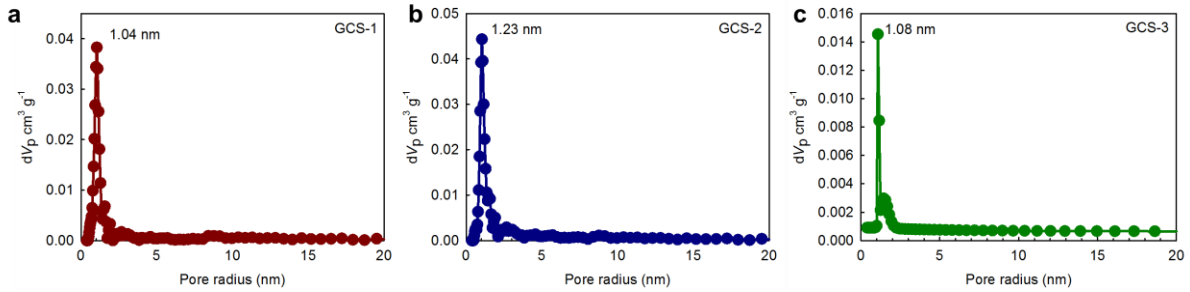

Figure 4.9. Pore size distributions of GCSs calculated from NLDFT method. (a) GCS-1, (b) GCS-2 and (c) GCS-3.

Table 4.3. The surface areas of GCSs calculated from N_2 adsorption and desorption isotherms

Sample	Specific Surface Area (m^2 g^{-1})	Pore Volume (mL g^{-1})	Pore Size (nm)
GCS-1	797.42	0.36	1.81
GCS-2	917.08	0.43	1.87
GCS-3	118.28	0.09	2.98

Table 4.4. ICP-MS data of GCSs

(Unit: ppm)

Sample	Mn	Co	Ni	Fe	Total
GCS-1	0.4090	N.D.	0.1960	0.0872	0.6922
GCS-2	0.4080	N.D.	0.1200	0.0725	0.6005
GCS-3	0.2400	N.D.	0.1000	0.00396	0.34396

*N.D.: Not detectable

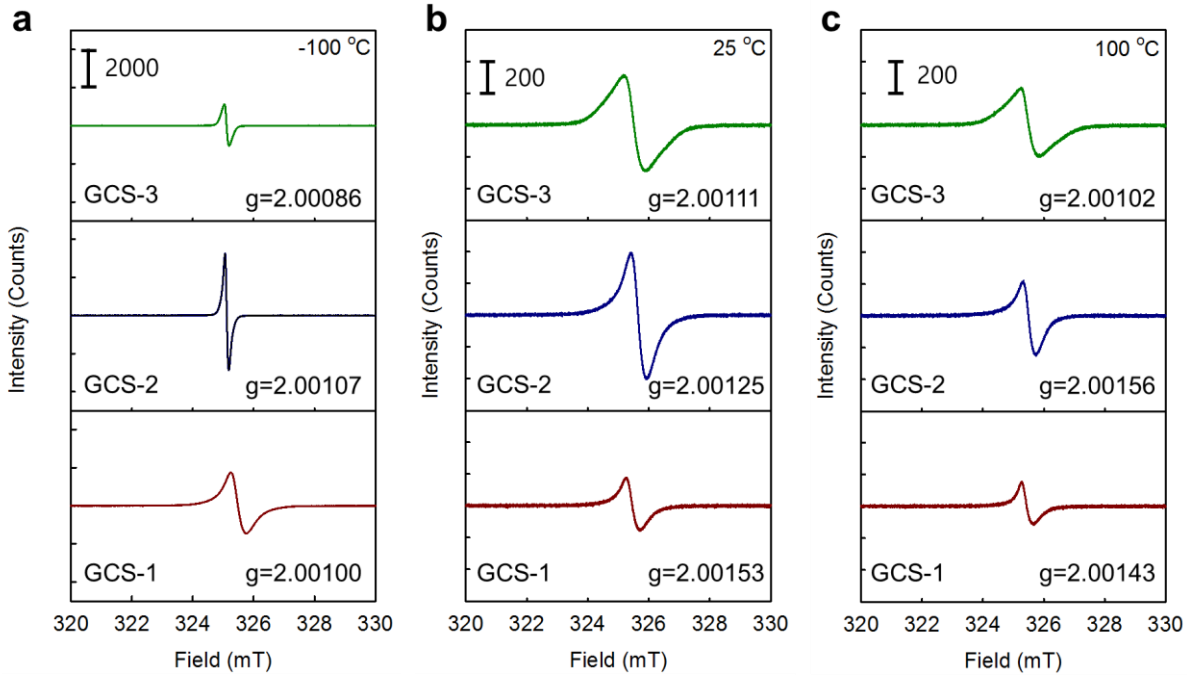

Figure 4.10. Solid ESR spectra of GCSs under ambient conditions showing isotropic singlet measured at (a) −100 °C, (b) 25 °C and (c) 100 °C.

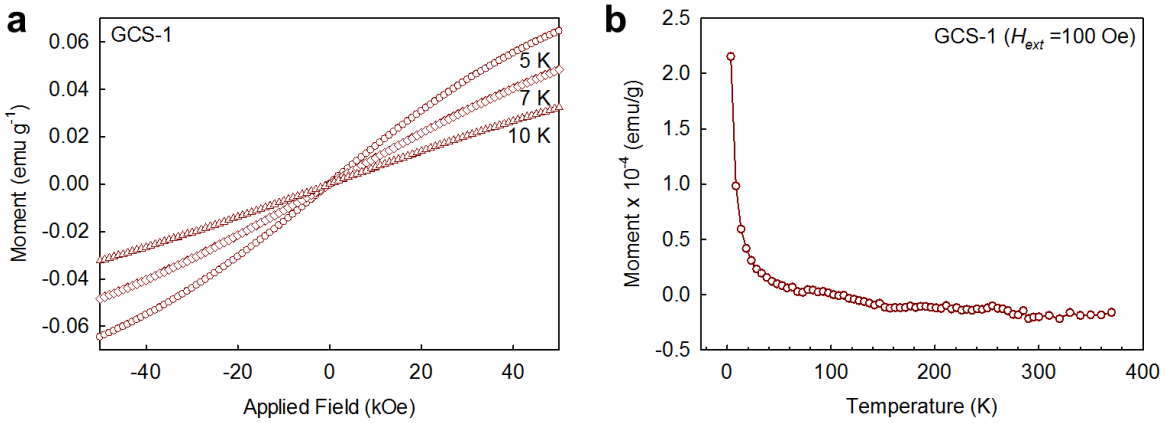

Figure 4.11. (a) Magnetic hysteresis loops of GCS-1 measured at 5, 7 and 10 K and (b) temperature evolution of the mass magnetic susceptibility of GCS-1.

The impurities even trace of metal contamination are a crucial factor to measure magnetic behavior. The controversial topic about contamination in metal-free magnetism field has given a rise. That's the reason that we confirmed the impurities amount through inductive coupled plasma mass spectrometry (ICP-MS). All samples have impurities (Mn, Fe, Co and Ni) less than 1 ppm (Table 4.3). Therefore, the total content of metallic impurities, indicating the unexpected magnetic effects, was below 1 elemental ppm. Additionally, before measuring the magnetic properties, we confirmed whether the unpaired electron exists in GCSs through the electron spin resonance spectra. In Figure 4.10, the GCS-1, GCS-2

and GCS-3 similarly have the unpaired electron with 2.001 of g-factors at −100, 25 and 100 °C, respectively.

Isothermal magnetization curves described, which were measured at 5, 7 and 10 K in the field range of −50 kOe < H < 50 kOe for GCS-1 in Figure 4.11. GCS-1 shows paramagnetic behavior by applied magnetic field *H* in low temperature, whose magnetic behavior followed Qurie-Weiss law at low temperature. Graphite and graphene are known to be strong diamagnetic.[30] Graphene, similar structure like GCS-1 having aligned graphitic carbon, is a diamagnet, and graphene multilayers is diamagnet, too because existence of the linear-dispersion at zero Fermi energy.[31]

The origin of unpaired electron, spin, of GCS-1 is derived from the magnetic ordering related to the mixture carbon atoms with sp^2 and sp^3 bond.[32] Those results are reinforced by theoretical calculations, the important role of defect-induced quasilocalizatied states.[33,34] Combination of defects within 2 nm of diameter and the zigzag edges from the defects broke the carbon hexagonal lattice and resulted in paramagnetic behavior. However, the long-range magnetic order mechanism is unclear but the exertions have been continued to clarify until now with experiments and proposed theoretical calculations.[17] Edge-inherited magnetism as an essentially 1D quantum phenomenon predicts a spin-gapped ground state with an antiferromagnetic inter-edge superexchange interaction.[17]

4.6 Conclusions

Graphitic carbon sheets were prepared *via in situ* dehydration and thermal reaction using dehydrating agent P_2O_5. GCSs showed carbon arrangement like graphene, having good graphitic structure and random hole-defects within the 2nm of diameter. The porosity of GCSs is from the defected structure and it matched with the microporosity. Aligned hexagonal lattice with random defects affects to modify magnetic state from diamagnetism to paramagnetism. This study is ongoing now, and further studies would be needed to determine the phenomena.

4.7 References

1. Namasivayam, C.; Kavitha, D. *Dyes Pigm.* **2002**, *54*, 47.
2. Zhao, X. L.; Li, F.; Wang, R. N.; Seo, J. M.; Choi, H. J.; Jung, S. M.; Mahmood, J.; Jeon, I. Y.; Baek, J. B. *Adv. Funct. Mater.* **2017**, *27*, 1605717.
3. Lee, B.; Baek, Y.; Lee, M.; Jeong, D. H.; Lee, H. H.; Yoon, J.; Kim, Y. H. *Nat. Commun.* **2015**, *6*, 7109.
4. Zhu, Y.; Murali, S.; Stoller, M. D.; Ganesh, K. J.; Cai, W.; Ferreira, P. J.; Pirkle, A.; Wallace, R. M.; Cychosz, K. A.; Thommes, M.; Su, D.; Stach, E. A.; Ruoff, R. S. *Science* **2011**, *332*, 1537.
5. Krüger, A. *Carbon Materials and Nanotechnology*; Wiley, 2010.
6. White, R. J.; Budarin, V.; Luque, R.; Clark, J. H.; Macquarrie, D. J. *Chem. Soc. Rev.* **2009**, *38*, 3401.
7. Xia, Y. D.; Yang, Z. X.; Zhu, Y. Q. *J. Mat. Chem. A* **2013**, *1*, 9365.
8. Roth, W. J.; Nachtigall, P.; Morris, R. E.; Wheatley, P. S.; Seymour, V. R.; Ashbrook, S. E.; Chlubna, P.; Grajciar, L.; Polozij, M.; Zukal, A.; Shvets, O.; Cejka, J. *Nat. Chem.* **2013**, *5*, 628.
9. Li, H.; Eddaoudi, M.; O'Keeffe, M.; Yaghi, O. M. *Nature* **1999**, *402*, 276.
10. Iizuka, H.; Fushitani, M.; Okabe, T.; Saito, K. *J. Porous Mat.* **1999**, *6*, 175.
11. Marsh, H.; Reinoso, F. R. *Activated Carbon*; Elsevier Science, 2006.
12. Jeon, I. Y.; Choi, H. J.; Choi, M.; Seo, J. M.; Jung, S. M.; Kim, M. J.; Zhang, S.; Zhang, L. P.; Xia, Z. H.; Dai, L. M.; Park, N.; Baek, J. B. *Sci. Rep.* **2013**, *3*, 1810.
13. Liang, C.; Li, Z.; Dai, S. *Angew. Chem. Int. Ed.* **2008**, *47*, 3696.
14. Pekala, R. W. *J. Mat. Sci.* **1989**, *24*, 3221.
15. Dolson, D. A.; Battino, R.; Letcher, T. M.; Pegel, K. H.; Revaprasadu, N. *J. Chem. Educ.* **1995**, *72*, 927.
16. Yazyev, O. V.; Helm, L. *Phys. Rev. B* **2007**, *75*, 125408.
17. Magda, G. Z.; Jin, X.; Hagymasi, I.; Vancso, P.; Osvath, Z.; Nemes-Incze, P.; Hwang, C.; Biro, L. P.; Tapaszto, L. *Nature* **2014**, *514*, 608.
18. Tamura, M.; Nakazawa, Y.; Shiomi, D.; Nozawa, K.; Hosokoshi, Y.; Ishikawa, M.; Takahashi, M.; Kinoshita, M. *Chem. Phys. Lett.* **1991**, *186*, 401.
19. Wang, Y.; Huang, Y.; Song, Y.; Zhang, X.; Ma, Y.; Liang, J.; Chen, Y. *Nano Lett.* **2009**, *9*, 220.
20. Ovchinnikov, A. A.; Spector, V. N. *Synth. Met.* **1988**, *27*, 615.
21. González-Herrero, H.; Gómez-Rodríguez, J. M.; Mallet, P.; Moaied, M.; Palacios, J. J.; Salgado, C.; Ugeda, M. M.; Veuillen, J.-Y.; Yndurain, F.; Brihuega, I. *Science* **2016**, *352*, 437.
22. Cervenka, J.; Katsnelson, M. I.; Flipse, C. F. J. *Nat. Phys.* **2009**, *5*, 840.
23. Blonski, P.; Tucek, J.; Sofer, Z.; Mazanek, V.; Petr, M.; Pumera, M.; Otyepka, M.; Zboril, R. *J. Am. Chem. Soc.* **2017**, *139*, 3171.

24. Yazyev, O. V.; Katsnelson, M. I. *Phys. Rev. Lett.* **2008**, *100*, 047209.
25. Park, N.; Yoon, M.; Berber, S.; Ihm, J.; Osawa, E.; Tománek, D. *Phys. Rev. Lett.* **2003**, *91*, 237204.
26. Lewis, I. C.; Singer, L. S. *Carbon* **1969**, *7*, 93.
27. Benjamin, B. M.; Raaen, V. F.; Maupin, P. H.; Brown, L. L.; Collins, C. J. *Fuel* **1978**, *57*, 269.
28. Paraknowitsch, J. P.; Thomas, A. *Macromol. Chem. Phys.* **2012**, *213*, 1132.
29. Kaneko, K.; Ishii, C.; Ruike, M.; kuwabara, H. *Carbon* **1992**, *30*, 1075.
30. Sepioni, M.; Nair, R. R.; Rablen, S.; Narayanan, J.; Tuna, F.; Winpenny, R.; Geim, A. K.; Grigorieva, I. V. *Phys. Rev. Lett.* **2010**, *105*, 207205.
31. Koshino, M.; Ando, T. *Physica E: Low-dimensional Systems and Nanostructures* **2008**, *40*, 1014.
32. Makarova, T. L.; Shelankov, A. L.; Zyrianova, A. A.; Veinger, A. I.; Tisnek, T. V.; Lähderanta, E.; Shames, A. I.; Okotrub, A. V.; Bulusheva, L. G.; Chekhova, G. N.; Pinakov, D. V.; Asanov, I. P.; Šljivančanin, Ž. *Sci. Rep.* **2015**, *5*, 13382.
33. Mizes, H. A.; Foster, J. S. *Science* **1989**, *244*, 559.
34. Pereira, V. M.; Lopes dos Santos, J. M. B.; Castro Neto, A. H. *Phys. Rev. B* **2008**, *77*, 115109.

Chapter V. Unusually Stable Triazine-based Organic Superstructure

Note: This chapter is partially and totally adapted with permission from "Unusually stable triazine-based organic superstructure", Angewandte Chemie International Edition 2016, 55(26), 7593. Copyright © 2016, WILEY-VCH Verlag.

5.1 Abstract

Since it was reported for polypeptide in 1963, solid-state reaction has been rapidly gaining popularity in organic chemistry due to its simplicity, efficiency, and selectivity compared to liquid-phase reaction. However, the direct conversion of organic single crystals into a well-defined superstructure had not yet been realized. Here, we describe the formation of superstructure by solid-state reaction of an organic single crystal. The superstructure of 5,5',5"-(1,3,5-triazine-2,4,6-triyl)triisophthalonitrile (TIPN) can be formed by stagnate cyclotrimerization of 1,3,5-tricyanobenzene (TCB) single crystals. The TIPN superstructure was confirmed by single crystal X-ray diffraction and visualized by transmission electron microscopy. The superstructure has hexagonally packed 1-dimensional (1D) channels along the crystal axis. Furthermore, the superstructure arises from interdigitated nitrile interactions in the crystal lattice, and thus has very high thermal stability.

5.2 Introduction

Merrifield introduced new chemical synthesis of polypeptide by solid-phase reaction in 1963.[1] After his contribution, solid-phase (reactions between solid-liquid or solid-gas phase reactants) and solid-state (the reaction between two solid-phase reactants) organic chemical reactions were rapidly developed, along with improvements in crystal engineering technique.[2] Solid-state reactions are simple, efficient, and highly selective compared to liquid-phase reactions, because the molecules are tightly and regularly orientated in a crystal lattice.[3] The solid-state reactions in modern chemistry involve photochemical reaction,[4,5] thermal reaction,[6] microwave method,[7] and mechanochemical reaction, including grinding.[8] In addition, Toda introduced host-guest chemistry in solid-state organic reactions towards high selectivity products.[3] Hence, understanding the crystal structure of reactants using X-ray crystallography is a fundamental step for prediction of the reactivity of reactants and the structural information of products. This is because the properties of organic solids depend not only on configuration, but also on conformation. The molecular arrangements in organic single crystals can provide clues to how molecules are packed, and allow understanding of the chemical and physical nature of the molecules. Most of the molecular ordering in organic compounds is not driven by chemical reactions, but in response to thermodynamic and statistical parameters crucial for molecular packing in a crystal lattice. Generally, the crystals of organic molecules assemble in response to noncovalent intermolecular interactions based on such as metal coordination,[9] van der Waals force,[10-12] π-π interaction,[13] and hydrogen bonding.[14,15] Furthermore, the study of superimposed crystalline structures

has been vigorously pursued, with subject areas including ordered supramolecules,[16] metal-organic frameworks (MOFs),[17,18] coordination complexes with particles and polymer,[19] and covalent organic frameworks (COFs).[20,21] However, following the principle of close packing, porous single crystals resulting from noncovalent interactions are rare because most of the molecules in the solid, pack efficiently in ways that minimize the crystal volume.[22] Even so, a few examples have been revealed by X-ray diffraction (XRD), and include such as the crystal structures of columnar pore channels[5,23] and cage pores.[22,24]

This work, our strategy was aimed at achieving a solid-state chemical reaction that would yield a well-defined interlocked superstructure. Moreover, this process had to be simple, convenient, and eco-friendly, without the use of organic solvents during synthesis. The new organic compound, 2,4,6-triphenyl-*s*-triazine has C_3 symmetry and six nitrile groups at its periphery. It is realized by a solid-state reaction of 1,3,5-tricyanobenzene single crystals in the presence of hydrochloric acid as a gaseous catalyst. The compound, 5,5',5''-(1,3,5-triazine-2,4,6-triyl)triisophthalonitrile (TIPN), has not yet been synthesized by conventional synthetic methodology, but for the first time, was created by stagnant cyclotrimerization. The TIPN-formed superstructure was resolved by single crystal XRD patterns and its cylindrical channels in the crystal architecture were visualized by transmission electron microscopy (TEM). The TIPN superstructure displayed unusually high thermal stability, due to six TIPN molecules interlocked to form a hexagonal structure, superimposed by π-π interaction.

5.3 Materials and Instrumentation

1,3,5-Tricyanobenzene (TCB, 97% purity) was purchased from Synton Chemicals GmbH (German). All other solvents were supplied by Aldrich Chemical Inc., unless otherwise specified.

Differential scanning calorimetry (DSC) was carried out with DSC Q200 (TA instrument, USA) at a ramping rate of 10 °C min^{-1}. Themogravimetric analysis (TGA) was conducted on a DSC Q600 (TA Instrument, USA) at a ramping rate of 10 °C min^{-1} under nitrogen atmosphere. The field emission scanning electron microscopy (FE-SEM) was performed on Nanonova 230 (FEI, USA) with operating at an accelerating voltage of 10 kV. Electron diffraction (ED) and high-resolution transmission electron microscopy (HR-TEM) images of TIPN 1D wires were taken using FEI Titan G2 60-300 equipped with an imaging-side spherical aberration (Cs) corrector operating at an accelerating voltage of 80 kV. Electron energy loss spectroscopy (EELS) spectra were recorded using a Gatan Imaging Filter (Quantum 965). The cross-sectional TEM samples of TIPN wires were prepared by a focused ion beam (FIB) technique (FEI Helios Nano Lab 450). Elemental analysis (EA) was conducted with Flash 2000 (Thermo Scientific, Netherlands). X-Ray diffraction (XRD) powder patterns were recorded with a D/MAZX 2500V/PC (Rigaku, Japan) with Cu–Kα radiation (40 kV, 100 mA, λ = 1.5418 Å). The sample mass was confirmed by electron ionized mass spectroscopy (EI-MS), which is 450-GC & 320-MS (Bruker) in powder state. Fourier transform infrared (FT-IR) spectra were performed on Spectrum 100

(Perkin-Elmer, USA) with KBr disks pellet. The nitrogen (N_2) and carbon dioxide (CO_2) gas adsorption-desorption isotherms obtained at 77 K and 196 K, respectively, using the Brunauer-Emmett-Teller (BET) method on BELSORP-max (BEL Japan, Inc., Japan). As the pretreatment, samples were degassed at 150 °C for 12 h under vacuum.

5.4 Experimental Section

5.4.1 Cyclotrimerization of TCB into TIPN (TCB-500HCl)

1,3,5-Tricyanobenzene (TCB) was recrystallized from 95% ethanol. TCB single crystals (250 mg) were placed in a glass ampoule (Φ 4 × 14 cm) dried in vacuum oven (0.05 mmHg) at 70 °C for overnight. After 5 cycles of charging and discharging argon gas, the ampule was charged and discharged with dry hydrogen chloride (HCl) five times. Dry HCl gas was generated by dropwise addition of conc. HCl (37%) into conc. sulphuric acid (95%). Evolved HCl gas was passed through sulphuric acid trap to completely remove any moisture prior to charging into the ampoule (**Caution**: violent HCl gas evolution occurs! Careful conc. HCl addition is required.). After charging dry HCl gas, the ampoule was sealed by flame and placed in the box furnace. The furnace was gradually heated to 250 °C with ramping rate of 0.7 °C min^{-1}, and maintained for 72 h. Then, the furnace was further heated to 500 °C for 9 h. After slowly cooling, the sample was washed with N-methyl-2-pyrrolidone (NMP). The product was collected by filtration and dried in vacuum oven (0.05 mmHg) at 70 °C for overnight. The product (TIPN, TCB-500HCl) obtained was 53.3 mg (21.3%) of brownish powder. Calcd. for $C_{27}H_9N_9$: C, 70.59%; H, 1.97%; N, 27.44% Anal. Found: C, 70.48%; H, 1.89%; N, 26.69%.

5.4.2 Cyclotrimerization of TCB-250

1,3,5-Tricyanobenzene (TCB) was recrystallized from 95% ethanol to give white needle-type crystals. TCB crystals (200 mg) were placed in an ampoule (Φ 4 x 14 cm) and dried in vacuum oven at 70 °C for overnight. The ampoule was charged and discharged with argon gas five times, and then flame sealed. The ampoule was heated to 250 °C with a ramping rate of 0.7 °C min^{-1} and kept at 250 °C for 18 h in box furnace. The work-up procedures were the same as TIPN (TCB-500HCl). The yield was too low to determine.

5.4.3 Cyclotrimerization of TCB-250HCl

Similar to TCB-250, TCB crystals (200 mg) were placed in an ampoule (Φ 4 x 14 cm) and dried in vacuum oven at 70 °C for overnight. After charging and discharging argon gas five times, dry hydrochloric acid (HCl) gas was charged and discharged five times. Dry HCl gas was generated by dropwise adding conc. HCl (37%) into 95% sulphuric acid. Evolved HCl gas was pass through sulphuric acid trap to completely remove any moisture prior to charging into the ampoule. The ampoule was heated to 250 °C with ramping rate of 0.7 °C min^{-1} and kept at 250 °C for 18 h in box furnace. The

work-up procedures were the same as TIPN (TCB-500HCl). The yield was 23.0 mg (6%) of ash brown powder.

5.4.4 Crystallographic Data Collection and Refinement of the Structure of TCB

A crystal of 1,3,5-tricyanobenzene was coated with paratone oil and the diffraction data measured at 173 K with Mo Kα radiation on an X-ray diffraction camera system using an imaging plate equipped with a graphite crystal incident beam monochromator. The RapidAuto software[25] was used for data collection and data processing. Structure was solved by direct method and refined by full-matrix least-squares calculation with the SHELXTL software package.[26]

TCB was observed as an asymmetric unit. All non-hydrogen atoms were refined anisotropically; the hydrogen atoms were assigned isotropic displacement coefficients U(H) = 1.2U (C) and their coordinates were allowed to ride on their respective atoms. Final least-squares refinement of the structure converged at a final $R1 = 0.0332$ and $wR2 = 0.0697$ for 1382 reflections with $I > 2\sigma(I)$; $R1 = 0.0547$ and $wR2 = 0.794$ for all 1803 reflections. The largest difference peak and hole were 0.137 and −0.163 e·Å^{-3}, respectively.

A summary of the crystal and some crystallography data is given in Supplementary Table 1. CCDC-1441873 contains the supplementary crystallographic data for this paper. The data can be obtained free of charge at www.ccdc.cam.ac.uk/conts/retrieving.html or from the Cambridge Crystallographic Data Centre, 12, Union Road, Cambridge CB2 1EZ, UK.

5.4.5 Crystallographic Data Collection and Refinement of the Structure of TIPN

A crystal of 5,5',5''-(1,3,5-triazine-2,4,6-triyl)triisophthalonitrile (TIPN) was coated with paratone-*N* oil and the diffraction data measured at 100 K with synchrotron radiation ($\lambda = 0.65000$ Å) on a ADSC Quantum-210 detector at 2D SMC with a silicon (111) double crystal monochromator (DCM) at the Pohang Accelerator Laboratory, Korea. The ADSC Q210 ADX program[27] was used for data collection (detector distance is 63 mm, omega scan; $\Delta\omega = 1°$, exposure time was 12 sec per frame) and HKL3000sm (Ver. 703r)[28] was used for cell refinement, reduction and absorption correction. Structure was solved by direct method and refined by full-matrix least-squares calculation with the SHELX software package.[29]

A TIPN and a water site of ~ 0.17 occupancy were observed as an asymmetric unit. All non-hydrogen atoms were refined anisotropically; the hydrogen atoms were assigned isotropic displacement coefficients U(H) = 1.2U (C) and their coordinates were allowed to ride on their respective atoms except for the hydrogen atoms of the water molecule. Refinement of the structure converged at a final $R1 = 0.0707$ and $wR2 = 0.1918$ for 4232 reflections with $I > 2\sigma(I)$; $R1 = 0.1233$ and $wR2 = 0.2273$ for all 7347 reflections. The largest difference peak and hole were 0.369 and −0.350 e·Å^{-3}, respectively.

A summary of the crystal and some crystallography data is given in Supplementary Table 2. CCDC-

1444191 contains the supplementary crystallographic data for this paper. The data can be obtained free of charge at www.ccdc.cam.ac.uk/conts/retrieving.html or from the Cambridge Crystallographic Data Centre, 12, Union Road, Cambridge CB2 1EZ, UK.

5.4.6 DFT Calculation

To evaluate the formation energy, we proceeded density functional theory (DFT) calculation with Perdew-Burke-Ernzerhof[30] (PBE) type generalized gradient approximation (GGA) exchange correlation using Vienna Ab initio simulation package (VASP).[31-34] To describe van der Waals type inter-molecular interaction, we used DFT+D2 potential.[35] Energy cut off was set as 400 eV for the plane wave basis set and projector argumented-wave (PAW) type pseudopotential method was employed. For the molecular system, there was at least 10 Å vacuum space in periodic boundary condition. For the TIPN crystalline 3-D structure and CTF-0 2-D structure, 2×2×4 and 3×3×1 k-points were sampled following the Monkhorst-pack in the Brillouin zone, respectively.

5.4.7 TEM Image Simulation

Based on crystal structure data obtained from XRD analysis, TEM simulations of ED patterns and HR-TEM images were carried out using MacTempas software. The simulation in Figure 5.20 was done in an acceleration voltage of 80 kV with a defocus of +250 nm, a thickness of 80 nm and a constant of third order spherical aberration of −27 μm. The simulation in Figure 5.21 was performed in an acceleration voltage of 80 kV with a defocus of −100 nm, a thickness of 60 nm and a constant of third order spherical aberration of −27 μm.

5.5 Result and Discussion

Via the synthetic procedure described in Figure 5.1a, a trifunctional monomer (M3) of 1,3,5-tricyanobenzene (TCB, structure 1, Figure 5.1a) was annealed in a sealed glass ampoule at 250 °C in the presence of hydrochloric acid as a gaseous catalyst for solid-state reaction. Typically, TCB polymerizes into a poly(*s*-triazine) network (CTF-0, structure 3, Figure 5.1a) *via* spontaneous cyclization of three nitrile (–C≡N) groups.[36,37] However, the reaction stagnates after a single cyclotrimerization, producing TCB trimer, 5,5',5"-(1,3,5-triazine-2,4,6-triyl)triisophthalonitrile (TIPN, structure 2, Figure 5.1a).

For the above solid-state reaction, TCB was recrystallized from ethanol to grow rod-shaped monoclinic crystals by rich π-π interaction (Figure 5.2a) and its structure was revealed by single-crystal XRD (Figures 5.3, 5.4 and Table 5.1). On the basis of crystallographic information, we recognized that nitrile groups in TCB crystals interacted with three adjacent molecules having average distance of 3.88 Å (each distance between carbon and nitrogen: 3.56 Å; 3.28 Å; 4.31 Å, Figure 5.3b). The distance among nitrile groups is within the range of cyclotrimerization. However, high energy (high pressure and temperature above melting) was required to drive the formation of *s*-triazine rings.[38] On the other hand, the solid-state reaction must occur below the melting temperature of reactants.

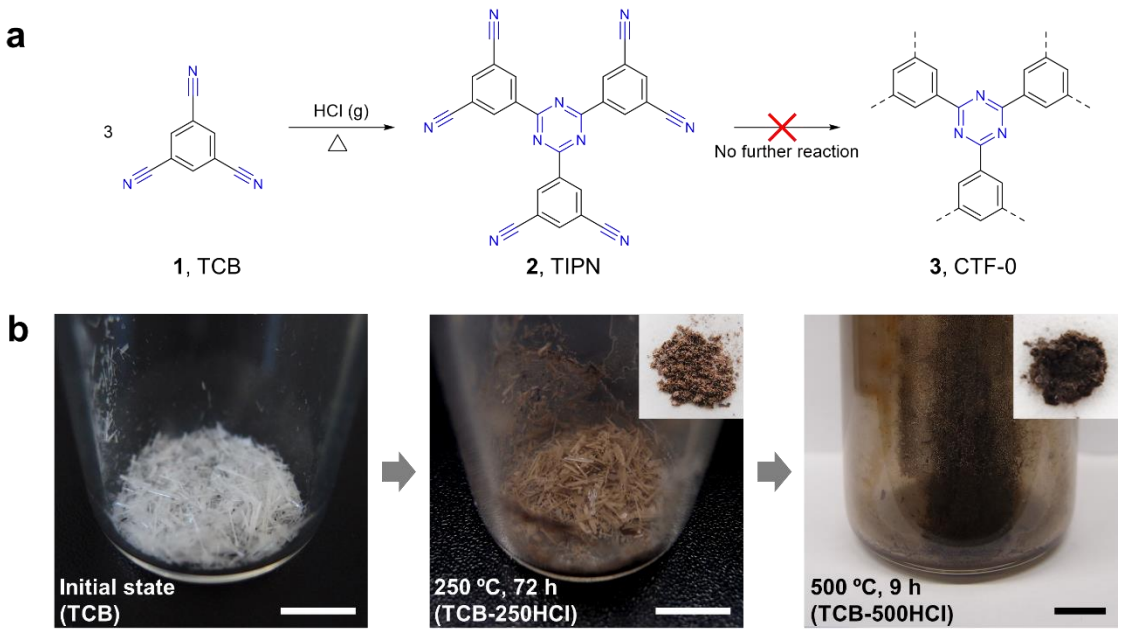

Figure 5.1. (a) Schematic representation of TIPN formation after a single cyclotrimerization of TCB single crystals; (b) Digital photographs of TCB at different temperature and time showing the progress of the solid-state reaction. The color change of the sample, from sugar white to ash brown, suggested that the solid-state reaction occurred at 250 °C (below TCB melting temperature) in the presence of dry gaseous HCl. After further heat-treatment at 500 °C, the color of the sample changed to dark brown. The scale bars indicate 1 cm. The inset images are the final products on weighing paper after work-up.

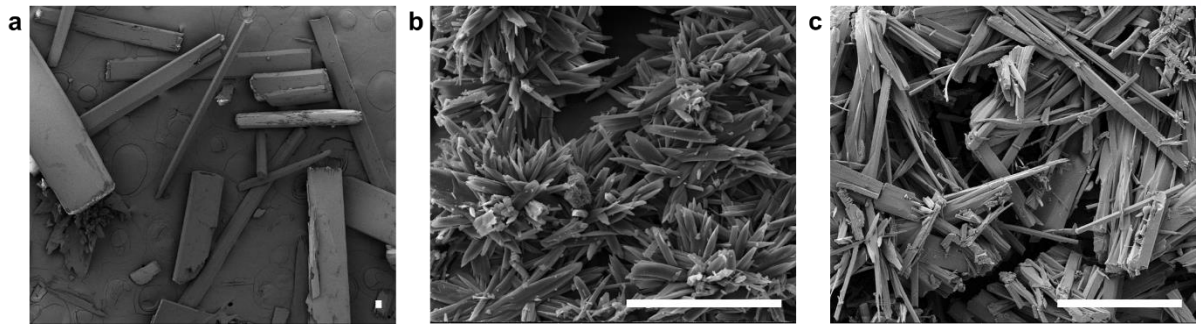

Figure 5.2. SEM images: (a) TCB single crystals, (b) TCB-250HCl (250 °C for 72 h) and (c) TCB-500HCl, TIPN (500 °C for 9 h after 250 °C for 72 h). The scale bars indicate 50 μm.

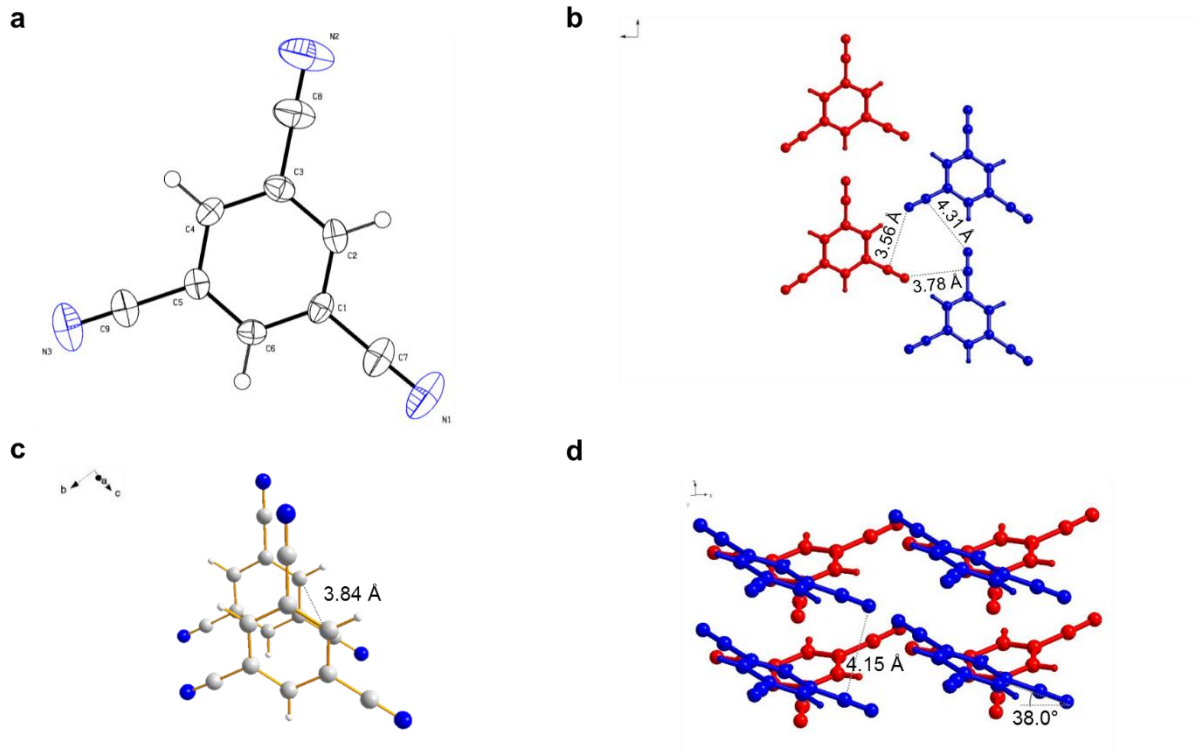

Figure 5.3. (a) ORTEP drawing of TCB, monomer **1**. (b) Ball-and-stick representation of TCB in crystal. (c) and (d) the distance of π-π distance is 3.84 Å in perpendicular direction (color code: grey = carbon; blue = nitrogen; white = hydrogen).

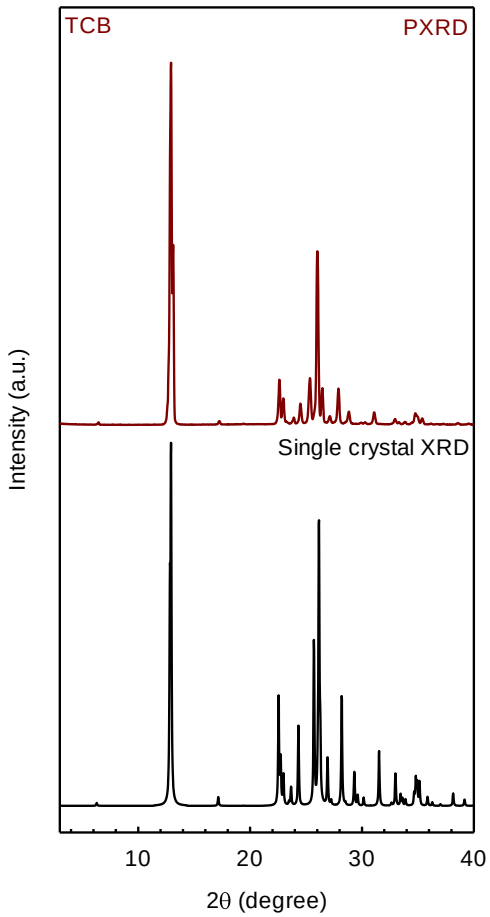

Figure 5.4. PXRD pattern of TCB (dark red) and single crystal XRD pattern of TCB (black).

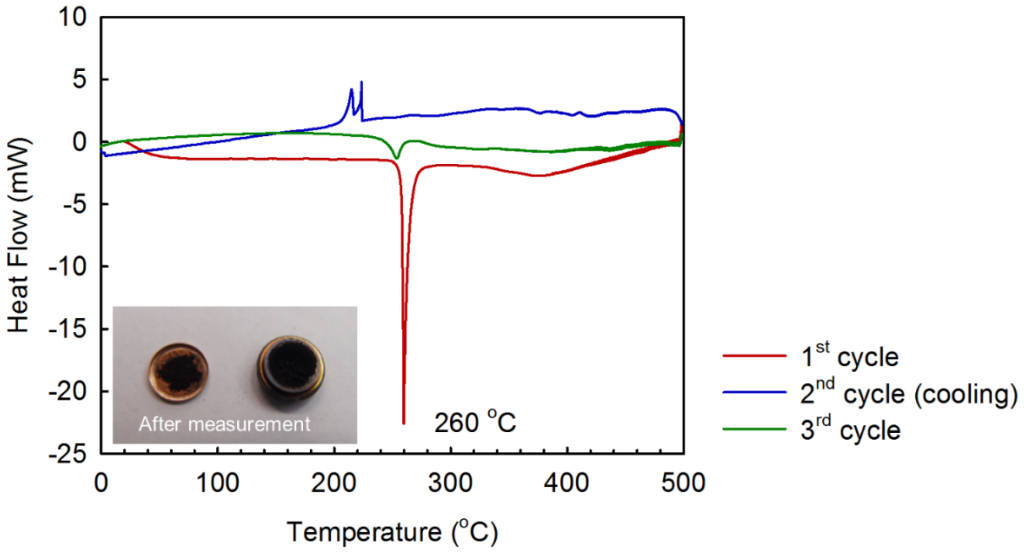

Figure 5.5. Differential scanning calorimetry (DSC) curves of TCB with ramping rate of 10 °C min^{-1} under nitrogen gas flow. Inset is a photograph after DSC measurement.

Table 5.1. Crystallographic data for TCB

Identification	TCB
Empirical formula	$C_9H_3N_3$
Formula weight	153.14
Temperature	173(2) K
Wavelength	0.71073 Å
Crystal system	Monoclinic
Space group	$P2_1$
Unit cell dimensions	a = 3.8397(8) Å, α = 90° b = 7.7446(15) Å, β = 93.79(3)° c = 13.585(3) Å, γ = 90°
Volume	403.10(14) $Å^3$
Z	2
Density (calculated)	1.262 Mg m^{-3}
Absorption coefficient	0.081 mm^{-1}
F(000)	156
Crystal size	0.47 x 0.29 x 0.09 mm^3
Theta range for data collection	3.01 to 27.44°
Index ranges	-4<=h<=4, -10<=k<=10, -17<=l<=17
Reflections collected	3881
Independent reflections	1803 [R(int) = 0.0263]
Completeness to theta = 22.955°	99.9%
Absorption correction	Semi-empirical from equivalents
Max. and min. transmission	0.9927 and 0.9627
Refinement method	Full-matrix least-squares on F^2
Data / restraints / parameters	1803 / 1 / 110
Goodness-of-fit on F^2	1.086
Final R indices [I>2sigma(I)]	R1 = 0.0332, wR2 = 0.0697
R indices (all data)	R1 = 0.0547, wR2 = 0.0794
Largest diff. peak and hole	0.137 and –0.163 e·$Å^{-3}$

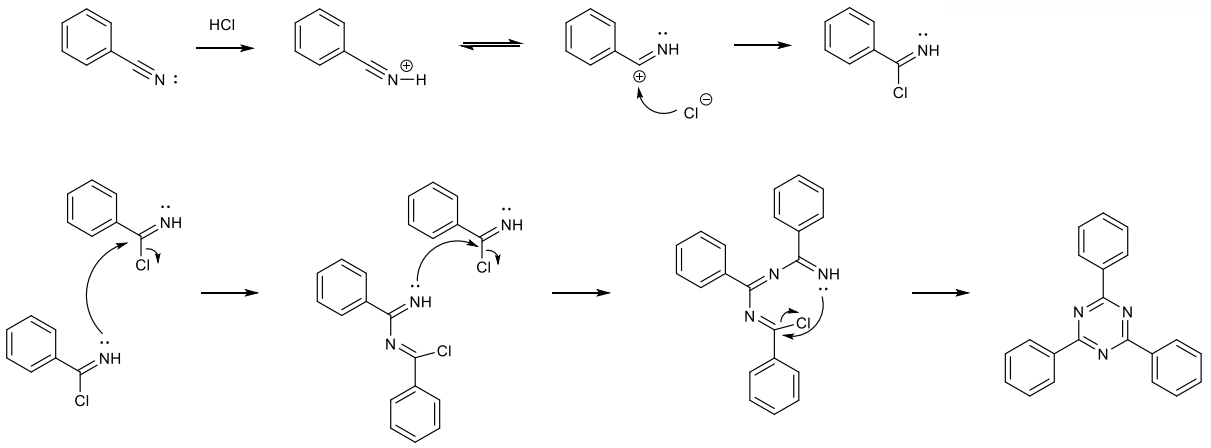

Figure 5.6. Brief mechanism of the formation of *s*-triazine of three benzoniriles under the acid catalyst.

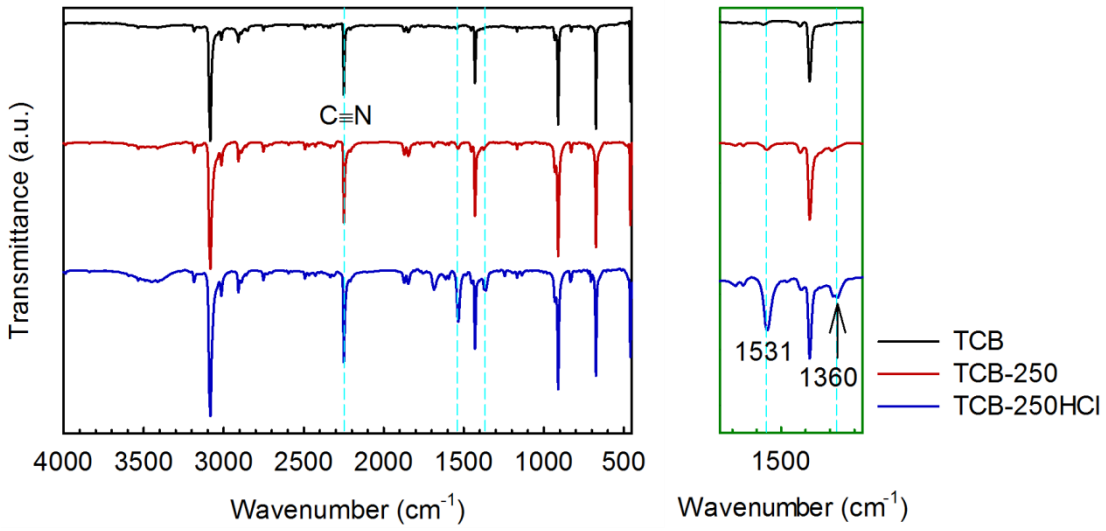

Figure 5.7. Fourier transform infrared spectroscopy (FT-IR) spectra of TCB, TCB-250 and TCB-250HCl. The *s*-triazine of TCB-250HCl vibrated at both 1531 and 1360 cm^{-1}. The sp^2 C-H stretching peak from TIPN was shifted at 3074 cm^{-1} compared with that of TCB at 3084 cm^{-1} due to resonance effects between benzene and the *s*-triazine ring.

Differential scanning calorimetry (DSC) indicates that the melting temperature of TCB is 260 °C (Figure 5.5), but the temperature of cyclotrimerization of nitrile groups is typically above 300 °C. Acid catalysts may play an important role for the formation of *s*-triazine from three nitrile groups of TCB under much milder conditions (Figure 5.6).[39,40] Still, the acid-catalyzed cyclotrimerization of TCB requires liquid-phase reaction in solution and/or a molten state.

For the solid-state reaction, we have chosen dry gaseous hydrogen chloride (HCl) as a catalyst for the following reasons: 1) to efficiently remove catalyst during work-up procedures, 2) to avoid use of solvents for green chemistry, and 3) to minimize the formation of by-products, such as conversion of

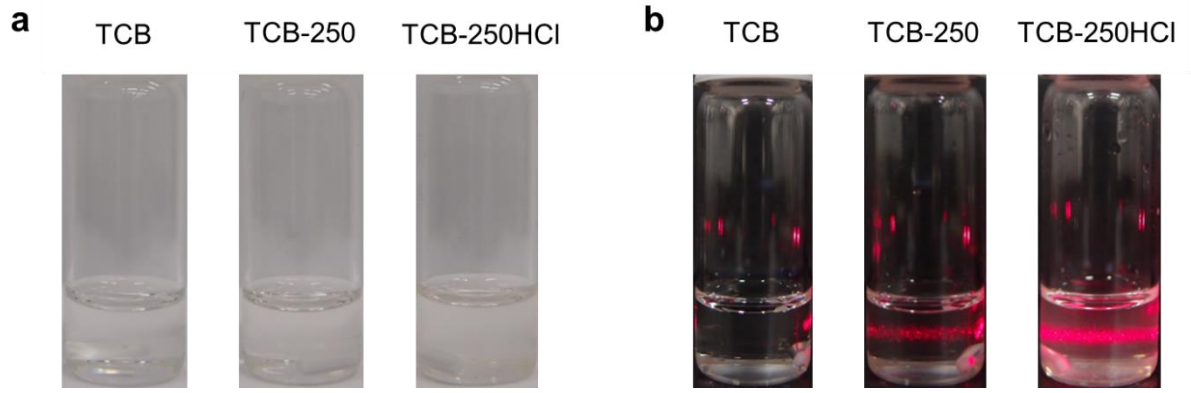

Figure 5.8. The solubility of TCB, TCB-250 and TCB-250HCl in NMP (concentration: 2 mg mL^{-1}): (a) under the light, (b) in the dark inside with a laser penetration for Brownian motion. Dispersed particles indicated TIPN in each solution.

nitrile into carboxylic acid in the presence of acid and moisture. To figure out the role of HCl, control reactions were carried out with and without the presence of HCl at 250 °C (samples denoted as TCB-250HCl and TCB-250, respectively). In the case of TCB-250, no reaction occurred, as evidenced by Fourier transform infrared spectroscopy (FT-IR) (Figure 5.7). The negligible peak intensities of *s*-triazine from TCB-250 were observed at both 1531 and 1360 cm^{-1}. They are almost identical to those of the starting TCB. On the other hand, TCB-250HCl shows strong *s*-triazine peaks, suggesting that only thermal annealing TCB at 250 °C in the presence of HCl can induce the formation of *s*-triazine in solid-state (Figure 5.7 and 5.8). However, the yield of TCB-250HCl was low (~ 6%). We speculated that the yield was low because only the exposed surface of the TCB single crystals had contact with the HCl catalyst and cyclized to form *s*-triazine. As described in the detailed illustrations of the single crystal structure of TCB (Figure 5.3), TCB molecules at the surface have more freedom of motion before melting. The mechanism for cyclotrimerization causes the TCB molecules to first form α-halogenated alkyl cyanides with HCl, and then to cyclize into *s*-triazine rings in solid-state.[40] Therefore, preformed triazine frameworks were stable enough for further heat-treatment at 500 °C, which greatly increased yield (21.3%; sample denoted as TCB-500HCl, Figure 5.1b). After incremental increase of the reaction temperature to 500 °C, the crystal morphology still remained (Figure 5.2c), indicating the stability of the products.

The structure of the resultant TCB-500HCl was determined by single-crystal XRD (Figures 5.9-11, and Table 5.2). TCB-500HCl turned out to be TIPN, which has monoclinic crystal structure with space group *C*12/c1. The crystal packing structure shows that the TIPN molecules are aligned along the crystallographic *b*-axis with a 26° tilt from the crystallographic *ac*-plane (Figure 5.9a), and are interdigitated to form a one-dimensional (1D) zig-zag ribbon structure (Figures 5.9, 5.10c and d). The molecules aligned along the crystallographic *b*-axis are π-π stacked to form a 1D column (Figures 5.9a and 5.10e). The combination of interdigitation and π-π stacking leads to corrugated 2-D sheets, which

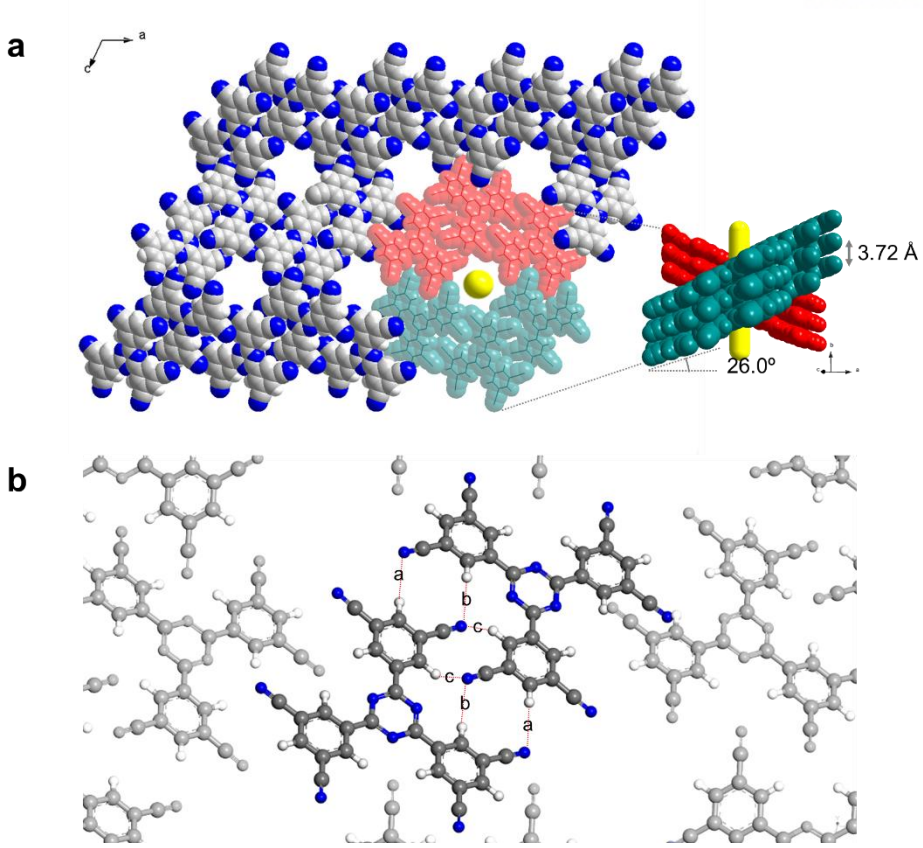

Figure 5.9. (a) CPK diagram of TIPN viewed along the crystallographic b-axis. The yellow ball and stick represent traces of water at partial occupancy sites in the solvent channels (color codes: grey = carbon; blue = nitrogen; white = hydrogen). (b) Ball-and-stick packing diagram of TIPN crystal and red lines indicate interdigitation between two TIPNs by dipole-dipole interactions with each distance; a: 2.75 Å; b: 2.76 Å and c: 2.71 Å.

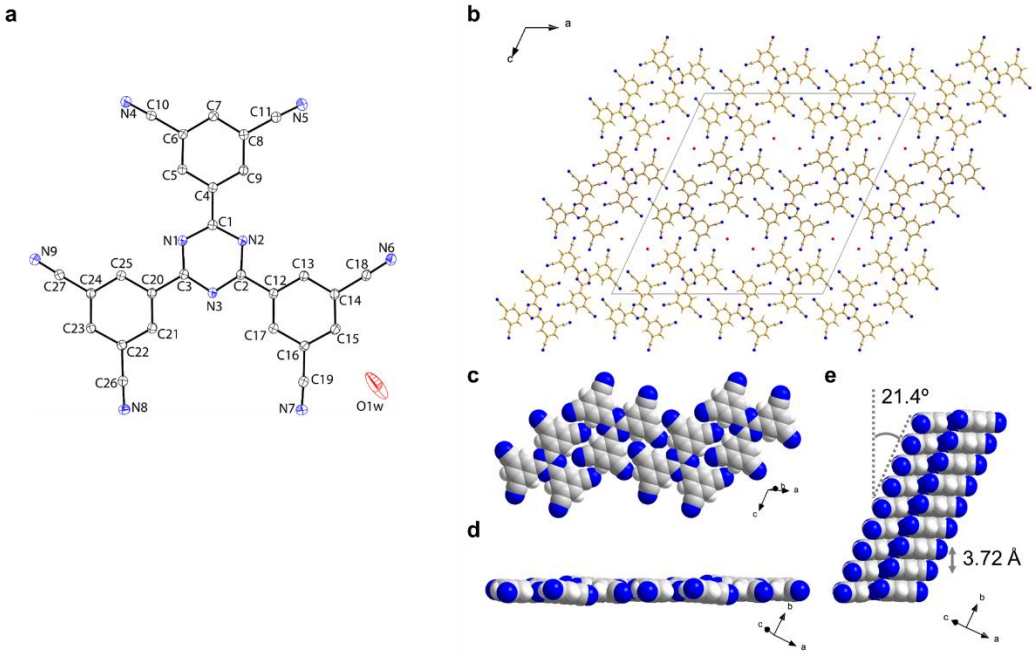

Figure 5.10. (a) ORTEP drawing of TIPN. (b) Ball-and-stick packing diagram of TIPN viewed along the crystallographic *b*-axis. The red balls represent traces of water at partial occupancy sites in the solvent channels. (c) CPK diagram of the interdigitated 1D zig-zag ribbon structure viewed from *b*-axis perpendicular to *ac*-plane, and (d) along the *ac*-plane of the molecules. (e) CPK diagram of the π-π stacked 1D column viewed (a) in parallel.

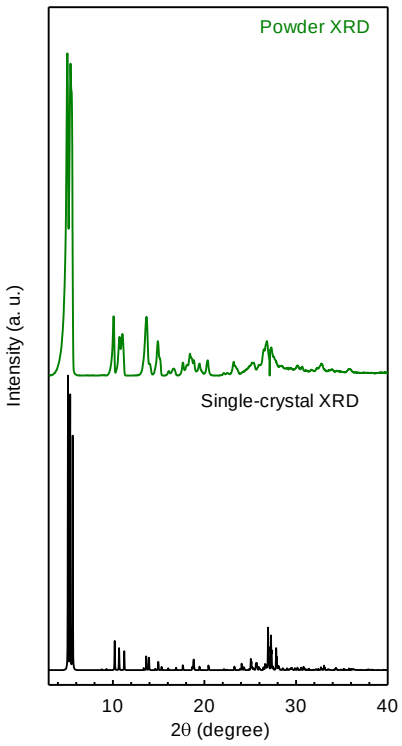

Figure 5.11. PXRD and single crystal XRD patterns of TIPN.

Table 5.2. Crystallographic data for TIPN

Identification	TIPN
Empirical formula	$C_{27}H_{9.35}N_9O_{0.17}$
Formula weight	462.58
Temperature	100(2) K
Wavelength	0.650 Å
Crystal system	Monoclinic
Space group	*C*2/*c*
Unit cell dimensions	a = 36.530(7) Å, α = 90° b = 3.7210(7) Å, β = 114.89(3)° c = 38.242(8) Å, γ = 90°
Volume	4715.2(19) $Å^3$
Z	8
Density (calculated)	1.303 Mg m^{-3}
Absorption coefficient	0.070 mm^{-1}
F(000)	1886
Crystal size	0.028 x 0.015 x 0.015 mm^3
Theta range for data collection	2.813 to 27.998°
Index ranges	–51<=h<=52, –5<=k<=5, –55<=l<=54
Reflections collected	13594
Independent reflections	7347 [R(int) = 0.0484]
Completeness to theta = 22.955°	98.8%
Absorption correction	Semi-empirical from equivalents
Max. and min. transmission	0.999 and 0.998
Refinement method	Full-matrix least-squares on F^2
Data / restraints / parameters	7347 / 0 / 335
Goodness-of-fit on F^2	1.029
Final R indices [I>2sigma(I)]	R1 = 0.0707, wR2 = 0.1918
R indices (all data)	R1 = 0.1233, wR2 = 0.2273
Largest diff. peak and hole	0.369 d –0350 e·$Å^{-3}$

form a series of 1D solvent channels of 6.5-Å diameter along the crystallographic *b*-axis in a crystallographic two-fold symmetry (Figure 5.9a). The crystal channel maintained itself without guest solvent, however, a trace of moisture (0.17 mol.%) was contained in the vacant channels of TIPN (Figure 5.10b and Table 5.2). Additionally, the powder XRD pattern supported proof of uniformity in the bulk of TIPN (Figure 5.11). Regarding the poly(*s*-triazine) network, CFT-0, which is synthesized by ionothermal reaction from TCB in the presence of zinc chloride ($ZnCl_2$) as a catalyst,[36] there were no clear XRD patterns observed like those of TIPN crystal in this study. Hence, the powder XRD patterns shown in Figure 5.11 are a unique feature of TIPN single crystals. This result, in turn, implies that stagnant cyclotrimerization of TCB had occurred rather than subsequent extension into a CTF-0 network polymer in solid-state.

Density functional theory (DFT) calculations were performed to understand how strongly TIPN molecules are packed in the crystal lattice, and why subsequent polymerization of TCB ceased after formation of a single *s*-triazine into TIPN. The formation energy of a single *s*-triazine ring from three TCBs was computed to be −2.84 eV, and that of a triazine-based network polymer (CTF-0) was computed to be −2.86 eV, for the sequential formation of *s*-triazine rings (Figure 5.12). The thermodynamic energy requirement is similar for formation of a single *s*-triazine ring from TIPN and CTF-0. However, the TIPN molecules forming in the crystal lattice are thermodynamically much more stable than individual TIPN molecules (Figure 5.13a), because they are interlocked by strong dipole-dipole interaction (–C–H···N≡C–) of −1.49 eV between two TIPN molecules. They are stacked tightly by van der Waals force of −1.41 eV (Figure 5.13a), which is a much more stable and favorable state than that of TCB (Figure 5.13b). Because the TIPN molecules are tightly bound in the stable crystal structure (Figure 5.9b), they cannot extend the structure as a network polymer, CTF-0, even after annealing at 500 °C.

The morphology and crystal facets (Figure 5.14a) of TIPN were studied using scanning electron (SEM) and transmission electron (TEM) microscopy, respectively. Figures 5.14b and 5.15 show that TIPN crystals are long 1D wires with a width of approximately 1–2 μm. Significantly longer wires (> 100 μm) were also observed (Figure 5.15c). SEM energy-dispersive spectroscopy (EDS) indicated that TIPN consisted of carbon and nitrogen with little physically absorbed oxygen (Figure 5.16). The selected-area electron diffraction (SAED) pattern from the TIPN 1D wire (Figure 5.14c), which was mounted on a carbon-coated copper grid, displays a single crystal diffraction with high crystallinity. The growth direction is parallel to [010] (crystallographic *b*-axis of unit cell). A magnified SEM image (inset, Figure 5.14b) shows that the surface of a TIPN crystal is multi-faceted. To clearly investigate the cross-sectional shape of TIPN crystals, we fabricated a cross-sectioned TEM sample using a focused ion beam (FIB) (Figure 5.17). The bright-field (BF) TEM image of the cross-section of TIPN crystal indicated a hexagonal type (Figures 5.14e and 5.18a) and others of octagonal shape were observed

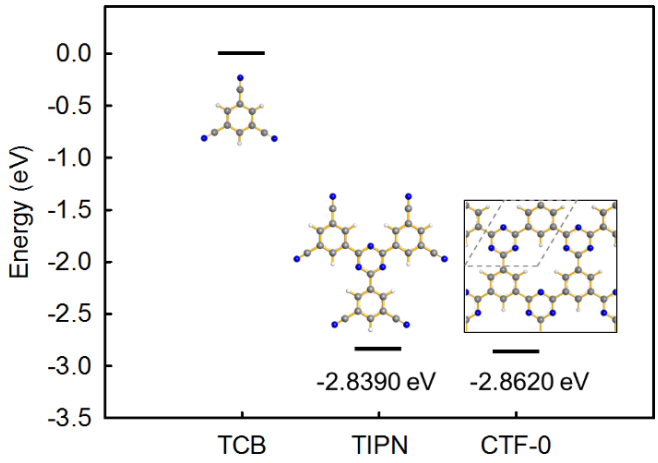

Figure 5.12. The formation energy diagram for formation of single *s*-triazine compared with TIPN and CTF-0 as the 2-dimensional polymeric crystal (color code: grey = carbon; blue = nitrogen; white = hydrogen).

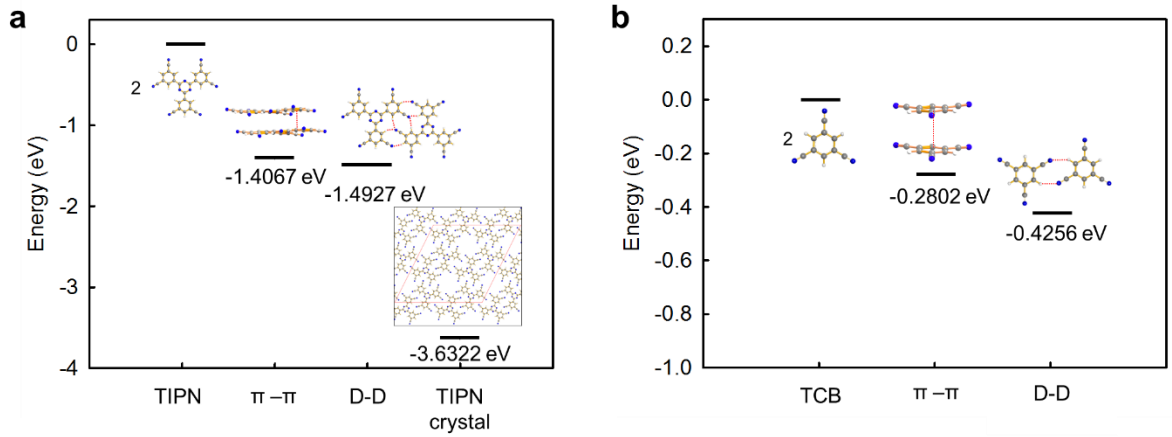

Figure 5.13. (a) The formation energy difference between TIPN and TIPN crystal composed of 8 units ($C_{216}N_{72}H_{72}$). The formation energy is computed to be −3.6322 eV per unit ($C_{27}N_9H_9$). The interaction energy of two TIPNs; van der Waals interaction (π-π) and dipole-dipole interaction (D-D) of a side of unit $C_{27}N_9H_9$ described molecules into figures. (b) The interaction energy between two TCBs in the crystal lattice, which composed of van der Waals interaction (π-π) and dipole-dipole interaction (D-D) of a side unit $C_9N_3H_3$ (color code: grey = carbon; blue = nitrogen; white = hydrogen).

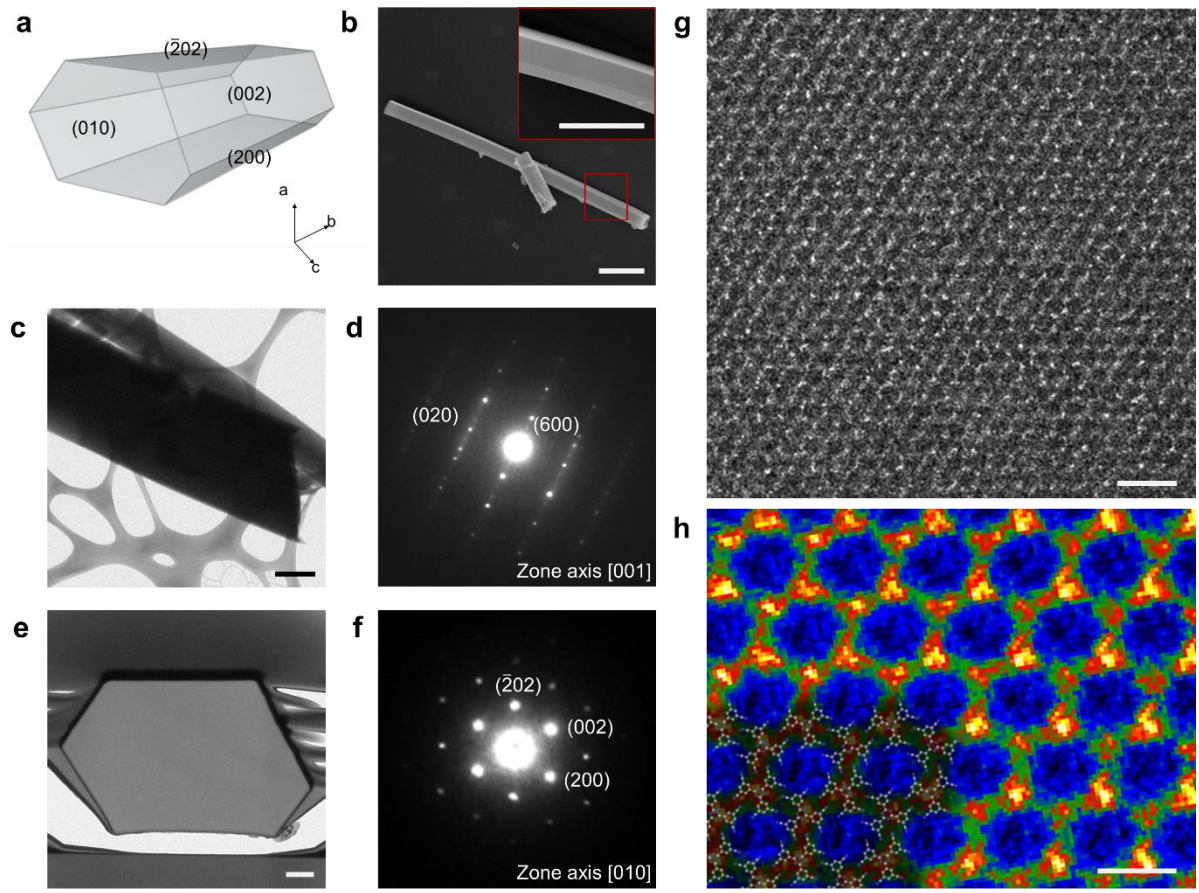

Figure 5.14. (a) Schematic diagram of TIPN crystal facets revealed by TEM; (b) SEM images of TIPN crystal: Inset is the magnified image from red square. (c) TEM images of TIPN. (d) SAED pattern from (c) region. The crystal (001) facet is parallel to the grid. (e) Cross-sectional TEM image of TIPN crystal prepared by FIB; (f) Selected area electron diffraction (SAED) pattern from (e) region depicting zone axis of [010]. The main crystal growth direction is perpendicular to the image plane, the crystallographic *b*-axis. (g) Atomic-resolution TEM image of the magnified region in (e) which shows a well-ordered crystal lattice; (h) Inverse fast-Fourier transform (IFFT) image. The image is matched with a TIPN crystallographic model determined by XRD (color codes: grey = carbon; blue = nitrogen). The scale bars indicate: (b) 5 μm; (c) 500 nm; (e) 200 nm; (g) 5 nm; (h) 2 nm.

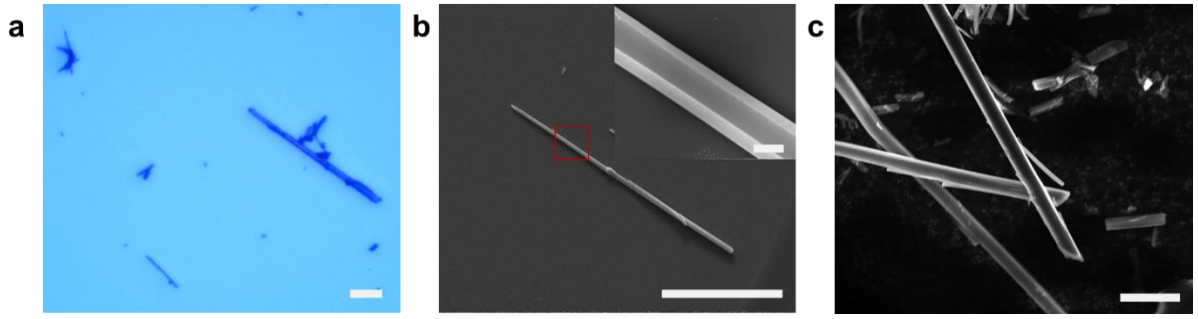

Figure 5.15. (a) Optical microscopy images of TIPN crystalline. The scale bars indicate 20 μm. (b) SEM images of TIPN with scale bar is 50 μm and the inset is a magnified image of the region marked with a red box with the scale bar of 1 μm. (c) SEM image shows TIPN powder (scale bar: 50 μm).

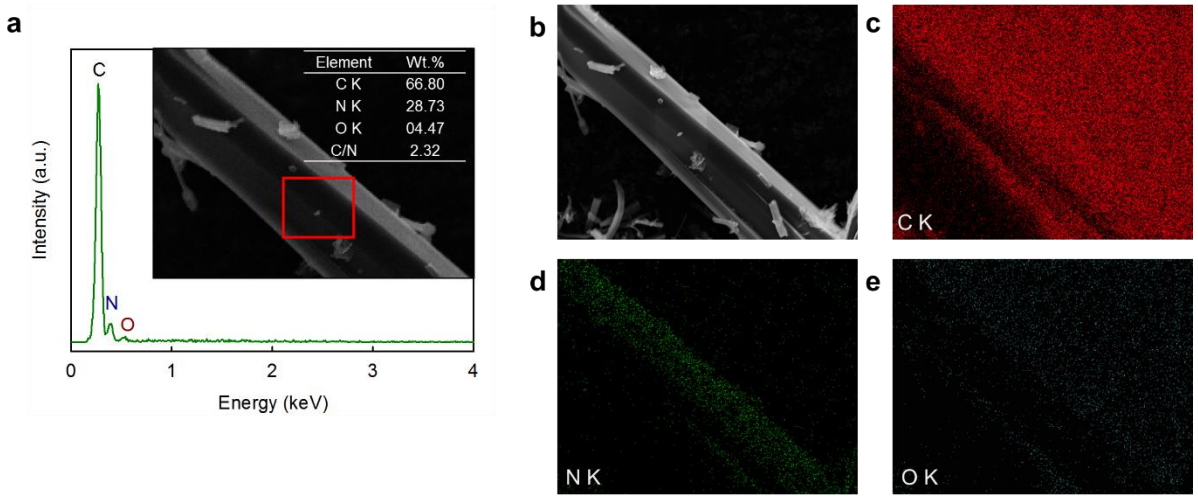

Figure 5.16. (a) EDX spectrum of TIPN. EDX spectrum was collected in marked region. Inset table recorded the EDX quantitate analysis and EDX mapping of TIPN: (b) SEM image, (c) carbon, (d) nitrogen and (e) oxygen.

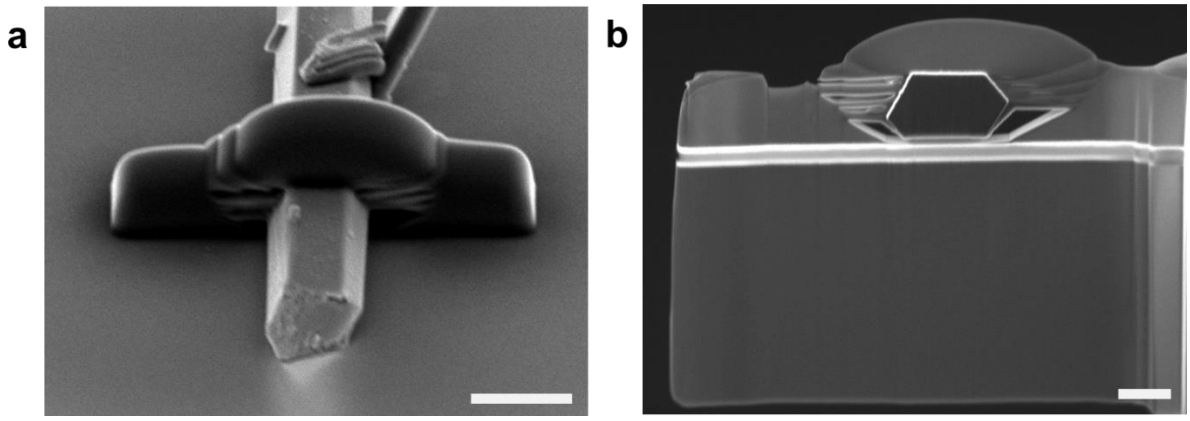

Figure 5.17. FIB milling process of TIPN. (a) Deposited carbon layers onto TIPN crystal rod for FIB milling. (b) Cross section of TIPN crystal, showing the hexagon shape. Scale bars: (a) 2 μm and (b) 1 μm.

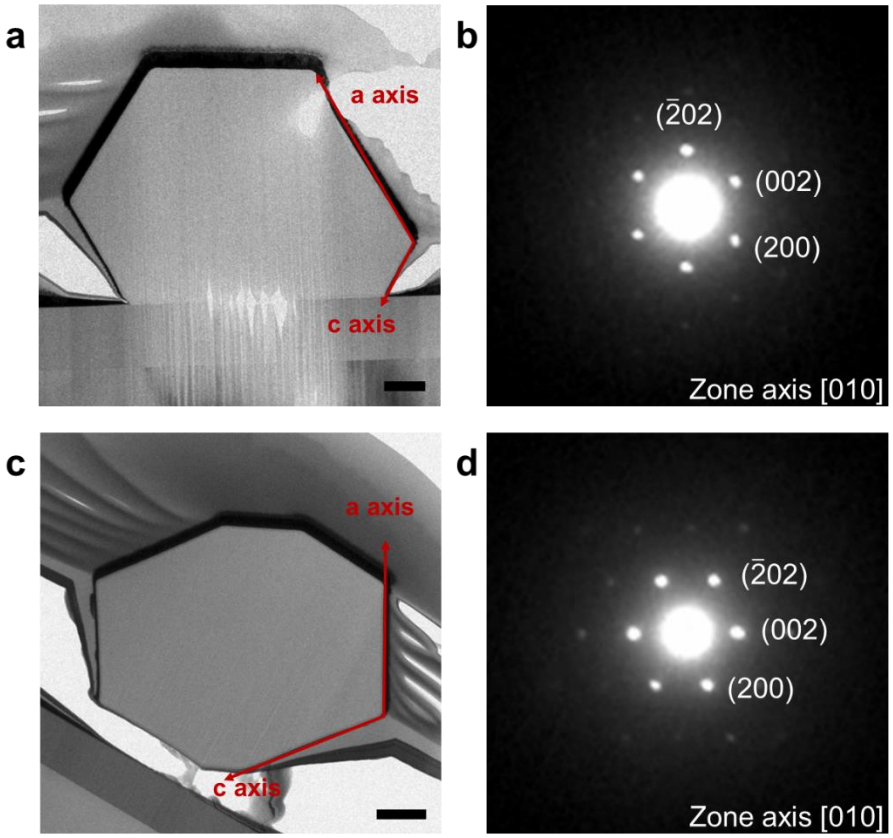

Figure 5.18. (a) The image of hexagonal cross-section of TIPN crystalline rod prepared by FIB. The main axes are indicated single crystal axis. The scale bar indicates 200 nm. (b) The selected area electron diffraction (SAED) pattern from (a) region depicting zone axis of [010]. (c) the octagonal cross-section of TIPN crystalline fabricated by FIB milling process of TIPN. The scale bar indicates 300 nm. (d) SAED pattern from (c) region having zone axis of [010]. SAED patterns ((b) and (d)) follow same trends having hexagonal spots.

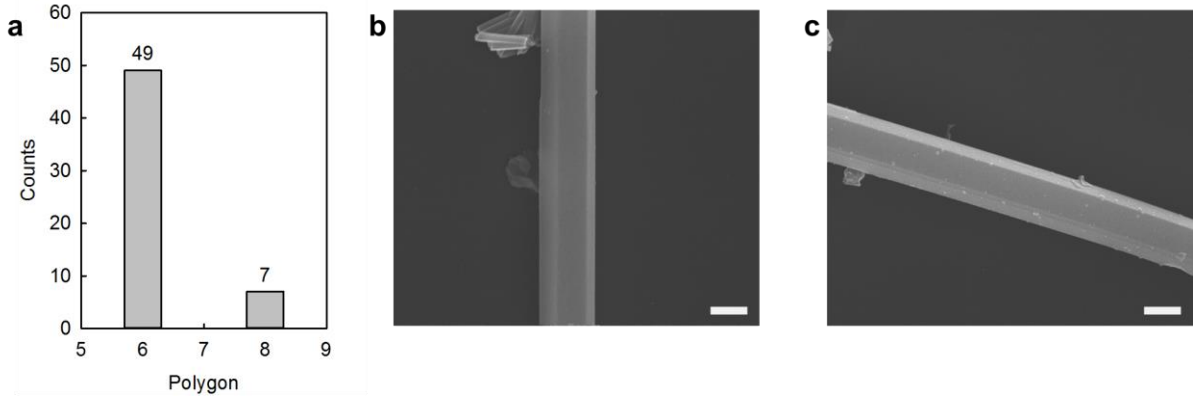

Figure 5.19. (a) The polygons of TIPN crystal distribution. The ratio of 87.5% occupied hexagonal shape and 12.5% took octagonal shape in cross-section. (b) The hexagonal cross-section has three faces and (c) the octagonal cross-section has the four faces. The scale bars indicate 1 μm.

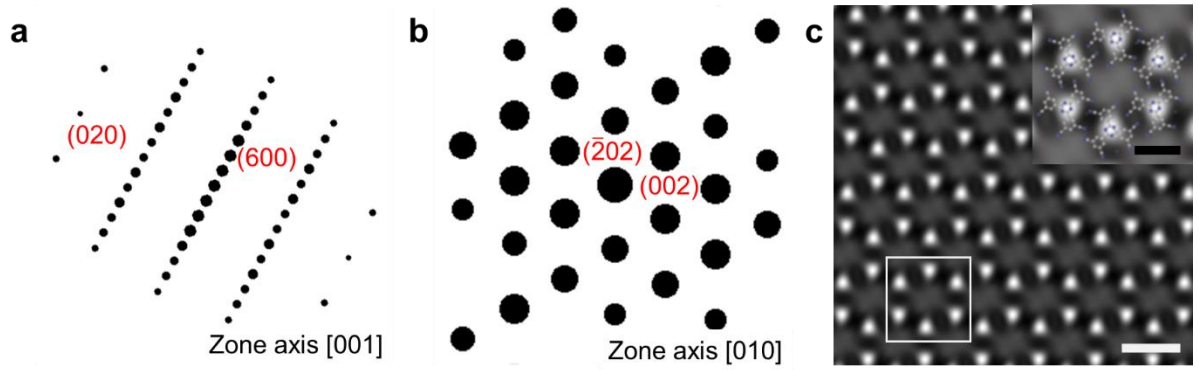

Figure 5.20. (a) The simulated SAED pattern of TIPN having zone axis of [001]. (b) Simulated SAED pattern having zone axis [010] and (c) simulated TEM image of cross-section of TIPN crystal image having zone axis [010]. The scale bar indicates 2 nm. The inset is a magnified image of the region marked with a white box, which is decorated by TIPN molecules and scale bar indicates 1 nm.

(Figure 5.18c). The major cross-section was the hexagonal type (~78.5%), which may be related to surface energy minimization (Figure 5.19). For assigning crystal facets, it is also noted that the SAED pattern (Figure 5.14f) from the cross-section samples was well matched with the simulated electron diffraction (ED) pattern (Figure 5.20b) of the above-mentioned monoclinic crystal structure, which is viewed along the [010] direction. The hexagonal surface facets are mainly composed of (−202), (002), and (200) planes, as schematically described in Figure 5.14a. It is challenging to observe high-resolution TEM (HR-TEM) images of the pores of organic materials, because they are easily damaged by strong electron beam irradiation, or require special conditions such as cryogenic temperature.[41] However, the TIPN crystals were so robust as to endure an electron beam operated at 80 kV. Therefore, we were able to obtain the HR-TEM cross-section images shown in Figures 5.14g and 5.21a, which

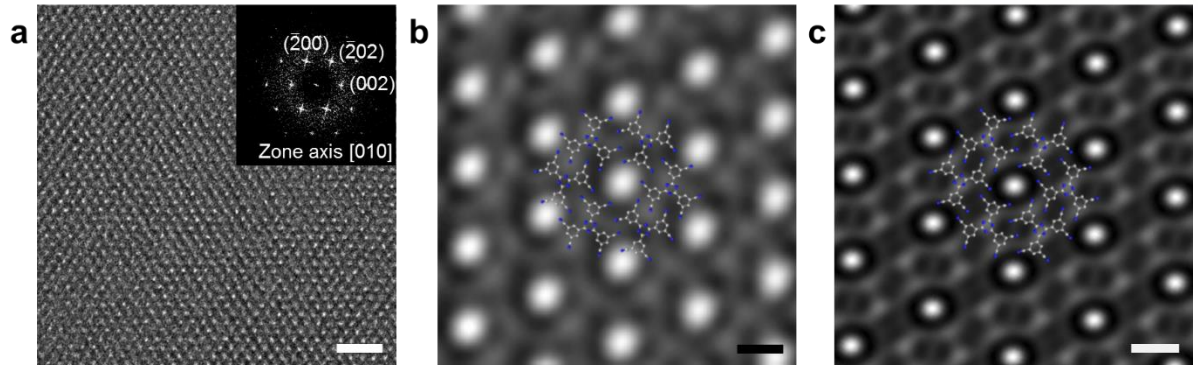

Figure 5.21. (a) The high-resolution TEM image and corresponding a fast-Fourier transform (FFT) pattern. (b) The inverse fast-Fourier transform (IFFT) image from (a). The lattice image indicates a regularly ordered crystalline. (c) The simulated IFFT images the calculated TIPN molecular model. The white contrast indicates a vacant pore (color codes: grey = carbon; blue = nitrogen). The scale bars: (a) 5 nm, (b) 1 nm and (c) 1 nm.

show well-ordered quasi-molecular frameworks. Furthermore, the inverse fast-Fourier transform (IFFT) image (Figure 5.14h) clearly visualizes the channel, which was described by a crystallographic atomic TIPN model (Figure 5.9). This result is in good agreement with a simulated HR-TEM image confirming the existence of columnar channels (Figure 5.20c). The bond nature and the qualitative analysis by electron energy loss spectroscopy (EELS) suggest that TIPN consists of carbon and nitrogen atoms (Figure 5.22).

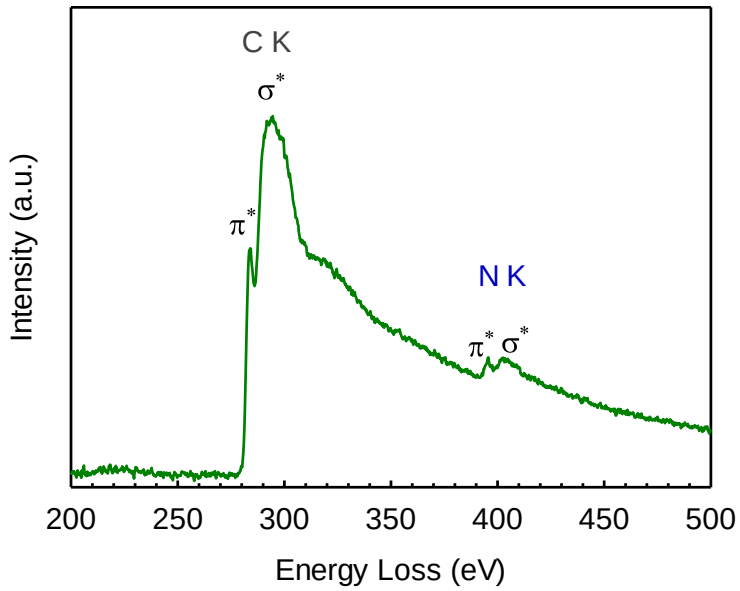

Figure 5.22. The K-shell excitation of carbon and nitrogen from electron energy loss spectroscopy (EELS) spectrum of TIPN.

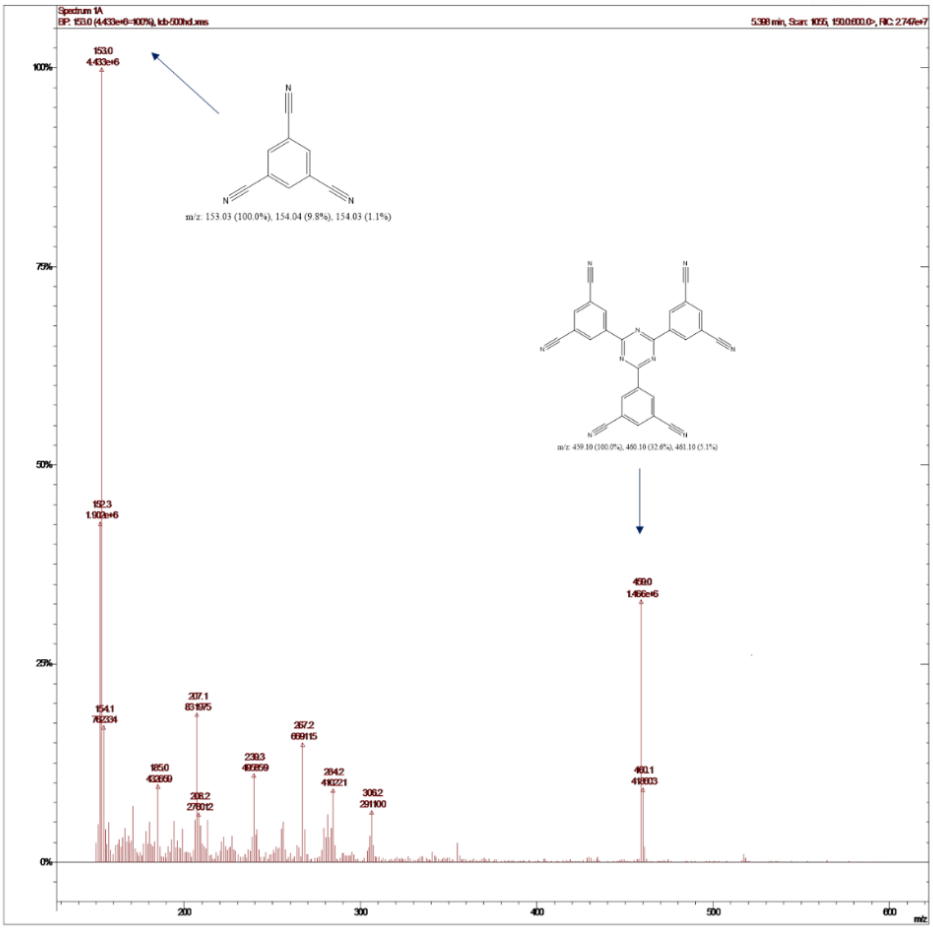

Figure 5.23. Electron ionized mass spectroscopy of TIPN, which is 459.0 *m/z* (M^+, calcd. 459.10). TIPN defragmented into an initial starting reactant TCB, originated in *s*-triazine, which was destroyed by strong electron source at *m/z* 153.0 (M^+, calcd. 153.03).

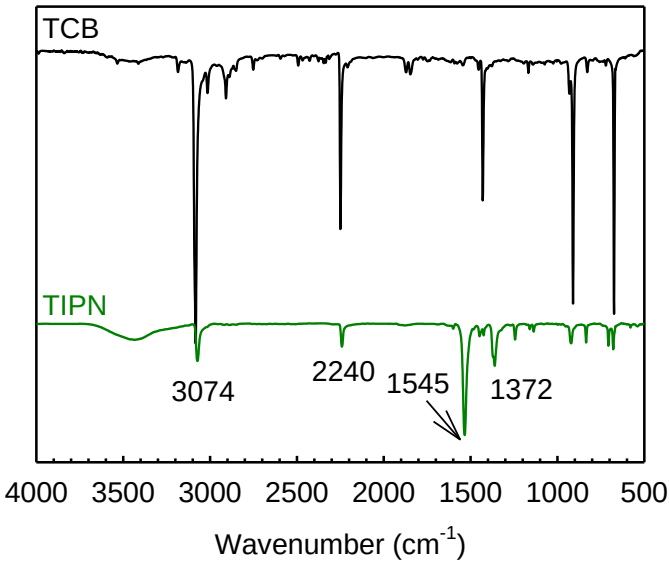

Figure 5.24. FT-IR spectra of TIPN and TCB.

Spectroscopic analyses were also carried out to provide additional information about the structure of TIPN. The ionized molecular mass of TIPN by electron ionization mass spectroscopy (EI-MS) was precisely matched with calculated values (Figure 5.23). In addition, the bond nature of TIPN was further determined using Fourier transform infra-red (FT-IR) spectroscopy, indicating that *s*-triazine rings show strong peaks at both 1545 and 1372 cm^{-1} (Figure 5.24).[42] As expected from the crystal lattice information (Figure 5.9), DFT calculations (Figure 5.13a) and *e*-beam tolerance (Figure 5.14g), TIPN crystals have high stability. Indeed, TIPN crystals showed unusually high thermal stability (Figure 5.25) due to their planar structure and each nitrile group tightly interlocked with other nitrile groups in the crystal lattice. The maximum decomposition temperature was as high as 605 °C in nitrogen gas. After heating to 1000 °C, the char yield was 5.8% (inset, Figure 5.25).

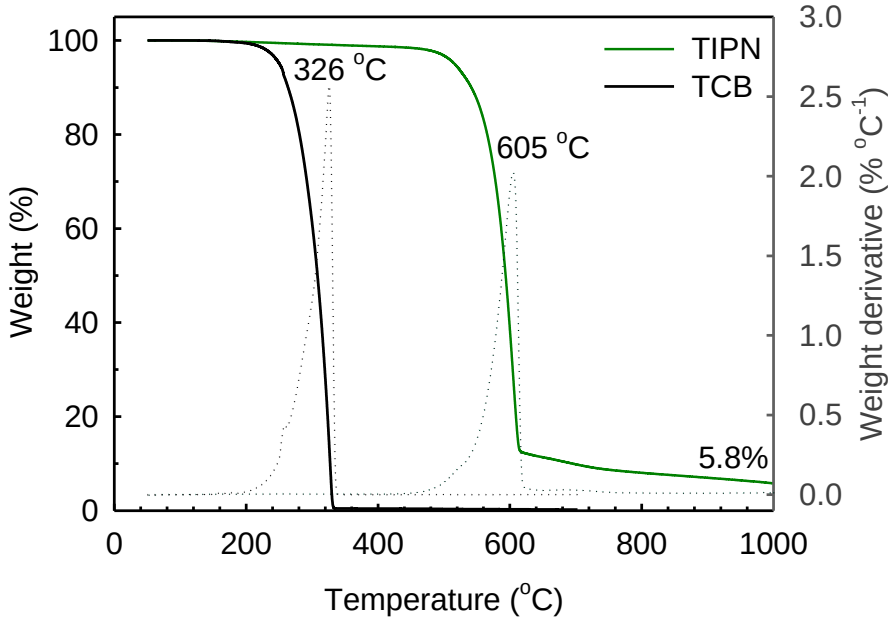

Figure 5.25. TGA thermograms of TCB and TIPN obtained with ramping rate of 10 °C min^{-1}. TIPN shows unusually high thermal stability under nitrogen gas. Inset is a photograph of residue at 1000 °C.

To determine details of the 1D inner channel of TIPN crystals, gas absorption/desorption were carried out using Brunauer-Emmett-Teller (BET) measurements. The cavity volume was 15.3% in TIPN crystals, which was calculated using PLATON software (the accessible volume by a 1.2 Å probe and the cell volume). Thus, we could confirm the presence of a cavity in TIPN, which adsorbed nitrogen gas (up to 17.26 $cm^3\ g^{-1}$) at 77 K and carbon dioxide to 12.73 $cm^3\ g^{-1}$ at 196 K and 0.96 bar, showing typical micropore isotherms (Figure 5.26). In the cylindrical channel, TIPN adsorbed CO_2 better at < 0.9 bar than N_2. This is because CO_2 is slightly thinner than N_2 even if they are linear molecules, and because there is electrostatic interaction between a surface with abundant π-electrons and the CO_2

molecule.[43] The BET surface area calculated from CO_2 adsorption was 41.50 m^2 g^{-1} at 196 K, with a pore volume of 7.15 cm^3 g^{-1}. Although the calculated BET surface area and gas adsorption amount are relatively low due to the narrow channel diameter (~ 6.5 Å), we confirmed a channel cavity.

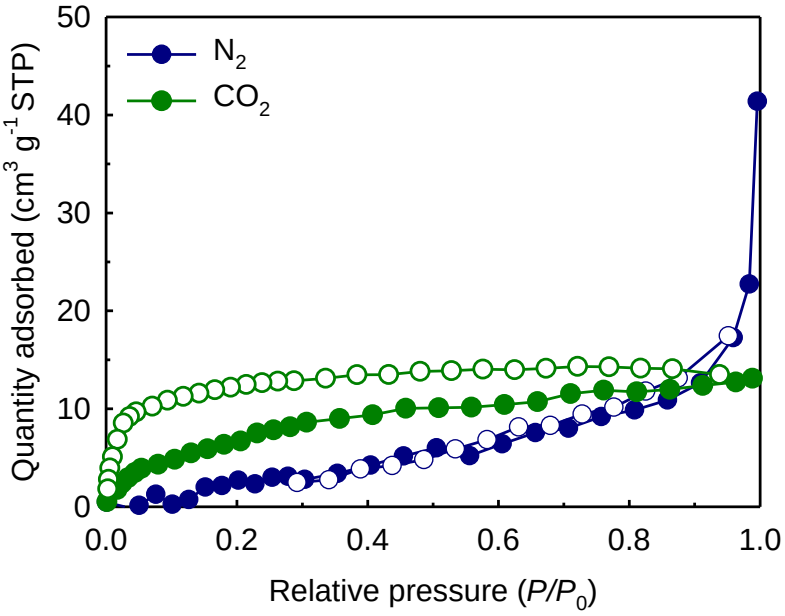

Figure 5.26. Gas adsorption/desorption isotherms of TIPN with N_2 at 77 K and CO_2 at 196 K (filled circle for absorption and open circle for desorption).

5. 6 Conclusions

In summary, the superstructure of TIPN was, for the first time, realized using stagnate cyclotrimerization of TCB single crystals in solid-state. The formation of TIPN superstructure was confirmed by single crystal XRD and visualized by TEM, confirming that hexagonally packed TIPN molecules with C_3 symmetry and six nitrile groups interlocked into a 1-dimensional rod with concentric hollow channels. The TIPN superstructure displayed unusually high thermal stability and *e*-beam tolerance due to interdigitated TIPN molecules forming a quasi-molecular framework. The formation of TIPN-based robust superstructure may open up a new class of stable organic frameworks. Thus, this new class of stable molecular frameworks will be useful for many applications, ranging from wet chemistry to specific devices.

5.7 References

1. Merrifield, R. B. *J. Am. Chem. Soc.* **1963**, *85*, 2149.
2. Rothenberg, G.; Downie, A. P.; Raston, C. L.; Scott, J. L. *J. Am. Chem. Soc.* **2001**, *123*, 8701.
3. Toda, F. *Acc. Chem. Res.* **1995**, *28*, 480.
4. Ramamurthy, V.; Venkatesan, K. *Chem. Rev.* **1987**, *87*, 433.
5. Baroncini, M.; d'Agostino, S.; Bergamini, G.; Ceroni, P.; Comotti, A.; Sozzani, P.; Bassanetti, I.; Grepioni, F.; Hernandez, T. M.; Silvi, S.; Venturi, M.; Credi, A. *Nat. Chem.* **2015**, *7*, 634.
6. Paul, I. C.; Curtin, D. Y. *Acc. Chem. Res.* **1973**, *6*, 217.
7. Baig, R. B. N.; Varma, R. S. *Chem. Soc. Rev.* **2012**, *41*, 1559.
8. Biswal, B. P.; Chandra, S.; Kandambeth, S.; Lukose, B.; Heine, T.; Banerjee, R. *J. Am. Chem. Soc.* **2013**, *135*, 5328.
9. Seo, J. S.; Whang, D.; Lee, H.; Jun, S. I.; Oh, J.; Jeon, Y. J.; Kim, K. *Nature* **2000**, *404*, 982.
10. Sozzani, P.; Bracco, S.; Comotti, A.; Ferretti, L.; Simonutti, R. *Angew. Chem. Int. Ed.* **2005**, *44*, 1816.
11. Yu, V. Z.; Zorkii, P. M. *Russ. Chem. Rev.* **1989**, *58*, 421.
12. Enright, G. D.; Udachin, K. A.; Moudrakovski, I. L.; Ripmeester, J. A. *J. Am. Chem. Soc.* **2003**, *125*, 9896.
13. Watanabe, M.; Chang, Y. J.; Liu, S. W.; Chao, T. H.; Goto, K.; Islam, M. M.; Yuan, C. H.; Tao, Y. T.; Shinmyozu, T.; Chow, T. J. *Nat. Chem.* **2012**, *4*, 574.
14. Desiraju, G. R. *Acc. Chem. Res.* **1991**, *24*, 290.
15. Desiraju, G. R. *Angew. Chem. Int. Ed.* **1995**, *34*, 2311.
16. Gilday, L. C.; Robinson, S. W.; Barendt, T. A.; Langton, M. J.; Mullaney, B. R.; Beer, P. D. *Chem. Rev.* **2015**, *115*, 7118.
17. Li, H.; Eddaoudi, M.; O'Keeffe, M.; Yaghi, O. M. *Nature* **1999**, *402*, 276.
18. Furukawa, S.; Reboul, J.; Diring, S.; Sumida, K.; Kitagawa, S. *Chem. Soc. Rev.* **2014**, *43*, 5700.
19. Belman, N.; Israelachvili, J. N.; Li, Y.; Safinya, C. R.; Ezersky, V.; Rabkin, A.; Sima, O.; Golan, Y. *Phys. Chem. Chem. Phys.* **2011**, *13*, 4974.
20. Côté, A. P.; Benin, A. I.; Ockwig, N. W.; O'Keeffe, M.; Matzger, A. J.; Yaghi, O. M. *Science* **2005**, *310*, 1166.
21. Feng, X.; Ding, X.; Jiang, D. *Chem. Soc. Rev.* **2012**, *41*, 6010.
22. Tozawa, T.; Jones, J. T. A.; Swamy, S. I.; Jiang, S.; Adams, D. J.; Shakespeare, S.; Clowes, R.; Bradshaw, D.; Hasell, T.; Chong, S. Y.; Tang, C.; Thompson, S.; Parker, J.; Trewin, A.; Bacsa, J.; Slawin, A. M. Z.; Steiner, A.; Cooper, A. I. *Nat. Mater.* **2009**, *8*, 973.
23. Hisaki, I.; Senga, H.; Shigemitsu, H.; Tohnai, N.; Miyata, M. *Chem. Eur. J.* **2011**, *17*, 14348.
24. Mitra, T.; Wu, X.; Clowes, R.; Jones, J. T. A.; Jelfs, K. E.; Adams, D. J.; Trewin, A.; Bacsa, J.; Steiner, A.; Cooper, A. I. *Chem. Eur. J.* **2011**, *17*, 10235.

25. Rapid Auto software, R.-A. s., Cat. No. 9220B101, Rigaku Corporation.
26. Sheldrick, G. M. *Acta crystallographica. Section A, Foundations of crystallography* **2008**, *64*, 112.
27. Arvai, A. J.; Nielsen, C. *ADSC Quantum-210 ADX Program* Area Detector System Corporation: Poway, CA, USA, 1983.
28. Otwinowski, Z.; Minor, W. *Processing of X-ray diffraction data collected in oscillation mode*; Academic Press: New York, 1997; Vol. 276.
29. Sheldrick, G. M. *Acta Crystallogr. C Struct. Chem.* **2015**, *71*, 3.
30. Perdew, J. P.; Burke, K.; Ernzerhof, M. *Phys. Rev. Lett.* **1996**, *77*, 3865.
31. Hohenberg, P.; Kohn, W. *Phys. Rev. B* **1964**, *136*, B864.
32. Kohn, W.; Sham, L. J. *Phys. Rev.* **1965**, *140*, A1133.
33. Kresse, G.; Furthmüller, J. *Phys. Rev. B* **1996**, *54*, 11169.
34. Kresse, G.; Furthmuller, J. *Comp. Mater. Sci.* **1996**, *6*, 15.
35. Grimme, S. *J. Comput. Chem.* **2006**, *27*, 1787.
36. Katekomol, P.; Roeser, J.; Bojdys, M.; Weber, J.; Thomas, A. *Chem. Mater.* **2013**, *25*, 1542.
37. Hao, L.; Ning, J.; Luo, B.; Wang, B.; Zhang, Y.; Tang, Z.; Yang, J.; Thomas, A.; Zhi, L. *J. Am. Chem. Soc.* **2015**, *137*, 219.
38. Bengelsdorf, I. S. *J. Am. Chem. Soc.* **1958**, *80*, 1442.
39. Hinkel, L. E.; Dunn, R. T. *J. Chem. Soc.* **1930**, 1834
40. Grundmann, C.; Kreutzberger, A. *J. Am. Chem. Soc.* **1954**, *76*, 5646.
41. Kissel, P.; Erni, R.; Schweizer, W. B.; Rossell, M. D.; King, B. T.; Bauer, T.; Gotzinger, S.; Schluter, A. D.; Sakamoto, J. *Nat. Chem.* **2012**, *4*, 287.
42. Kuhn, P.; Antonietti, M.; Thomas, A. *Angew. Chem. Int. Ed.* **2008**, *47*, 3450.
43. Hisaki, I.; Nakagawa, S.; Tohnai, N.; Miyata, M. *Angew. Chem. Int. Ed.* **2015**, *54*, 3008.

Chapter VI. Conclusions

Carbon is an abundant element in earth and crucial composition from organic to inorganic materials. Advanced materials, for example, graphene-like 2-dimensional periodic materials, show outstanding physical and chemical properties and it is ready to introduce new area from the advanced material.

First, we prepared heteroatoms doped graphene with boron/nitrogen *via* Wurtz reaction for tuning the bandgap. Successfully, boron and nitrogen co-doped graphene was prepared and boron and nitrogen interaction helps to be introduced into graphitic carbon structure. It showed semiconductor behavior, even though on/off ratio is relatively low (10.7) calculated from FET devices, but it shows the potentials to control the bandgap and processibility.

Second, boron-doped graphene shows high stability and provides the catalytic sites for reduction of cobalt type electrolyte in dye-sensitive solar cell as a counter electrode. Platinum as a precious metal used not only many commercial catalysts but also counter electrode for electrolyte reduction in DSSC. Replacing Pt counter electrode, boron-doped graphene shows superior performance and power conversion efficiency was recorded on 9.21% than Pt (8.45%) because of lower charge-transfer resistance and stable electrochemical stability.

Third, graphitic carbon sheets with random hole-defects were synthesized as a 2D material. Combined synthesis process with dehydration and thermal reaction, resulted from well-ordered graphitic structures were formed with high BET surface arear. Depending on the carbon precursor Study on these materials are working now. This GCS is a paramagnet under 10 K, however, similar graphitic structure graphene is a diamagnetic. As a view of the material, we predict that the modified graphitic structure based on graphene has diverse applications exploiting GCSs advantages.

Fourth, TIPN superstructure was synthesized by solid-state reaction and interdigitated nitrile interactions in the single crystal guaranteed robust architecture like macromolecules. TIPN crystal has 1D channel with 6.5-Å diameter along the crystallographic *b*-axis3. Also, TIPN was observed the pore through TEM clearly.

In summary, carbon-based materials were prepared by various methods, built up 2D and 3D structures from precursors, and characterized thoroughly. Prepared carbon-based materials were shown the potentials to apply in electronic devices and energy conversion and storage systems.

Appendix I. Curriculum Vitae

Sun-Min Jung

Department of Energy Engineering, Ulsan National Institute of Science and Technology (UNIST)
104-708, UNIST-gil 50, Ulsan, Republic of Korea
Phone: +82-52-217-2571, E-mail: sunminj@unist.ac.kr
Research ID: D-4662-2017 (http://www.researcherid.com/rid/D-4662-2017)

Education

Mar. 2011 – Aug. 2017	**Combined Master & PhD course, Energy Engineering** Ulsan National Institute of Science and Technology (UNIST), Ulsan, Republic of Korea ***Thesis***: Two- and Three-Dimensional Network Structures from Design to Application ***Research Advisor***: Prof. Jong-Beom Baek
Mar. 2007 – Feb. 2011	**Bachelor of Engineering, Chemical Engineering** Chungbuk National University, Cheongju, Chungbuk, Republic of Korea

Experiences

Mar. 2011 – Dec. 2014	RA/TA scholarship, UNIST
Mar. 2011 – Aug. 2011	T.A., School of Nano-bioscience and Chemical Engineering, UNIST Course: Advanced Chemical Engineering Laboratory

Honors/Affiliations

Feb. 2013	Outstanding Graduate Student Award, UNIST
Nov. 2016	Outstanding Graduate Student Award, UNIST

Research Interests

Design and utilization of highly porous materials

Design and synthesis of 2D materials and 3D polymeric materials

List of Publications

Representative Paper

1. **Jung, S.-M.**; Kim, D.; Shin, D.; Mahmood, J.; Park, N.; Lah, M. S.; Jeong, H. Y.; Baek, J.-B. Unusually stable triazine-based superstructure *Angewandte Chemie International Edition* **2016**, *55*(26), 7539.
2. **Jung, S.-M**.; Lee, E. K.; Choi, M.; Shin, D.; Jeon, I.-Y.; Seo, J.-M.; Jeong, H. Y.; Park, N.; Oh, J. H.; Baek, J.-B., Direct Solvothermal Synthesis of B/N-Doped Graphene. *Angewandte Chemie International Edition* **2014,** *53* (9), 2398.
3. **Jung, S.-M.**; Choi, I. T.; Lim, K.; Ko, J.; Kim, J. C.; Lee, J.-J.; Ju, M. J.; Kim, H. K.; Baek, J.-B., B-Doped Graphene as an Electrochemically Superior Metal-Free Cathode Material as Compared to Pt over a Co(II)/Co(III) Electrolyte for Dye-Sensitized Solar Cell. *Chemistry of Materials* **2014,** *26* (11), 3586.

Co-author Paper

4. Bae, S.-Y.; Kweon, D. H.; Mahmood, J.; Kim, M.-J.; Yu, S.-Y.; **Jung, S.-M.**; Shin, S.-H.; Ju, M. J.; Baek, J.-B. Nitrogen-rich two-dimensional porous polybenzimidazole network as a durable metal-free electrocatalyst for a cobalt reduction reaction in organic dye-sensitized solar cells *Nano Energy* **2017,** *34,* 533.
5. Mahmood, J.; Li, F.; **Jung, S.-M.**; Okyay, M. S.; Ahmad, I.; Kim, S.-J.; Park, N.; Jeong, H. Y.; Baek, J.-B. An efficient and pH-universal ruthenium-based catalyst for the hydrogen evolution reaction *Nature Nanotechnology* **2017**, *12,* 441.
6. Jeon, I.-Y.; Shin, S.-H.; Choi, H.-J.; Yu, S.-Y.; **Jung, S.-M.**; Baek, J.-B. Heavily aluminated graphene nanoplatelets as an efficient flame-retardant *Carbon* **2017**, *116*, 77.
7. Zhao, X.; Li, F.; Wang, R.; Seo, J.-M.; Choi, H.-J.; **Jung, S.-M.**; Mahmood, J.; Jeon, I.-Y.; Baek, J.-B. Controlled Fabrication of Hierarchically Structured Nitrogen-Doped Carbon Nanotubes as a Highly Active Bifunctional Oxygen Electrocatalyst *Advanced Functional Materials* **2017**, *27*(9), 1605717.

8. Jeon, I.-Y.; Kim, H. M.; Kweon, D. H.; **Jung, S.-M.**; Seo, J.-M.; Shin, S.-H.; Choi, I. T.; Eom, Y. K.; Kang, S. H.; Kim, H. K.; Ju, M. J.; Baek, J.-B. Metalloid tellurium-doped graphene nanoplatelets as ultimately stable electrocatalysts for cobalt reduction reaction in dye-sensitized solar cells *Nano Energy* **2016**, *30*, 867.

9. Ju, M. J.; Jeon, I.-Y.; Kim, H. M.; Choi, J. I.; **Jung, S.-M.**; Seo, J.-M.; Choi, I. T.; Kang, S. H.; Kim, H. S.; Noh, M. J.; Lee, J.-J.; Jeong, H. Y.; Kim, H. K.; Kim, Y.-H.; Baek, J.-B. Edge-selenated graphene nanoplatelets as durable metal-free catalysts for iodine reduction reaction in dye-sensitized solar cells *Science Advances* **2016**, *2*.

10. Mahmood, J.; Lee, E. K.; Jung, M.; Shin, D.; Choi, H.-J.; Seo, J.-M.; **Jung, S.-M.**; Kim, D.; Li, F.; Lah, M. S.; Park, N.; Shin, H.-J.; Oh, J. H.; Baek, J.-B. Two-dimensional polyaniline (C_3N) from carbonized organic single crystals in solid state *Proceedings of the National Academy of Sciences* **2016**, *113*, 7414.

11. Mahmood, J.; **Jung, S.-M.**; Kim, S.-J.; Park, J.; Yoo, J.-W.; Baek, J.-B. Cobalt Oxide Encapsulated in C_2N-*h*2D Network Polymer as a Catalyst for Hydrogen Evolution *Chemistry of Materials* **2015**, 27, 4860.

12. Jeon, I.-Y.; Choi, M.; Choi, H.-J.; **Jung, S.-M.**; Kim, M.-J.; Seo, J.-M.; Bae, S.-Y.; Yoo, S.; Kim, G.; Jung, H. Y.; Park, N.; Baek, J.-B. Antimony-doped graphene nanoplatelets *Nature Communications* **2015**, 6, 7123.

13. Mahmood, J.; Lee, E. K.; Jung, M.; Shin, D.; Jeon, I.-Y.; **Jung, S.-M.**; Choi, H.-J.; Seo, J.-M.; Bae, S.-Y.; Sohn, S.-D.; Park, N.; Oh, J. H.; Shin, H.-J.; Baek, J.-B. Nitrogenated holey two-dimensional structures *Nature Communications* **2015**, 6, 6486.

14. Ju, M. J.; Jeon, I.-Y.; Kim, J. C.; Lim, K.; Choi, H.-J.; **Jung, S.-M.**; Choi, I. T.; Eom, Y. K.; Kwon, Y. J.; Ko, J.; Lee, J.-J.; Kim, H. K.; Baek, J.-B., Graphene Nanoplatelets Doped with N at its Edges as Metal-Free Cathodes for Organic Dye-Sensitized Solar Cells *Advanced Materials* **2014,** *26* (19), 3055.

15. Jeon, I.-Y.; Choi, H.-J.; Ju, M. J.; Choi, I. T.; Lim, K.; Ko, J.; Kim, H. K.; Kim, J. C.; Lee, J.-J.; Shin, D.; **Jung, S.-M.**; Seo, J.-M.; Kim, M.-J.; Park, N.; Dai, L.; Baek, J.-B., Direct nitrogen fixation at the edges of graphene nanoplatelets as efficient electrocatalysts for energy conversion *Scientific Reports* **2013**, *3*.

16. Jeon, I. Y.; Choi, H. J.; Choi, M.; Seo, J. M.; **Jung, S.-M.**; Kim, M. J.; Zhang, S.; Zhang, L. P.; Xia, Z. H.; Dai, L. M.; Park, N.; Baek, J. B., Facile, scalable synthesis of edge-halogenated graphene nanoplatelets as efficient metal-free eletrocatalysts for oxygen reduction reaction *Scientific Reports* **2013**, *3*.

17. Jeon, I. Y.; Choi, H. J.; **Jung, S.-M.**; Seo, J. M.; Kim, M. J.; Dai, L.; Baek, J. B., Large-scale production of edge-selectively functionalized graphene nanoplatelets via ball milling and their use as metal-free electrocatalysts for oxygen reduction reaction *Journal of the American Chemical Society* **2013,** *135* (4), 1386.

18. Shin, Y. R.; **Jung, S.-M.**; Jeon, I. Y.; Baek, J. B., The oxidation mechanism of highly ordered pyrolytic graphite in a nitric acid/sulfuric acid mixture *Carbon* **2013,** *52* (0), 493.

19. Choi, H. J.; **Jung, S.-M.**; Seo, J. M.; Chang, D. W.; Dai, L. M.; Baek, J. B., Graphene for energy conversion and storage in fuel cells and supercapacitors *Nano Energy* **2012,** *1* (4), 534.

20. Chang, D. W.; Choi, H. J.; **Jung, S.-M.**; Dai, L. M.; Baek, J. B., Large clusters and hollow microfibers by multicomponent self-assembly of citrate stabilized gold nanoparticles with temperature-responsive amphiphilic dendrimers *Journal of Materials Chemistry* **2012,** *22* (26), 13365.

21. Jeon, I. Y.; Shin, Y. R.; Sohn, G. J.; Choi, H. J.; Bae, S. Y.; Mahmood, J.; **Jung, S.-M.**; Seo, J. M.; Kim, M. J.; Wook Chang, D.; Dai, L.; Baek, J. B., Edge-carboxylated graphene nanosheets *via* ball milling *Proceedings of the National Academy of Sciences of the United States of America* **2012,** *109* (15), 5588.

Proceedings

1. Poster Presentation

    1. Jeon, I.-Y.; **Jung, S.–M.**; Choi, H.-J, Tan, L.-S.; Baek, J.-B., Nanocomposite Prepared from *in-Situ* Grafting of Polypyrrole to Aminobenzoyl-Functionalized Multi-Walled Carbon Nanotube and Its Electrochemical Properties, **2011** spring meeting, The Polymer Society of Korea, Daejeon.

    2. **Jung, S.–M.**; Jeon, I.-Y.; J.-B. Baek, Solvothermal Synthesis of Doped Graphene, **2011** fall meeting**,** The Polymer Society of Korea, Gwangju.

    3. **Jung, S.–M.**; Jeon, I.-Y.; J.-B. Baek, Heteroatom-Doped Graphene *via* Solvothermal Process, **2012** Spring meeting, The Polymer Society of Korea, Daejeon.

    4. **Jung, S.–M.**; Jeon, I.-Y.; J.-B. Baek, Graphene nanoplatelets with edge-chloride prepared *via* ball milling, **2012** Fall meeting, The Polymer Society of Korea, Changwon.

    5. **Jung, S.–M.**; Jeon, I.-Y.; J.-B. Baek, Edge-chlorinated graphene nanoplatelets *via* ball-

milling, **2013** Spring meeting, The Polymer Society of Korea, Daejeon.

6. **Jung, S.–M.**; Jeon, I.-Y.; J.-B. Baek, The preparation of conjugated microporous polymer: cyclohexa-m-phenylene, **2013** Spring meeting, The Polymer Society of Korea, Chang-won.
7. **Jung, S.–M.**; Lee, E. K.; Choi, M.; Shin, D.; Jeon, I.-Y.; Seo, J.-M.; Jeong, H. Y.; Park, N.; Oh, J. H.; Baek, J.-B., Direct Solvothermal Synthesis of B/N-doped Graphene**, 2014** Carbon conference, Jeju.
8. **Jung, S.–M.**; Ko, J.; Lee, J.-J.; Kim, H. K.; J.-B. Baek, B-Doped Graphene as a Metal-Free Cathode Material Compared to Pt over a Co(II)/Co(III) Electrolyte for Dye-Sensitized Solar Cell, **2015** Spring meeting, The 115th General Meeting of the Korean Chemical Society, Ilsan.
9. **Jung, S.–M.**; Choi, I. T.; Lim, K.; Ko, J.; Kim, J. C.; Lee, J.-J.; Ju, M. J.; Kim, H. K.; Baek, J.-B., Boron-Doped Graphene as a Metal-Free Counter Electrode Material over a Co(II)/Co(III) Electrolyte for Dye-Sensitized Solar Cell, **2015** IUPAC 45th World Chemistry Congress, Busan.
10. **Jung, S.–M.**; Choi, I. T.; Lim, K.; Ko, J.; Kim, J. C.; Lee, J.-J.; Ju, M. J.; Kim, H. K.; Baek, J.-B., Heteroatom Doped Graphene as a Metal-Free Cathode Material Compared to Pt over a Co(II)/Co(III) Electrolyte for Dye-Sensitized Solar Cell, **2016** IUPAC-PSK, Jeju.

2. Oral Presentation

1. **Jung, S.–M.**; Seo, J.-M; Baek, J.-B., Solvothermal synthesis of boron and nitrogen co-doped graphene for modification of graphene properties, **2016** ACS 252nd American Chemical Society National Meeting and Exposition, Philadelphia, USA.
2. **Jung, S.–M.**; Baek, J.-B., Thermally stable triazine-based organic superstructure, **2017** ACS 253rd American Chemical Society National Meeting and Exposition, San Francisco, USA.

Patents

US 14/605,738	Graphene for semiconductor co-doping boron and nitrogen at the same time and preparation method thereof
KR 10-1611218 등록	붕소와 질소가 동시에 도핑된 반도체용 그래핀 및 이의 제조방법 (Graphene for semiconductor co-doping boron and nitrogen at the same time and preparation method thereof)

Synergistic Activities

Scientific advisor for

Insights reports for industry

Title: Graphene Technology and Development Status and Market Outlook (그래핀 기술 및 개발현황과 시장전망) (Display Bank, 2012)

Technical Skills

1. Synthesis of organic/polymeric compounds
2. Characterization Techniques

A. Experiences for Material Analyses: SEM (Nano SEM), TEM (JEM-2100, JEOL), EDX, XRD (D/max-2500/PC, Rigaku), UV/Vis spectrophotometer (Perkin-Elmer), Thermogravimetric analysis (TGA), Differential Scanning Calorimetry (DSC), BET (BELLSORP-max), Raman spectroscopy, AFM, FT-IR

B. Instrumental Analyses: X-ray photoelectron spectroscopy (XPS), Scanning transmission electron microscopy (STEM), Nuclear magnetic resonance spectroscopy (NMR), SEM: SUPRA 55VP (Carl Zeiss), EDS: Xflash5030 (Bruker), Electrochemical workstation: ZIVE SP2 (WonA tech)

C. Photoshop, Sigma Plot, Chemdraw, MS softwares (Word, Power poit, Excel, etc.)

Appendix II. Permission from Cited Journal Paper in This Thesis

Chapter I. Introduction

1.3 Carbon Materials

Permission from “Carbon Materials and Nanotechnology” Copyright © 2010, WILEY-VCH Verlag.

This Agreement between Sun ("You") and John Wiley and Sons ("John Wiley and Sons") consists of your license details and the terms and conditions provided by John Wiley and Sons and Copyright Clearance Center.

printable details

License Number	4100641357180
License date	May 02, 2017
Licensed Content Publisher	John Wiley and Sons
Licensed Content Publication	Wiley oBooks
Licensed Content Title	Carbon – Element of Many Faces
Licensed Content Author	Anke Krueger
Licensed Content Date	Mar 19, 2010
Licensed Content Pages	32
Type of Use	Dissertation/Thesis
Requestor type	University/Academic
Format	Print and electronic
Portion	Text extract
Number of Pages	1
Will you be translating?	No
Order reference number	15
Title of your thesis / dissertation	Dimension-controllable network structures from design to their applications
Expected completion date	Jul 2017
Expected size (number of pages)	100
Requestor Location	Sun-Min Jung 104-708 50, UNIST-gil Ulsan, 44919 Korea, Republic Of Attn: Sun-Min Jung
Publisher Tax ID	EU826007151
Billing Type	Invoice
Billing address	Sun-Min Jung 104-708 50, UNIST-gil Ulsan, Korea, Republic Of 44919 Attn: Sun-Min Jung
Total	**0.00 USD**

Figure 1.1

Permission from “Covalent organic frameworks (COFs): from design to applications”, Chemical Society Reviews 2013, 42(2), 548. Copyright © 2013, Royal Society of Chemistry.

This Agreement between Sun ("You") and Royal Society of Chemistry ("Royal Society of Chemistry") consists of your license details and the terms and conditions provided by Royal Society of Chemistry and Copyright Clearance Center.

printable details

License Number	4115180237375
License date	May 24, 2017
Licensed Content Publisher	Royal Society of Chemistry
Licensed Content Publication	Chemical Society Reviews
Licensed Content Title	Covalent organic frameworks (COFs): from design to applications
Licensed Content Author	San-Yuan Ding,Wei Wang
Licensed Content Date	Oct 11, 2012
Licensed Content Volume	42
Licensed Content Issue	2
Type of Use	Thesis/Dissertation
Requestor type	academic/educational
Portion	figures/tables/images
Number of figures/tables/images	1
Distribution quantity	1
Format	print and electronic
Will you be translating?	no
Order reference number	
Title of the thesis/dissertation	Dimension-controllable network structures from design to their applications
Expected completion date	Jul 2017
Estimated size	100
Requestor Location	Sun-Min Jung 104-708 50, UNIST-gil Ulsan, 44919 Korea, Republic Of Attn: Sun-Min Jung
Billing Type	Invoice
Billing address	Sun-Min Jung 104-708 50, UNIST-gil Ulsan, Korea, Republic Of 44919 Attn: Sun-Min Jung
Total	**0.00 USD**

Figure 1.2

Permission from “Rationally synthesized two-dimensional polymers”, Nature Chemistry 2013, 5(6), 453. Copyright © 2013, Nature Publishing Group.

This Agreement between Sun ("You") and Nature Publishing Group ("Nature Publishing Group") consists of your license details and the terms and conditions provided by Nature Publishing Group and Copyright Clearance Center.

printable details

License Number	4115171326283
License date	May 24, 2017
Licensed Content Publisher	Nature Publishing Group
Licensed Content Publication	Nature Chemistry
Licensed Content Title	Rationally synthesized two-dimensional polymers
Licensed Content Author	John W. Colson, William R. Dichtel
Licensed Content Date	May 12, 2013
Licensed Content Volume	5
Licensed Content Issue	6
Type of Use	reuse in a dissertation / thesis
Requestor type	academic/educational
Format	print and electronic
Portion	figures/tables/illustrations
Number of figures/tables/illustrations	1
High-res required	no
Figures	Figure1.2
Author of this NPG article	no
Your reference number	8
Title of your thesis / dissertation	Dimension-controllable network structures from design to their applications
Expected completion date	Jul 2017
Estimated size (number of pages)	100
Requestor Location	Sun-Min Jung 104-708 50, UNIST-gil Ulsan, 44919 Korea, Republic Of Attn: Sun-Min Jung
Billing Type	Invoice
Billing address	Sun-Min Jung 104-708 50, UNIST-gil Ulsan, Korea, Republic Of 44919 Attn: Sun-Min Jung
Total	**0.00 USD**

Figure 1.3

Permission from “Synthesis of hyperbranched polymers with controlled structure”, Polymer Chemistry 2013, 4(6), 1746. Copyright © 2013, Royal Society of Chemistry.

This Agreement between Sun ("You") and Royal Society of Chemistry ("Royal Society of Chemistry") consists of your license details and the terms and conditions provided by Royal Society of Chemistry and Copyright Clearance Center.

printable details

License Number	4115180646152
License date	May 24, 2017
Licensed Content Publisher	Royal Society of Chemistry
Licensed Content Publication	Polymer Chemistry
Licensed Content Title	Synthesis of hyperbranched polymers with controlled structure
Licensed Content Author	Yukari Segawa,Tomoya Higashihara,Mitsuru Ueda
Licensed Content Date	Nov 22, 2012
Licensed Content Volume	4
Licensed Content Issue	6
Type of Use	Thesis/Dissertation
Requestor type	academic/educational
Portion	figures/tables/images
Number of figures/tables/images	1
Distribution quantity	1
Format	print and electronic
Will you be translating?	no
Order reference number	
Title of the thesis/dissertation	Dimension-controllable network structures from design to their applications
Expected completion date	Jul 2017
Estimated size	100
Requestor Location	Sun-Min Jung 104-708 50, UNIST-gil Ulsan, 44919 Korea, Republic Of Attn: Sun-Min Jung
Billing Type	Invoice
Billing address	Sun-Min Jung 104-708 50, UNIST-gil Ulsan, Korea, Republic Of 44919 Attn: Sun-Min Jung
Total	**0.00 USD**

Table 1.1

Permission from “Graphene for energy conversion and storage in fuel cells and supercapacitors”, Nano Energy 2012, 1(4), 534. Copyright © 2012, Elsevier.

This Agreement between Sun ("You") and Elsevier ("Elsevier") consists of your license details and the terms and conditions provided by Elsevier and Copyright Clearance Center.

printable details

License Number	4115221229948
License date	May 24, 2017
Licensed Content Publisher	Elsevier
Licensed Content Publication	Nano Energy
Licensed Content Title	Graphene for energy conversion and storage in fuel cells and supercapacitors
Licensed Content Author	Hyun-Jung Choi,Sun-Min Jung,Jeong-Min Seo,Dong Wook Chang,Liming Dai,Jong-Beom Baek
Licensed Content Date	Jul 1, 2012
Licensed Content Volume	1
Licensed Content Issue	4
Licensed Content Pages	18
Type of Use	reuse in a thesis/dissertation
Portion	figures/tables/illustrations
Number of figures/tables/illustrations	1
Format	both print and electronic
Are you the author of this Elsevier article?	Yes
Will you be translating?	No
Order reference number	
Original figure numbers	
Title of your thesis/dissertation	Dimension-controllable network structures from design to their applications
Expected completion date	Jul 2017
Estimated size (number of pages)	100
Elsevier VAT number	GB 494 6272 12
Requestor Location	Sun-Min Jung 104-708 50, UNIST-gil Ulsan, 44919 Korea, Republic Of Attn: Sun-Min Jung
Total	**0.00 USD**

Chapter II. Direct Solvothermal Synthesis of B/N Doped Graphene

Permission from “Direct solvothermal synthesis of B/N doped graphene”, Angewandte Chemie International Edition 2014, 53(9), 2398. Copyright © 2014, WILEY-VCH Verlag.

Chapter III. B-doped Graphene as an Electrochemically Superior Metal-free Cathode Material as Compared to Pt over a Co(II)/Co(III) Electrolyte for Dye-sensitized Solar Cell

Permission from “B-doped graphene as an electrochemically superior metal-free cathode material as compared to Pt over a Co(II)/Co(III) electrolyte for dye-sensitized solar cell”, Chemistry of materials 2014, 26(11), 3586. Copyright © 2014, American Chemical Society.

Chapter V. Unusually Stable Triazine-based Organic Superstructure

Permission from “Unusually stable triazine-based organic superstructure”, Angewandte Chemie International Edition 2016, 55(26), 7593. Copyright © 2016, WILEY-VCH Verlag.

This Agreement between Sun ("You") and John Wiley and Sons ("John Wiley and Sons") consists of your license details and the terms and conditions provided by John Wiley and Sons and Copyright Clearance Center.

printable details

License Number	4111210027872
License date	May 17, 2017
Licensed Content Publisher	John Wiley and Sons
Licensed Content Publication	Angewandte Chemie
Licensed Content Title	Unusually Stable Triazine-based Organic Superstructures
Licensed Content Author	Sun-Min Jung,Dongwook Kim,Dongbin Shin,Javeed Mahmood,Noejung Park,Myoung Soo Lah,Hu Young Jeong,Jong-Beom Baek
Licensed Content Date	Apr 27, 2016
Licensed Content Pages	5
Type of Use	Dissertation/Thesis
Requestor type	Author of this Wiley article
Format	Print and electronic
Portion	Full article
Will you be translating?	No
Title of your thesis / dissertation	Dimension-controllable network structures from design to their applications
Expected completion date	Jul 2017
Expected size (number of pages)	100
Requestor Location	Sun-Min Jung 104-708 50, UNIST-gil Ulsan, 44919 Korea, Republic Of Attn: Sun-Min Jung
Publisher Tax ID	EU826007151
Billing Type	Invoice
Billing address	Sun-Min Jung 104-708 50, UNIST-gil Ulsan, Korea, Republic Of 44919 Attn: Sun-Min Jung
Total	**0.00 USD**

Acknowledgements

Firstly, I sincerely appreciated many people, who have helped and encouraged to complete PhD course. It has been a long journey for me and I realized that it is worthwhile.

I profoundly thank to my advisor, Prof. Jong-Beom Baek, who has always motivated and supported during the combined master and PhD course. Also, I am thankful to the committee members, Profs. Myoung Soo Lah, Noejung Park, Jung-Woo Yoo and Hu Young Jeong, who have helped to improve research quality. I have learned lots of lessons related to scientific knowledge and attitude.

I am greatly thankful to co-workers, CDCOF group members and UCRF as well as my friends. Whatever I did, they have supported me and provided huge belief.

Finally, I dedicated thesis to my family, being my strongest background with unlimited love.

2017. 06. 25
Sun-Min Jung

감사의 글

7년 전, 이곳 유니스트에 처음 발을 디뎠을 때가 기억이 납니다. 따뜻한 가을 햇살이 반겨주었던 곳이었습니다. 처음 방문한 울산은 낯설었지만, 그 낯섦 뒤에 당찬 각오로 차 있었습니다. 초심을 잃지 않고 생활하는 것은 참으로 어려운 일이었습니다. 하지만 초심을 잃을 때마다 혹은 어려움을 겪을 때마다, 격려와 응원을 해주시는 교수님, 랩실 동료들, 친구들 그리고 사랑하는 가족 덕분에 무사히 학위과정을 마칠 수 있었습니다. 다시금 생각해보면 제 주변에서 좋은 사람들로부터 많은 도움을 받았고, 이는 얼마나 행복한 일인가를 생각하게 되었습니다.

박사과정 동안 지도해주신 백종범 교수님, 6 년 반이란 세월 동안 많은 가르침과 살이 되고 뼈가 되는 조언을 통해 제가 졸업을 할 수 있었습니다. 인내심을 가지고 저를 지켜봐 주신 점 진심으로 감사드립니다. 그리고 제가 하고 싶은 연구를 마음껏 할 수 있도록 도와주셔서 감사합니다. 입학했을 때부터 자주 들었던 말씀 중에 실험실 설거지를 강조하시며 기본부터 충실해야 한다는 말, 깊이 새겨듣겠습니다.

심사위원으로 모신 나명수 교수님, 박노정 교수님, 유정우 교수님, 정후영 교수님 진심으로 심사위원으로 모실 수 있어서 감사드립니다. 학위 기간 동안 도움 말씀도 많이 주시고, 공동 연구를 통하여 논문에 이름을 올릴 수 있었던 것도 영광입니다. 그리고 다양한 방면으로 바라볼 수 있도록 도와주셔서 정말 감사합니다. 정후영 교수님, 덕분에 많은 것도 배우고, 높은 수준의 데이터를 함께 의논했다는 사실로도 영광입니다.

학부 때 지도교수님으로 연을 맺어 안부 인사를 여쭐 때마다 반갑게 맞아주시는 신채호 교수님, 감사합니다. 교수님의 지도로 제가 연구자로서 길로 첫 발 내디딜 수 있었어요. 다양한 경험을 할 수 있도록 도와주셨던 것들이 양분이 되어 지금의 제가 있을 수 있었어요. 항상 감사함을 잊지 않고 지내고 있어요.

긴 시간을 함께 보낸 CDCOF 구성원들. 주명종 박사님, 논문 지도도 해주시고, 좋은 말씀들 감사합니다. 인엽 오빠, 후배들에게 먼저 손 내밀어 주시고, 큰오빠처럼 잘 챙겨주셔서 고맙습니다. 그리고 실험실에 모범이 되신 점 항상 배우고 싶어요. 고등학교 선배님이신 따뜻한 서윤 언니, 언제나 미소를 잃지 않고 어떤 이야기라도 귀 기울여주시는 현정 언니, 그리고 친언니처럼 잘 챙겨주신 경주 언니, 운동도 실험도 모두 잘하시는 연란 언니, Diligent Dr. Javeed, thanks for your help and warm encouragement and I learned a lot from you, 동기로 지내며 곁에서 의지가 되고 힘이 되어준 꼼꼼한 맥가이버 정민이와 야무지고 따뜻한 민정이, 착하고 똑똑한 후배들; 졸업한 종열이, 솔선수범하는 석진이, 랩장 윤광씨, 다부진 선희, 차분한 수영이, 재미있는 혁준이, 3개국어 구사하는 성욱이, Smile guy Ishfaq, 속 깊은 도형이, 신입생인 종필이, 부재씨 감사드립니다. 옆 실험실이셨지만 옆자리에서 많이 챙겨주던 경식오빠 고맙습니다. 그리고 현정이 언니 남편이자 유준이 아빠이신 영훈이 오빠, 어려운 전기화학을 덕분에 쉽게 다가갈 수 있었어요.

논문에 도움을 많이 준 동욱 오빠, 은광씨, 동빈씨, 인택씨, 기민씨, 재천씨, 정민씨 감사드립니다.

저의 대학원 시절 동안 가장 가까운 짝꿍이 되어준 고마운 우리 수현쌤, 수현쌤 없었으면 졸업도 못했을 거에요. 힘들 때 옆에 있어주며 위로도 해주시고 의지할 수 있도록 도와주셔서 정말 감사해요. 대학원 시절 동안 행복하고 즐거운 추억을 만들어주셔서 고마워요.

중학교 때부터 쭈욱 만나온 우리 은혜, 심성도 곱고 어른스러운 우리 은혜, 내가 참 많이 배운다. 고등학교 시절 함께 동고동락하며 지냈던 호님이, 요다, 렉슈, 토토, 혜이니, 스큐, 희영이, 오민이, 집을 떠나 기숙사 생활하면서 너네와 함께 지낼 수 있었던 것이 큰 행운이야. 그리고 혜진이, 홍양, 희연이, 윤미, 은혜 대학교 때부터 지금까지 꾸준히 만나면서 좋은 일마다 항상 응원해주어서 고마워.

세상에서 가장 사랑하는 우리 가족, 아빠, 엄마, 영준이 고마워요. 항상 옆에서 살뜰히 챙겨주고, 언제나 애교 가득한 목소리로 응원해주시고, 제가 하고 싶었던 것은 최선을 다해 할 수 있도록 도와주신 점, 부족한 딸이지만 언제나 사랑으로 보듬어준 우리 가족 사랑하고 감사합니다. 사랑해요❤

한 분 한 분 다 말씀드리지 못했지만 석박사 생활 동안 많은 도움을 주신 분들께 진심으로 머리 숙여 감사드립니다.

저의 부족하다고 느끼는 마음 끝자락에는 "배움에는 끝이 없다"라는 것을 절실히 느끼고 있습니다. 겸손한 자세로, 배움의 자세로 조금씩 조금씩 성장해 나갈 수 있도록 노력하겠습니다.

2017 년 6 월 25 일
정선민 드림